Année 2014 N° d'ordre :41616

Université Lille1 Sciences et Technologies
Laboratoire Génie Civil et géo-Environnement
Ecole doctorale Sciences Pour l'Ingénieur

THÈSE

Pour l'obtention du grade de
Docteur de L'Université des Sciences et Technologies de Lille
Discipline : Génie Civil
Sous le titre de :

Use of thermal heating /cooling process for rock fracturing: Numerical and experimental analysis

---

par

Muhammad YASEEN

Jury

SHAHROUR Isam	**Professeur, Univ^{2}ersité Lille 1**	**Directeur de thèse**
ZEMMOURI Jaouad	**Professeur, Université Lille 1**	**Co-directeur de thèse**
DJERAN-MAIGRE Irini	**Professeur, INSA de Lyon**	**Rapporteur**
ALHEIB Marwan	**HDR, INERIS- Ecole des Mines de Nancy**	**Rapporteur**
ZAOUI Ali	**Professeur, Université Lille 1**	**Examinateur**
Hanbing BIAN	**MCF, Université Paul Verlaine Metz**	**Examinateur**

ACKNOWLEDGEMENTS

I would like to thank a number of people who were instrumental in the completion of this thesis.

First, I would like to thank and present supreme respecting to my thesis advisors who gave me the opportunity to do this work under their guidance. **Mr. Isam SHAHROUR**; Professor at the University of Lille 1 and the director of the "Laboratoire Génie Civil et géo-Environnement LGCgE"; who managed, supervised and enriched this work by his notices and guidance. He is pacemaker for everyone wants the success. **Mr. Jaouad ZEMMOURI**; Professor at the University of Lille 1 (Physics laboratory); who provided me psychological and scientific supports besides that he added to me the powerful physician thinking manner. He is real benchmark in my life.

I would like to thank the members of the defense committee: **Mr. Ali ZAOUI** Professor at the University of Lille; **Mrs. Irini DJERAN-MAIGRE** Professor at the INSA de Lyon; **Mr. Marwan ALHEIB** HDR at INERIS- Ecole des Mines de Nancy and **Mr. Hanbing BIAN** MCF at the University of Paul Verlaine Metz whose remarks, advices and discussions brought to me a lot to improve the quality of my dissertation.

Special thank is also extended to **Mr. Malek SIBI**; Research Engineer at the University of Lille 1; for his good humor and very good advices. I found in him the good supporter by his extensive experience in the experimental field.

Special thanks to **Mr. Yves Quiquempois**, Professor at the University Lille 1, for his cooperation and logistical support that allowed me to finish this work.

To my friends who shared with me moments of happiness and sadness. To my labmates with who I spent unforgettable moments.

I couldn't forget in these acknowledgments the most expensive: **my parents**, for the encouragement and the support for all of the sacrifices that you've made on my behalf. Your prayers for me were what sustained me thus far everything they gave it to me to reach this stage in the science harvest especially during these years of Ph.D. As well, I would like to thank **my dear sisters and brother** for all motivations they gave it to me.

“Of all the home remedies, a good wife is best” to my beloved wife who will give me soon my candle “Abdelrahman”.

Finally, I benefit from this opportunity to dedicate this work to my dear country that passes a very hard ordeal that fires our hearts. I wish that it will overtake this situation in good solidarity. **Forever Beloved SYRIA**

RÉSUMÉ

La fracturation des roches concerne plusieurs applications industrielles, telles que les tunnels, l'excavation et l'industrie minière. Les techniques classiques pour fracturer la roche présentent des effets indésirables face à leur utilisation dans certaines circonstances. Par conséquent, la fracturation par spallation thermique a été suggérée comme une solution alternative. Cette technique produit des contraintes de compression dans la roche due à un flux de chaleur intense. Une fois ces contraintes dépassent la résistance à compression de la roche, la rupture aura lieu par éjection des petits éclats. Cette mode de fracturation thermique nécessite une source d'énergie puissante et elle influence négativement les conditions du travail. Profitant d'une faible résistance à traction du matériau de roche, le présent travail propose une méthode basée sur un chauffage rapide de la matière rocheuse par un rayonnement micro-ondes, suivi par un refroidissement rapide par l'eau afin de fracturer la roche. Durant ce processus, une dilatation thermique est produite à l'intérieur de la zone traitée, suivie d'une contraction thermique. Cette contraction produit des contraintes de traction qui conduira à la rupture de la matière de roche. Le processus de chauffage/refroidissement a été analysé grâce à un modèle numérique qui décrit les événements physiques et l'influence de différents paramètres. En outre, le processus a été examiné expérimentalement du point de vue thermique.

ABSTRACT

The issue of rock fracturing concerns several industrial applications, such as tunneling or excavation in rock material, extraction of rock blocks and the mining industry. The conventional techniques to fracture the rock material are associated with disadvantages restrict their use in certain circumstances. Consequently, the fracture by thermal spallation was suggested as an alternative solution. This solution basically depends on exceeding the compressive strength of the rock material by compressive stresses induced by heating effects. This necessitates high temperature at the rock surface, which requires high power supply and it degrades the work conditions. Profiting from low tensile strength of the rock material, the present work proposes a method based on a rapid heating of the rock material by microwaves radiation followed by a rapid cooling by water to fracture the rock material. During this process, a thermal dilatation is produced within the treated zone, which is then followed by a thermal shrinkage. This shrinkage produces tensile stresses, which could lead to fracturing the rock material. The heating/cooling process will be analyzed through numerical model describes the physical events and the influence of different parameters. Experimentally, the process will be examined from thermal point of view.

TABLE OF CONTENTS

Résumé iii

Abstract v

Table of Contents vii

List of Figures xi

List of Tables xvii

General Introduction 1

Chapter 1 : State of the art 5

- **1.1 Introduction:** 7
- **1.2 Analysis of the conventional tunneling and drilling methods:** 7
- **1.3 Thermo-mechanical behavior of rock material:** 13
  - 1.3.1 The thermal properties: 13
  - 1.3.2 Thermal damage in rock Materials: 16
  - 1.3.3 Influence of the thermal treatment on the physical properties: 19
- **1.4 Thermal spallation principle:** 21
- **1.5 Experimental works** 24
  - 1.5.1 The Laser as heat sources 25
  - 1.5.2 Microwaves as heat source 31
- **1.6 Numerical Modeling of thermal spallation:** 33
- **1.7 Conclusion** 38

Chapter 2 :Laboratory investigation of the rock-laser interaction 41

- **2.1 Introduction:** 43

2.2 Experimental procedures: 43
2.2.1 Rock Materials 43
2.2.2 Laser drilling system 44
2.2.3 Experimental program: 44

2.3 Laboratory results 46
2.3.1 Group 1 46
2.3.2 Group 2 47
2.3.3 Group 3 49

2.4 Conclusion 51

Chapter 3 : Use of the heating/cooling process in rock fracture: Numerical analysis 53

3.1 Introduction: 55

3.2 Description of the heating/cooling method 55

3.3 Numerical modeling of the heating/cooling fracture process 57
3.3.1 Presentation of the numerical model 57
3.3.2 The microwaves-rock material interaction 59
3.3.3 Heat transfer in the rock material 61
3.3.4 Thermo-mechanical behavior of the rock material 68

3.4 Numerical model 72

3.5 Application to granite sample 74
3.5.1 Presentation of the sample properties and boundary condition 74
3.5.2 Numerical results 76
3.5.3 Mechanical response 84

3.6 Summary and conclusion 97

Chapter 4 : Analysis of the cyclic thermal process and its influence on the penetration rate 99

4.1 Introduction 101

4.2 Presentation of the adopted continuum damage model 101
4.2.1 The damage Constitutive law 101
4.2.2 The computational model and damage implementation in Comsol 105
4.3 Analysis of the first cycle of the heating/cooling process: 108
4.3.1 The application model: 108
4.3.2 Results: 109
4.4 Analysis of the second cycle of the heating/cooling process 117
4.4.1 Numerical modeling 117
4.4.2 Results 118
4.5 Conclusion 122
Chapter 5 : Thermal laboratory study of the heating-cooling fracture process in rock material 125
5.1 Introduction: 127
5.2 Description of the experimental setup and procedure 127
5.2.1 Heating/cooling dispositive 127
5.2.2 Thermal monitoring system 129
5.2.3 Experimental protocol 131
5.3 Results and discussion 132
5.3.1 Test with cooling water at 20 °C 132
5.3.2 Test with cooling water at 100 °C 140
5.4 Conclusion 141
Conclusion 143
References 145

LIST OF FIGURES

Figure 1.1: Range of methods compared to uniaxial compressive strength (Heiniö, 1999)..................8

Figure 1.2: Drill and Blast cycle (Heiniö, 1999) 9

Figure 1.3: Cutting process in TBM (Herrenknecht,2003)..10

Figure 1.4: The penetration rate with the compressive strength (Gong and Zhao, 2008) 11

Figure 1.5 : Some damaged cutters...11

Figure 1.6: The composition and temperature effects on the thermal conductivity of the different rocks types (Vosteen and Schellschmidt, 2003) 14

Figure 1.7: Thermal conductivity variation with the physical properties (Singha et al., 2007) 14

Figure 1.8: The specific heat capacity and the thermal capacity dependence on the temperature (Vosteen and Schellschmidt, 2003) 15

Figure 1.9: The thermal diffusivity vs temperature (Vosteen and Schellschmidt, 2003)....................16

Figure 1.10: The tensile strength variation with the heating treatment (Hommand-Etienne and Hourpert, 1989)..18

Figure 1.11: The cracking density with the temperature (Hommand-Etienne and Hourpert, 1989)...19

Figure 1.12: The porosity variation with the temperature (Takarli and Agbodjan, 2006)..................20

Figure 1.13: The permeability vs the temperature (Chaki et al., 2008)...20

Figure 1.14: Evolution of longitudinal wave velocity vs temperature and the energy attenuation 21

Figure 1.15: Simplified scheme of spall formation on surface of a semi-infinite solid (Rauenzahn and Tester, 1989) 22

Figure 1.16: Schematic distribution of thermoelastic stresses in thermal spallation process (Germanovich, 1997) 23

Figure 1.17: Membrane stresses as a function of radius at time of crack initiation (Farra, 1968) 26

Figure 1.18: Linear tracks tests and the identified zones (Xu et al., 2003) 29

Figure 1.19: increased permeability in lased samples (Xu et al., 2004) 30

Figure 1.20: Variation of ROP according to SE and saturation liquid type (Ahmadi et al., 2011) 31

Figure 1.21: ROP variation with confining pressure in Granite (Ahmadi et al., 2012)......................31

Figure 1.22: Scheme of the microwave drilling apparatus and configured hole (Jerby and Dikhtyar, 2001) 32

Figure 1.23: Schematic illustration of thermally weakening rock by microwaves (Lmdroth et al., 1991) 32

Figure 1.24: Dependence of penetration rate and free surface temperature on the rock structure, (1) $2a_0$=0.1 mm, Δ=0.158 mm, (2) $2a_0$=0.1 mm, Δ=0.5 mm, (3) $2a_0$=1 mm, Δ=1.58 mm and (4) $2a_0$=1 mm, Δ=5 mm...34

Figure 1.25: Velocity of spalling front advance and surface temperature at the moment of spalling (Germanovich, 1997) 34

Figure 1.26: Removed rock material for different Laser-on time (Xu et al., 2005) 35

Figure 1.27: Temperature and stress profiles (Xu et al., 2005) 36

Figure 1.28: Fracture initiation and propagation during heating process (Walsh et al., 2011) 37

Figure 1.29: Damage comparison between flat and rough surface, (Walsh et al., 2011)...................37

Figure 1.30: Pore-fluid enhanced spall-production model: the micro-pores serve as site for fracture initiation caused by the rapid heating. The expansion of fluid within the pores aids in fracture propagation. Fluid expansion and buckling cause the spall to be removed from the surface. (Walsh and Lomov, 2013)...38

Figure 2.1: a) The Experimental setup used in the test, b) The arrangement of the sample under the laser nozzle..45

Figure 2.2: Results of the tests:...46

Figure 2.3: The molten border due to laser treatment in test (4): power peak 1.34 kW, average power 201 watts, nozzle velocity 0.0 mm/s 47

Figure 2.4: The Laser trace and the identified zones in test (6) power peak 1.34 kW, average power 241.2 watts, nozzle velocity 0.4 mm/s 48

Figure 2.5: Cracks in tests: 49

Figure 2.6: Damage induced in the area adjacent to the laser trajectory (test 8) 49

Figure 2.7: Results of tests: 50

Figure 3.1: Illustration scheme of the whole process, a) heating by microwaves, b) heat transfer during heating phase, c) heat transfer during cooling phase, d) the expected damaged zone. 57

Figure 3.2: The physical events during one cycle of examined thermal treatment 59

Figure 3.3: Temperature expected profile on the treated rock surface 63

Figure 3.4: Nukiyama’s curve presented by (Karwa, 2012) 64

Figure 3.5: Cooling profile over the time (Karwa, 2012) 65

Figure 3.6: Heat transfer coefficient variation with the heat flux 66

Figure 3.7: Water temperature variation with heat energy and the corresponding phases 68

Figure 3.8: Crack propagation during compression 68

Figure 3.9: Crack propagation during tension 69

Figure 3.10: Schematic illustration of the removing rock process, a) Intact rock, b) Crack propagation due to compressive stresses in parallel to the treated surface during heating phase, c) Crack propagation due to tensile stresses during cooling phase and d)The removed part of the rock body 70

Figure 3.11 Thermal expansion coefficient variation with temperature (Heuze, 1983) 72

Figure 3.12 Presentation of the mode, the initial and boundary conditions 75

Figure 3.13 The adopted geometry and mesh 75

Figure 3.14 Variation of the heat exchange during the thermal treatment 76

Figure 3.15 Temperature profile over the treated zone 77

Figure 3.16: Temperature variation over the radial distance of treated surface 78

Figure 3.17: Temperature variation with the depth beneath the treated surface.................................79

Figure 3.18: Temperature profiles in the subsurface areas under the treated surface..........................79

Figure 3.19: Temperature profile due to different time of heating just between (25 and 200 seconds). 80

Figure 3.20 Temperature profile according to different values of heat exchange coefficient............82

Figure 3.21 Coolant Temperature influence on the temperature profile 83

Figure 3.22: The Temperature profile according to different power intensity 83

Figure 3.23: Radial stress variation over the treated zone at different moments................................85

Figure 3.24: Tangential stress variation over the treated surface at different moments 86

Figure 3.25: a) Temperature spatial distribution at the second 50, b) Temperature distribution at the second 51, c) Radial stress distribution at the second 50, d) Radial stress distribution at the second 51 second 87

Figure 3.26: The effect of heat exchange coefficient on the conversion process 88

Figure 3.27: variation of stress value with heat exchange coefficient after cooling start (moment: 51 sec) 89

Figure 3.28: Influence of the power intensity on the conversion process 90

Figure 3.29: The relationship between power intensity and the induced tensile stress (at moment: 51 sec) 90

Figure 3.30: Influence of the coolant temperature on the conversion process 91

Figure 3.31: Variation of induced tensile stress with coolant temperature (at moment: 51 sec).........92

Figure 3.32: Radial stress profile with the depth of the sample at different moments 93

Figure 3.33: Variation of penetration depth over the cooling time..94

Figure 3.34: Variation of penetration depth with time due to different irradiation density................95

Figure 3.35: The maximum attained penetration depth as a function of the power density................95

Figure 3.36: The profile of the penetration depth over time due to the variation of heat exchange coefficient 96

Figure 3.37: a) Evaluation of the penetration depth according to different coolant temperatures, b) Variation of maximum attained penetration depth with coolant temperature 96

Figure 3.38: a) variation of penetration depth profile according to different heating period, b) variation of penetration depth with heating period 97

Figure 4.1: Flowchart of the followed algorithm to calculate the damage 107

Figure 4.2: The 2D axisymmetric model and the initial and boundary conditions 109

Figure 4.3: Damage variable variation over the time of treatment, Subfigure: damage variation during cooling phase 110

Figure 4.4: Radial stress variation at the treated surface: a) without damage, b) with damage during different moments of cooling process 111

Figure 4.5: Tangential stress variation at the treated surface during different moments of cooling process 112

Figure 4.6: damage evolution in the subsurface layers beneath the treated spot 113

Figure 4.7: Damage evolution beneath the treated surface (centroid line) 114

Figure 4.8: Penetration depth of damage under the treated zone 115

Figure 4.9: Young ‘modulus degradation with the damage variable 115

Figure 4.10: The estimated removed rock material after the thermal treatment during the first cycle 116

Figure 4.11: Variation of the damage penetration depth with different coolant temperatures 117

Figure 4.12: Scheme of the adopted geometry for the second cycle analysis 118

Figure 4.13: Temperature profile during the cyclic application of the thermal treatment 119

Figure 4.14: damage variation with process time at different levels under the treated surface: a) first cycle, b) second cycle 120

Figure 4.15: Damage evolution during the first and second cycles 121

Figure 4.16: The removed rock material after the second cycle 122

Figure 5.1: Experimental set up used in the study of the heating-cooling process in rock material . 128

Figure 5.2: Camera calibration setup 130

Figure 5.3: Camera calibration curve 130

Figure 5.4: Scheme of thermocouples installation 131

Figure 5.5: Experimental setup 132

Figure 5.6: Temperature variation measured by the thermocouple (Test with water at 20 °C) 133

Figure 5.7: Temperature profile from the second sample cooled down with fresh water (~20 °C) .. 134

Figure 5.8: Temperature distribution on the rock surface during the last second of heating: 135

Figure 5.9: Temperature distribution at the beginning of cooling phase: 136

Figure 5.10: Comparison between the numerical and experimental temperature results 137

Figure 5.11: a) Experimental heating and cooling rates, b) Numerical heating and cooling rates 137

Figure 5.12: Comparison between numerical and experimental results in the cooling phase 138

Figure 5.13: Heating and cooling rates during the second test 139

Figure 5.14: Heating and cooling rates within the treated zone 139

Figure 5.15: Bubbles formation during cooling phase by hot water at (~100 °C) 140

LIST OF TABLES

Table 1.1 : The mechanical properties after the thermal treatment (Takarli and Agbodjan, 2006).....17

Table 1.2: Average rock properties and spalling ratings of some rocks (Rauenzahn and Tester, 1989) 24

Table 1.3: Spallation Temperature in Laser and Flame-jet tests (Rauenzahn and Tester, 1989) 27

Table 2.1: The thermal and mechanical properties of the tested Granite 43

Table 2.2 : The parameters of Laser Nd:YAG..45

Table 3.1 Granite properties used in the simulation 74

Table 3.2 : Heat convection coefficient values (Vlachopoulos and Strutt, 2002) 81

Table 4.1: Thermal and mechanical properties of the Granite..108

GENERAL INTRODUCTION

The issue of rock fracturing concerns several industrial applications, such as tunneling or excavation in rock material, extraction of rock blocks and the mining industry. Generally the industry uses two methods for the rock fracturing: explosive and mechanical techniques. The former is used in mining industry as well as in tunneling in hard rock in non-urban area, while the latter is used in soft rocks as well as in sensitive area where the uses of explosives is prohibited. Nowadays, the industry uses the Tunnel Boring Machine (TBM) for the construction of tunnels in almost every type of soils, even in hard rocks. In this case, the industry encounters a major difficulty, which is related to the cutters damage during tunneling, which requires complex replacement operation. Consequently the industry is particularly interested by alternative methods for the rock excavation, or the association of the conventional cutters to another technology, which could reduce the rock material strength and consequently facilitate its excavation.

The use of a thermal treatment could be a good alternative for the hard rock softening. Indeed, a process of heating followed by cooling induces compression and extension stresses in the rock material, which could exceed the rock strength and consequently lead to the rock damage or fracture. The thermal spallation was suggested as an alternative solution in the previous century. This technique has been expected to achieve the same penetration rate as the mechanical ones. Several theoretical descriptions were proposed to explain the mechanism of the thermal spallation, in particular by Preston et al.(1934). Spallation results from temperature gradient in the rock material, which produces compressive and tensional stresses. When the compressive stresses exceed the compressive strength of the rock material, failure occurs and eventually thin spalls are rejected from the rock body.

As the rock material has generally high compressive strength, powerful heat sources are required for the generation of high compressive stresses. Different heat sources were tested, such as the Flame-jet (Rauenzahn and Tester, 1989) (Potter et al., 2010) and the laser (Farra, 1968) (Rauenzahn and Tester, 1989) (Xu et al., 2003) (Xu et al., 2004) (Ahmadi et al., 2011) (Ahmadi et al., 2012). The reported power intensity varied between 0.5 and 14.0 MW/m². The induced surface temperature varied between 250 °C up to the melting temperature (900 °C to 1200 °C) where the rock material was removed by melting mechanism.

The high level of power intensity requires high power supply. In addition, the high level of temperature leads to poor and insecure work conditions. Since the tension strength of rock materials is largely inferior to that in compression, the use of a thermal process treatment for the creation of tension stresses could reduce significantly the energy needed for the rock fracture. This process can be accomplished by submitting the rock surface to heating-cooling cycles. In this thesis, we propose a method based on this statement. It consists in a rapid heating of the rock material by microwaves radiation followed by a rapid cooling by water. During this process, a thermal dilatation is produced within the treated zone, which is then followed by a thermal shrinkage. During the cooling phase, the rock shrinkage produces tensile stresses, which could lead to fracturing the rock material. Physical processes involved in this treatment are analyzed, in particular the microwaves-rock coupling (heating phase), coolant-rock interaction (cooling phase) and the thermo-mechanical coupling in the rock material.

The thesis includes five chapters:

The first chapter includes a literature review. It describes the tunneling methods as well as the thermo-mechanical behavior of the rock material. It includes also a literature review of the experimental and numerical researches conducted on the rock thermal spallation.

The 2nd chapter presents a laboratory study of the interaction between the rock material and a laser radiation. The study is conducted using the laser Nd:YAG. Different laser power parameters are tested. The removal rock mechanism by laser and the influence of the laser head velocity will be analyzed.

The 3rd chapter presents the method proposed in this thesis, which is based on a heating/cooling treatment of the rock material. The chapter presents the numerical model used in the analysis of this method as well as the influence of the main parameters on the method performances.

The 4th chapter presents a numerical analysis of the rock excavation using the heating/cooling process in taking into account the rock material damage and a repetitive loading heating/cooling process. The continuum damage law will be presented as well as its use for the rock fracture using a heating/cooling treatment.

The 5th chapter describes an experimental study of the heating/cooling thermal treatment of the rock material. The experimental setup will be described as well as the experimental results and their comparison to the numerical modeling.

CHAPTER 1

STATE OF THE ART

1.1 Introduction:

Brief statement of the used tunneling and drilling methods will be presented in this chapter. This presentation includes the “Drill & Blast” and “Tunneling Boring Machine TBM” ones. Technical description of these technologies will be rapidly highlighted. The advantages and disadvantages of each will be shortly addressed. Relatively to their major concerns, the thermal treatment of the rock material was suggested to be the promising alternative of those technologies in order to bring the prospective improvements over their performance.

Since the rock material is a complex structure that contains pores, flaws embedded in the structure, heterogeneous composition, formed under different conditions (temperature, pressure…), it is very important to point out the thermal rock behavior and its reaction to thermal treatment. So, the variation of the structural, mechanical and physical properties of rock material with temperature will be presented in few subsections.

Then after, a bibliographic analysis of the thermal spallation will be presented. Many aspects will be handled: the conception of thermal spallation, results of experiments conducted in this field, numerical modeling efforts and the heat sources used to deliver the heat to rock body. As well, different issues either in experimental or modelling works will be addressed, in trying to illustrate and understand the physical processes behind the thermal spallation of rocks.

1.2 Analysis of the conventional tunneling and drilling methods:

Generally the rock excavation methods are divided into two large families: “Drill & Blast”, and mechanical drilling. The latter is furthermore subdivided into partial face (e.g. roadheaders, hammers, excavators…) and full face (e.g. TBM, shield, pipe jacking, and micro tunneling). The choice of the excavation method depends on many factor should be taken into account (Heiniö, 1999): Tunnel dimensions, Tunnel geometry, Length of tunnel, total volume to be excavated, Geological and rock mechanical conditions, Ground water level and expected water inflow, Vibration restrictions and Allowed ground settlements.

The rock compressive strength is one of the most important factors. The "Drill & Blast" and TBMs are reported appropriate for wide range of soils and hard rocks types. The TBM is more adequate for hard rock with strength varies between 30 MPa till 250 MPa. The "Drill & Blast" is consistent with almost all levels of compressive strength greater than 30 MPa (Figure 1.1).

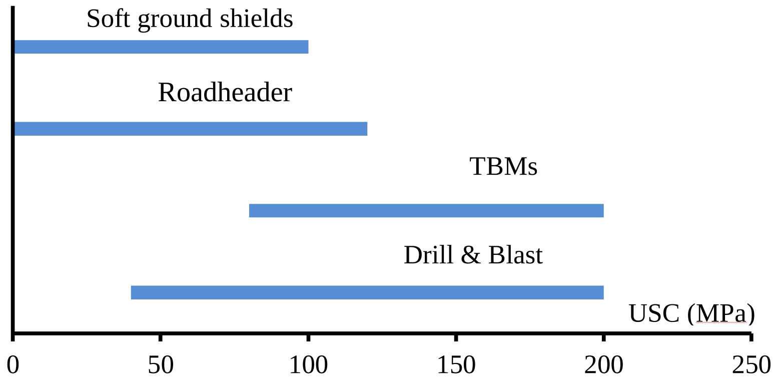

Figure 1.1: Range of methods compared to uniaxial compressive strength (Heiniö, 1999)

Drill & Blast

In this method, a predetermined pattern of holes to a selected depth in the rock face of the proposed tunnel's path are primarily drilled. Then after, those are filled with explosives substances such as dynamite to be then detonated. Likewise, the rock will be cracked and broken apart. The loosened debris or muck is then drove out and hauled away. The drilling and blasting method has a cyclic nature that requires a good organized work site as well as a good planning of the each cycle during the process to guarantee the security of working staff as well as the rapidity of performance.

However, this method has many advantages (Palmström, 1996), in particular:

- It can be applied to nearly any type of rock.
- It gives great flexibility in the performance of the excavation.
- The rock support can be installed easily and quickly.

The uncertainty in cracks propagation because of blasting largely influences the drilling & blasting performance, which is a big concern in the underground constructions. From other side, the misalignment in the hole's drilling can lead to deviate the tunnel path where the rectifying cost is high. (Figure 1.2) A illustrates a scheme of one round of drilling & blasting process.

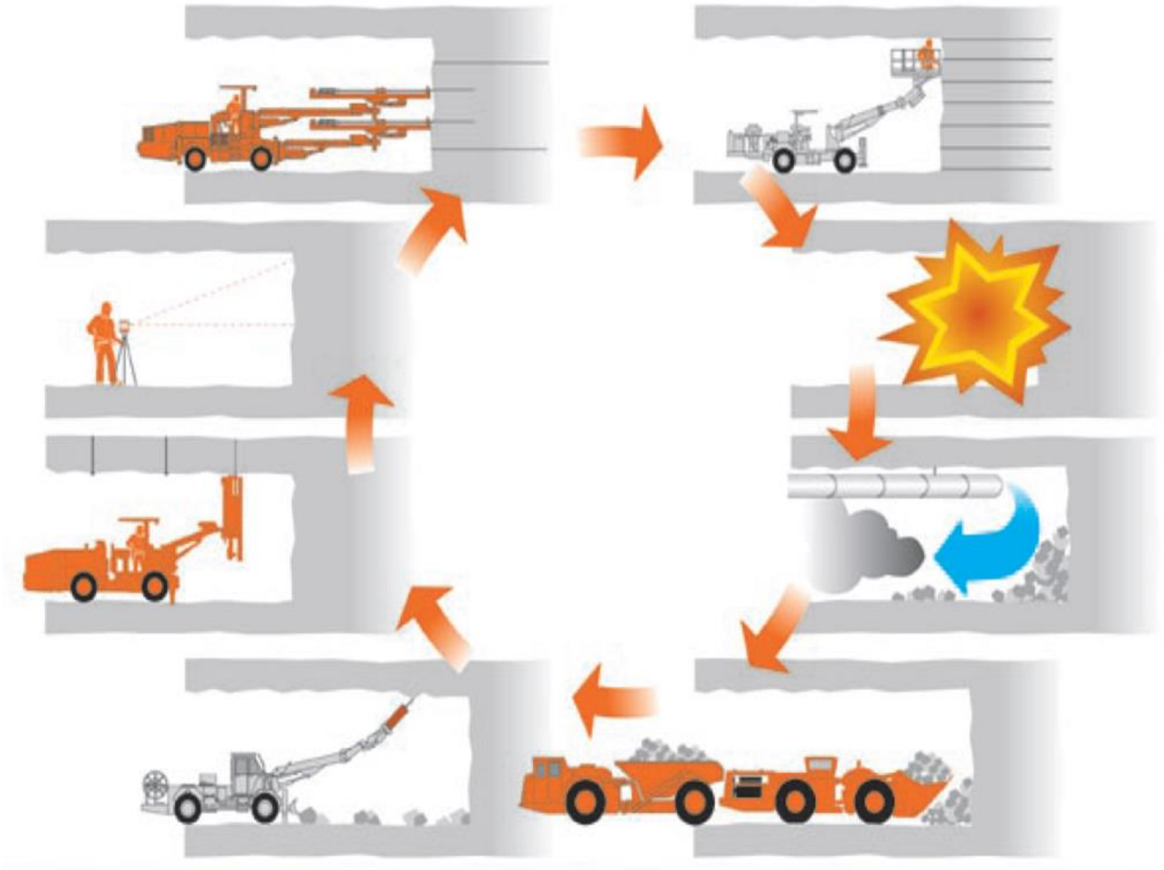

-

- *Figure 1.2: Drill and Blast cycle (Heiniö, 1999)*

Few of disadvantages of drill & blast method are summarized thereafter, which strongly restrict its use especially in the urban areas (Palmström, 1996):

- Production of unpleasant gases and smoke from the explosives, which often leads to poor working conditions for the crew.
- Vibrations on nearby structures.
- Rough surface gives head loss for water tunnels.
- The blasting creates new cracks in the rock, which leads to an increase need in the rock support.

Tunnel Boring Machine (TBMs)

TBMs belong to the mechanical family includes: (a) excavators equipped with ripper teeth, (b) hydraulic rams, (c) roadheaders and (d) TBMs of various designs.

The objective of TBMs is generally to shut off and break the hard rocks in fastest manner possible. Thus the concoction of rotating head made the TBMs more efficient and reliable than the primitive models conceptually based on the same principle as the percussion drill head. All successful modern tunnel boring machines are equipped with rotating grinding heads and cutting wheels.

Technically, the disk cutter produces the rock failure in shearing mode forming slabs (chips) of rock. The process begins by applying a pressure on these cutters against the rock face. This pressure pulverizes the rock and causes lateral crack to propagate towards the neighboring kerf. Thereafter the rock begins to be chipped. To get an optimal rendering, kerf spacing and cutter load should be suitably parameterized according to the rock type. (Heiniö, 1999) estimated these parameters to be standard as 80-110 mm for the space and 250 kN as cutter load for (430 mm) discs (Figure 1.3).

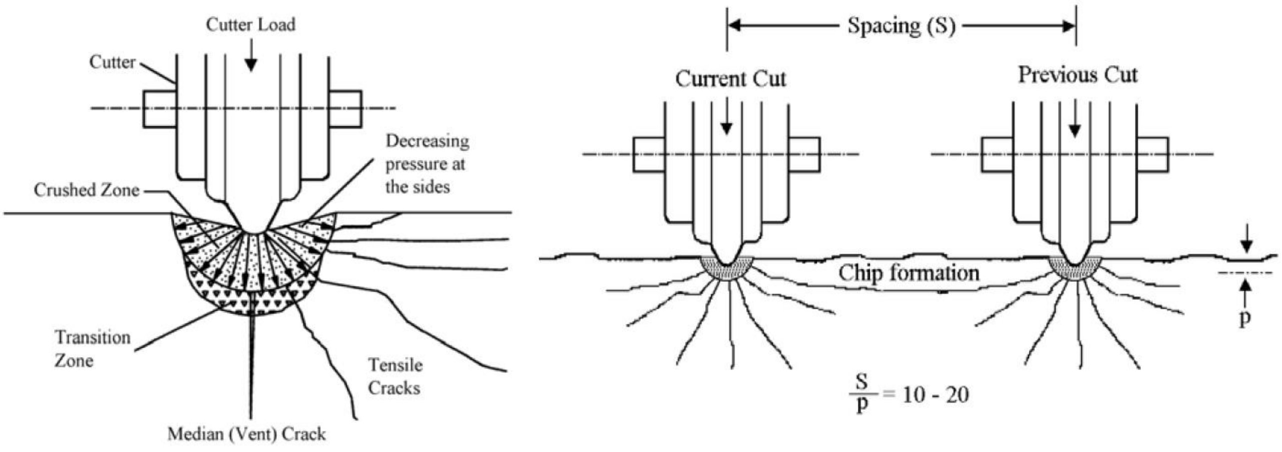

Figure 1.3: Cutting process in TBM (Herrenknecht,2003)

The performance of the TBMs is strongly associated to the compressive strength of the rocks. (Gong and Zhao, 2007) showed that the penetration rate decreases exponentially with the increase in the compressive strength of rock material (Figure 1.4).

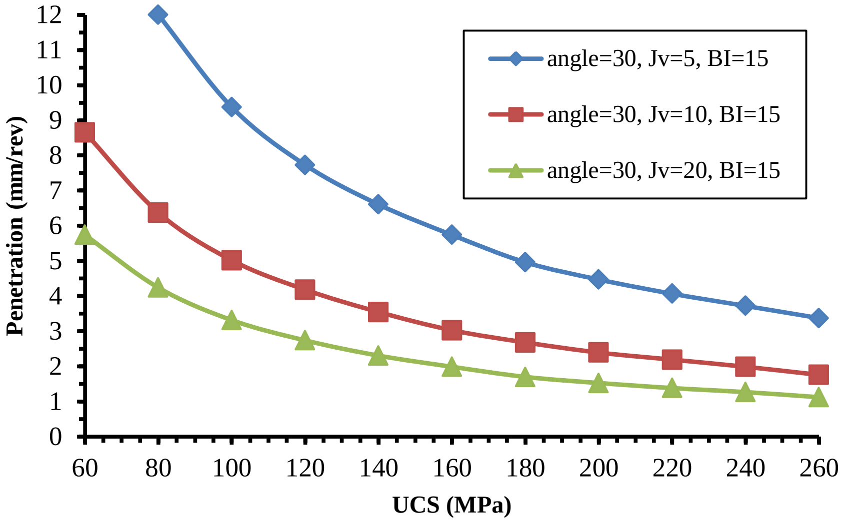

Figure 1.4: The penetration rate with the compressive strength (Gong and Zhao, 2008)

The “wipeout” is very costing phenomenon in tunneling by the TBM, which is pertaining to not detect the bearings failure so that the adjacent cutters becomes overloaded and prematurely fail and lead to a chain reaction of multiple cutter failures. The regular replacement of the damaged cutter is indispensable every stop of the TBM to avoid such complete failure of the cutters. The cutter on the left quit turning and wore flat. Figure 1.5 shows few damaged cutters those experienced a massive bearing failure that resulted in a damaged seal retainer.

Figure 1.5 : Some damaged cutters

TBM has the advantages of not disturbing the surrounding texture and resulting in a smooth tunnel wall. Besides the aforementioned things in following some of the significant advantages of using the TBM excavation are (Palmström, 1996):

- It requires less rock support.
- It gives smoother tunnel walls and reduced head loss in water tunnels.
- Longer tunnel sections can be excavated between adits.
- It has higher tunneling capacity.
- It gives better working conditions for the crew.

The disadvantages of TBM are summarized by (Palmström, 1996):

- More geological information from the pre-investigation stage is required.
- It is more sensitive to tunneling problems in poor rock mass conditions.
- It is a less flexible than drill & blast method.
- Only longer tunnel sections can be bored more economically (because of larger investment and rigging costs) than drill and blast.
- The TBM may get stuck under squeezing rock conditions.

The other major concern of the tunneling boring machine is the caused impacts to the whole rocky mass where the potential for rock falls, rock slides, or slow inward movement (squeezing) of the surrounding rocks are largely worrying the contractors. Consequently, the costs may become higher than predicted.

The above aforementioned concerns push the researchers as well as the engineers to enhance and even suggest new technologies. Those are able to affect the rock toughness as same as less destructive for the rocky mass and depend on the abrasive property of the rocks to efficiently drill it. However, for many years ago the emergent solution was the temperature to stimulate some kind of expansion leads to compressive stresses that cause the spallation of the rock.

1.3 Thermo-mechanical behavior of rock material:

This section includes two subsections: (1) analysis the thermal properties and their dependences on the temperature, (2) analysis the variation of physical characteristics with temperature and (3) analysis the influence of the temperature on the mechanical behavior.

1.3.1 The thermal properties:

Thermal conductivity

The thermal conductivity (λ) is defined as the material ability to conduct the heat. It is expressed by Fourier's law:

$$\frac{dQ}{dt} = -\lambda \frac{dT}{dx} \qquad \textit{Eq 1-1}$$

Where: dQ/dt is the rate of heat transfer; dT/dx the temperature gradient,

Almost all the rocks have basic values of thermal conductivity ranging between 0.1~15 (W/m.k) comparing to the metal materials of order of few hundreds (W/m.k). Relatively, the thermal conductivity is isotropic, but it could be anisotropic into fashions:

- Mineral anisotropy depending on the arrangement of mineral particles (lineation) in the rock sample, and
- Shape anisotropy, occurring parallel and perpendicular to the plane of bedding, foliation or schistosity of a rock volume.

The thermal conductivity of the rock materials generally decreases with temperature, (Figure 1.6). This reduction could reach 45% for the sedimentary rocks and about 40% for the magmatic and the metamorphic ones (Vosteen and Schellschmidt, 2003).

The thermal conductivity could be affected by the pore water content, porosity and the bulk density. The porosity negatively influences the thermal conduction due to decrease in contact surfaces between the grains, (Figure 1.7). The thermal conductivity increases as the grain's size increases (Tavman, 1996).

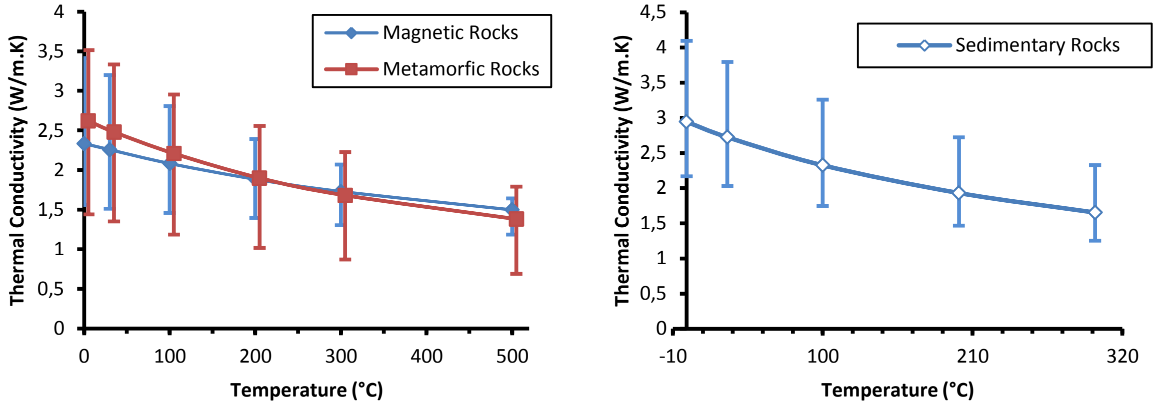

Figure 1.6: The composition and temperature effects on the thermal conductivity of the different rocks types (Vosteen and Schellschmidt, 2003)

Thermal capacity

The thermal capacity is the product of the rock density ρ and its specific heat capacity c_p. The latter ranges from 740 to 850 $J.kg^{-1}.k^{-1}$ for the magmatic and metamorphic rocks respectively. it could increase to 1050 $J.kg^{-1}.k^{-1}$ with increase in the temperature in the sedimentary rocks. In order to visualize the temperature dependence of the thermal capacity, the density of rock was considered as constant over the temperature range 1-300 °C (Vosteen and Schellschmidt, 2003). Tests revealed that the specific heat capacity follows an exponential variation with temperature (Figure 1.8).

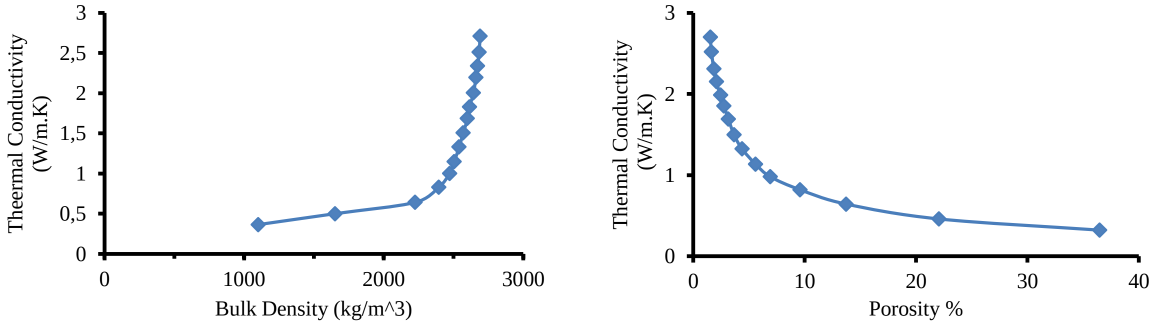

Figure 1.7: Thermal conductivity variation with the physical properties (Singha et al., 2007)

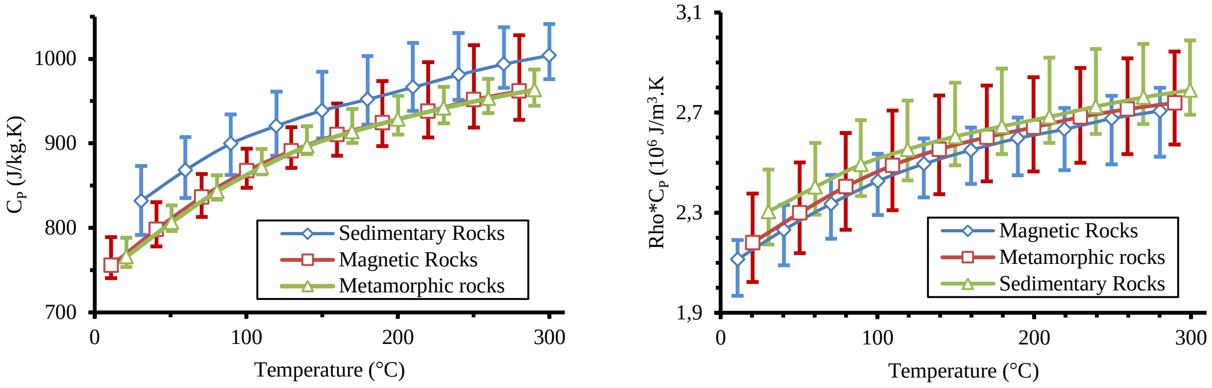

Figure 1.8: The specific heat capacity and the thermal capacity dependence on the temperature (Vosteen and Schellschmidt, 2003)

The thermal diffusivity

The thermal diffusivity describes the ability of a material to conduct thermal energy relative to its ability to store thermal energy. It is a function of thermal conductivity λ, the density ρ and the specific heat capacity c_p:

$$k = \frac{\lambda}{\rho . c_p} \qquad \text{Eq 1-2}$$

The thermal conductivity decreases with temperature while the specific heat capacity increases with temperature. Consequently, the thermal diffusivity decreases more than the thermal conductivity with temperature. In the temperature interval (1-300 °C), Vosteen et al. (2003) reported a decrease in the thermal conductivity between 25% and 44%, and decrease of 42–54% in the thermal diffusivity (Figure 1.9).

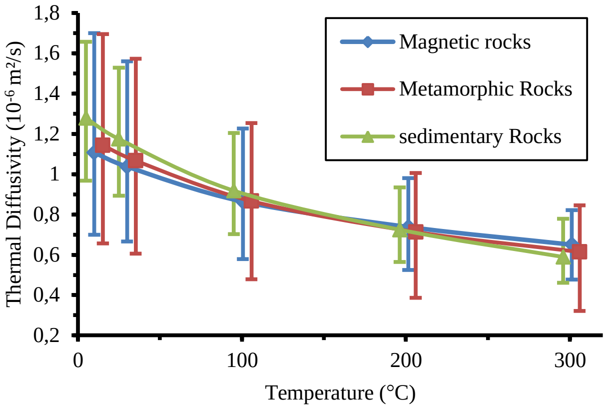

Figure 1.9: The thermal diffusivity vs temperature (Vosteen and Schellschmidt, 2003)

1.3.2 Thermal damage in rock Materials:

In order to understand the rock behavior under high temperature, this section presents the thermal damage, in particular the stress-strain diagrams, the development of micro-cracks with increase the temperature, the porosity and the permeability.

The damage in the mechanical behavior:

Compressive strength

Hommand-Etienne et al. (1989) used two granite types (Senones, Remiremont) to study the thermal damage in rock materials. The samples were heated slowly at a rate of 50 °C/h up to 300 °C. Thereafter the rate was increased to 100 °C/h to reach the maximum temperature. The maximum temperatures (200, 400, 500 and 600 °C) were maintained for 5 hr. Statistically, they noticed a very slight reduction in the compressive strength 400°C even in few samples the reduction reached 16%. Significant drop in strength is observed from 400 °C upwards that attained 44% at 600 °C.

Later, Takarli et al. (2006) conducted experimental work to investigate also the thermal damage in rocks. The physical and mechanical properties of the samples were measured by destructive and non-destructives tests. The samples were heated to the desired maximal temperature, and then maintained during 2 hours at this temperature to eventually cooled down to ambient temperature. The destructive methods revealed that the compressive strength decreased by 20% with maximum temperature between 105 °C and 500°C. This reduction reached 47% when the sample was heated up to 600 °C. As well, they reported a decrease in Young Modulus of 28% and 62% for maxi temperatures 500 and 600 °C respectively, (Table 1.1).

Table 1.1 : The mechanical properties after the thermal treatment (Takarli and Agbodjan, 2006)

The mechanical properties after the thermal treatment		
Temperature	σ_c (Mpa)	E (Gpa)
105 °C	244	75
300 °C	224	62
500 °C	194	54
600 °C	128	28

Tensile strength

Hommand-Etienne et al. (1989) described the tension test as more specific in determining the behavior of the thermally damaged Granite. This test is more sensitive to the increasing of the cracks (advantage of the direct loading of the cracks). Figure 1.10 (b) shows the decrease in the tensile strength that reached 75%. From 400 °C upwards, the reduction in tensile strength became more pronounced due to the increase in the density of micro-cracking. Furthermore, they reported that the tensile strength dropped more rapidly in the more coarse granular size than the fine size.

Hommand-Etienne et al. (1989) reported also that the treated sample exhibits kind of contraction in the lateral side at the beginning of the test and then start to expand till the failure. This behavior is totally differentiating from the non-treated sample one that contracts more and more till the failure in the side direction Figure 1.10(c).

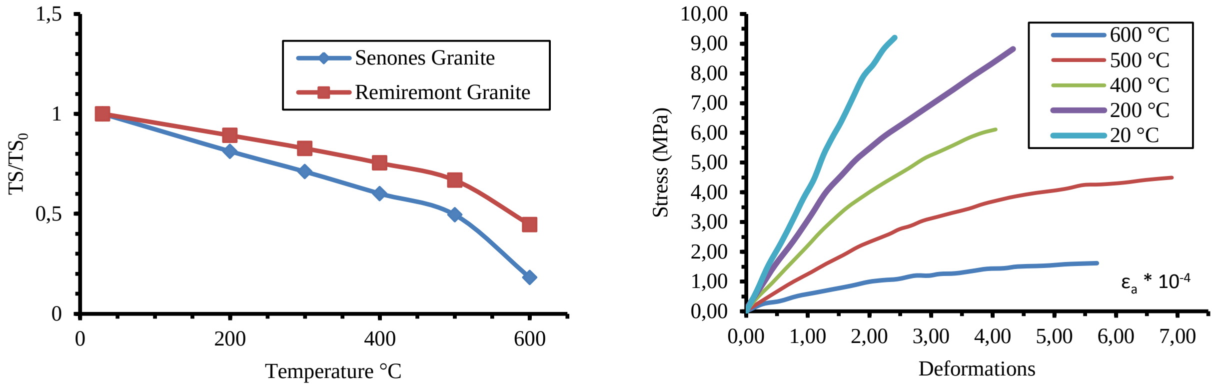

a) Tensile strength variation as a function of pre-cracking temperature

b) Tensile stress-axial strain

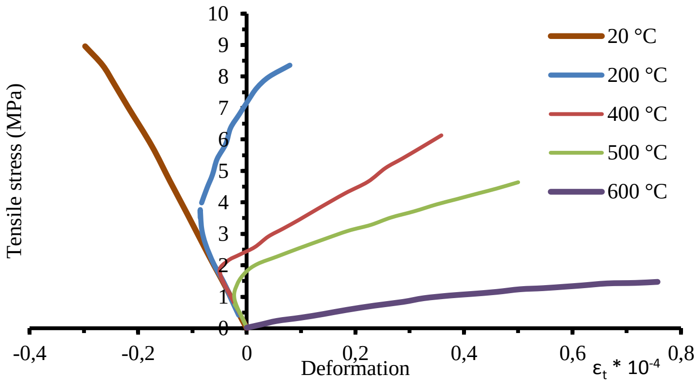

c) Tensile stress-lateral strain

Figure 1.10: The tensile strength variation with the heating treatment (Hommand-Etienne and Hourpert, 1989)

Damage at the microstructure level

The rock microstructure can be analyzed through three principal indicators: the length of the cracks, the width of the cracks and the crack density. Hommand-Etienne et al. (1989) conducted SEM observations to study the structural induced damage within the treated samples by using Stereoscan SEM 250. Quantitative and qualitative analyses were done to describe the cracks after the thermal treatment.

The **length of the crack** depends on the initial material structure, the shape and dimensions of the crystals. However, at 200 °C a rather notable similarity of inter- and intra-granular crack length modes is observed. Up to 600 °C, intra-granular cracking occurs particularly within feldspar where they propagate in straight lines following the cleavages (Hommand-Etienne and Hourpert, 1989).

Crack width remarkably increased with pre-cracking temperature. The intra-granular cracks are normally less open than the inter-granular ones. This width increases noticeably after the 200 °C. The crack exhibits the most significant increase in the width between the 500 °C and 600 °C, they reported.

The **density of cracking** increases with the intensity of the thermal treatment. Figure 1.11 shows the variation of the cracking with temperature for large grain size (Senones granite) and small grain size (Remiremont granite). For coarser grain, the inter-crystalline cracking is stronger than intra-crystalline up to 500 °C. But between 500 °C and 600 °C, the intra-crystalline cracks increase more than inter-crystalline ones. In fine grain size rocks, the inter-crystalline cracks are predominates over intra-crystalline ones, which is due to its small grain size, they mentioned.

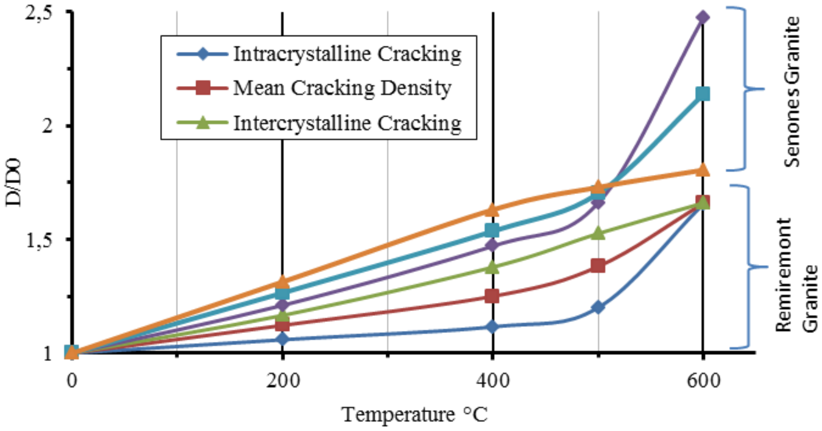

Figure 1.11: The cracking density with the temperature (Hommand-Etienne and Hourpert, 1989)

1.3.3 Influence of the thermal treatment on the physical properties:

The porosity

Chaki et al. (2008) reported that the porosity generally undergoes non-significant change between the 105 °C and 500 °C pertaining to the small structural modification at this range of temperature. The significant change in porosity happens between 500 °C and 600 °C where the rock witnesses an important increase in the open porosity because of existing cracks' growth (Figure 1.12).

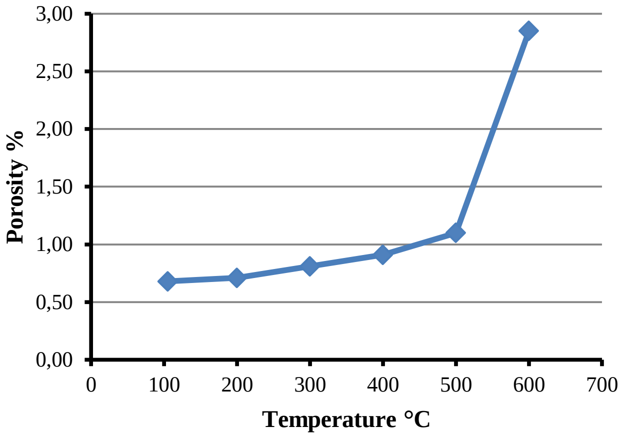

Figure 1.12: The porosity variation with the temperature (Takarli and Agbodjan, 2006)

The Permeability:

Chaki et al. (2008) stated a similarity between permeability behavior and the porosity one. The permeability exhibits weak variation between 105 °C and 300 °C. This variation becomes more pronounced between 300 °C and 500 °C. From 500 °C upwards, a rapid increase in permeability is recorded due to the important increase of the connected porosity (Figure 1.13).

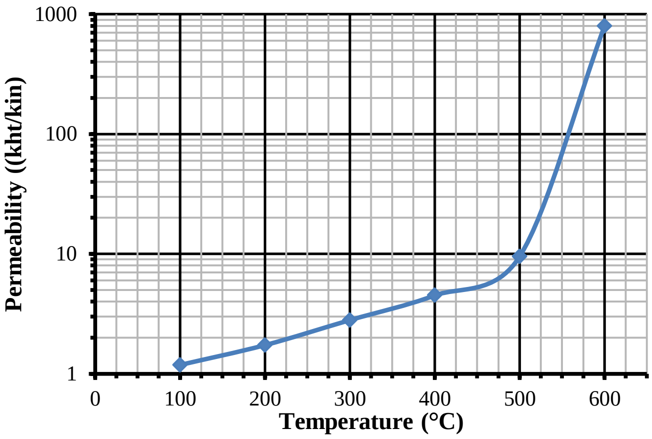

Figure 1.13: The permeability vs the temperature (Chaki et al., 2008)

The ultrasonic waves

Concerning the ultrasonic waves, Chaki et al. (2008) and Takarli et al. (2006) reported the following : a negative correlation between velocity and the damage induced by the heat treatment is observed. The velocity of waves undergoes a weak decrease (<12%) between 105 °C and 300 °C. Up to 500 °C, the velocity significantly drops down (more than 32%). Between 500 °C and 600 °C, the velocity values loses more than 63% comparing to intact samples (Figure 1.14 (a)). Chaki et al. (2008) recorded regular decrease in the central amplitude up to 500 °C. Between 500 °C and 600 °C, the energy amplitude of the ultrasonic waves suffered a disastrous decreasing (Figure 1.14 (b)).

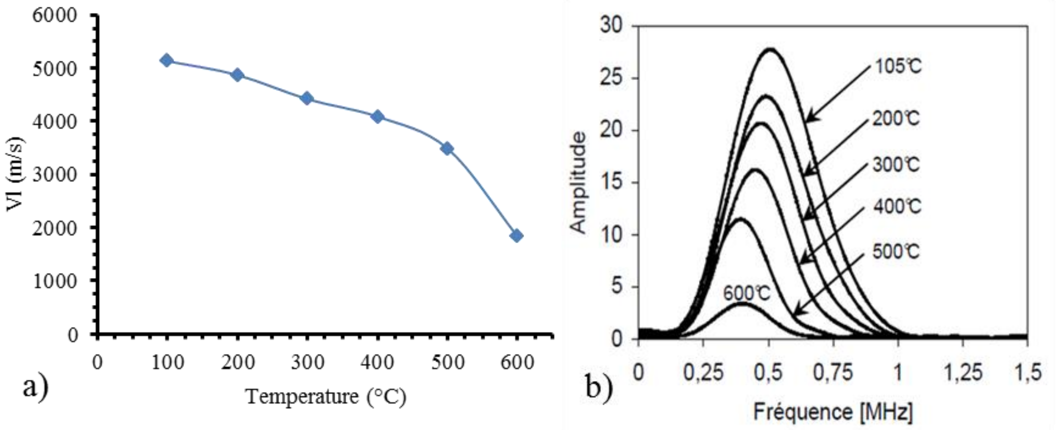

Figure 1.14: Evolution of longitudinal wave velocity vs temperature and the energy attenuation

1.4 Thermal spallation principle:

“Spall” as a word means to break something into smaller pieces, split or chip. Mechanically, spalling occurs at the surface of rock material when large shallow stresses are generated near to the surface. This form of spallation can be caused by freezing and thawing, thermal expansion and contraction. The thermal rock spallation was firstly designated by (Preston and White, 1934).

A strong thermal gradient develops at the surface of the rock as it is heated. Due to the low thermal conductivity and high specific heat, a restrain of the temperature in the exposed zone is produced. With this temperature confinement, the locally heated zone will largely expands comparing to the surrounding non-heated zone. Likewise, compressive stresses close to the surface are induced.

A more technical definition of thermal spallation was presented by Rauenzahn et.al (1989), "*spallation is to denote the generation of thin chips, often smaller than a single grain, liberated from a rock body perhaps three orders of magnitude larger in scale as a result of much larger heat fluxes (0.5-10MW/m²) over relatively short times scales (0.1-1 sec)*".

On the other hand, many hypothesizes were assumed to interpret the failure mechanism by thermal spallation. Rauenzahn (1986) and (1989) conducted a wide bibliographic study to analyze the previous works. Norton (1925) emphasized that thermal spallation is due to shear failure. Later this theory was sinned by Rauenzahn (1986) who considered it as built on fault physical basis.

In the same period, Preston et al. (1934) had corrected the vision of Norton and explained the failure as a result of micro-flaws generated during heating and originated from pre-existed flaws in rock body so that Preston assigned the failure to thin shallow slab buckling after the extension of the flaws due to compressive stresses (Figure 1.15).

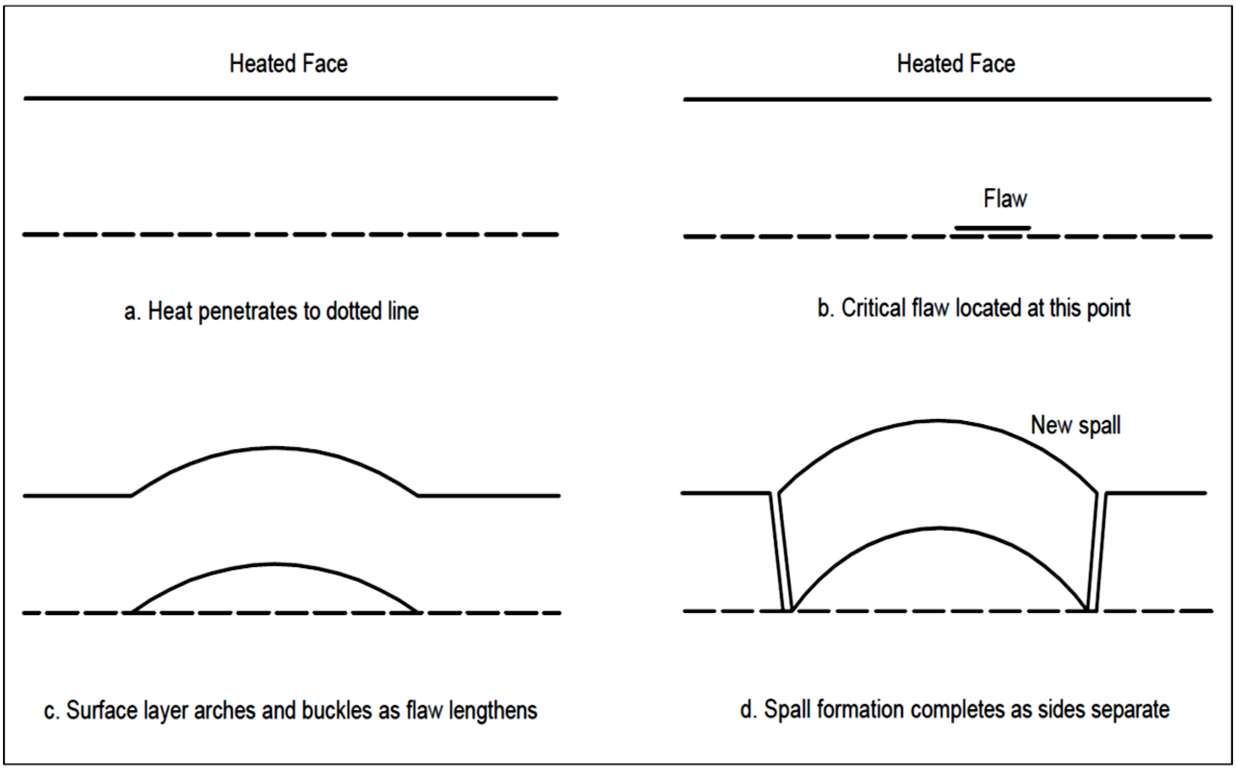

Figure 1.15: Simplified scheme of spall formation on surface of a semi-infinite solid (Rauenzahn and Tester, 1989)

Germanovich (1997) revisited the problem and showed that the compressive stresses are restrained in a thin layer near to the heated surface. Below this thin layer, a stable tensile stresses layer is formed (Figure 1.16). Some researchers described the failure by mechanical buckling mechanism profiting from crack growth around the compressive layer (Cherepanov, 1966) (Kill, 1967), cited by (Germanovich, 1997).

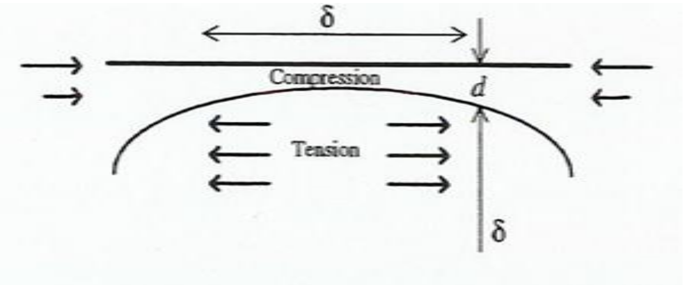

Figure 1.16: Schematic distribution of thermoelastic stresses in thermal spallation process (Germanovich, 1997)

Deeny et al. (2008) stated that the sharp thermal gradient results in compressive stresses close to the exposed surface related to the local thermal expansion and tensile stresses in the cooler interior regions. However, Preston suggested two crucial criterions for causing spallation:

- Localization effect: the heated zone must be relatively small compared to the whole rock surface: the ratio between treated zone and the rock surface is around 10% (Rauenzahn and Tester, 1989).
- Heating rate: the speed of the heat delivery to rock surface must be high; in such a way that the temperature of the treated zone increases compared to its diffusion to the surrounding zones (Rauenzahn and Tester, 1989). The heat source types and the delivery modes (conduction, radiation…) are crucial factors in thermal spallation process.

Another factor that influences largely the spallation process is the rock type, in particular, its physical as well as mechanical properties. Table 1.2 shows the rock spallapility according to the spalling rate and the temperature gradient.

Table 1.2: Average rock properties and spalling ratings of some rocks (Rauenzahn and Tester, 1989)

Rock	**Rating**	$\beta_t(\times 10^{-6})$	**E(GPa)**	$\rho.C_p$	ν	σ_c**(MPa)**	$\Delta T_s = \frac{\sigma_c(1-\nu)}{\beta_t.E}$
Basalt	Fair-Poor	4-5	30-50	2.5-3.3	0.22	80-300 (130)	560
Diorite	Good-Poor	6-7	35-70 (60)	3.4	0.25	100-200 (120)	230
Dolomite	Excellent	11-13	50-100 (70)	5.2	0.2	50-150 (100)	95
Gneiss	Good-Fair	5-9	20-70 (40)	2.5	0.22	150-200 (180)	500
Granite	Good-Fair	8-14	20-70 (50)	2.5	0.2	100-250 (200)	320
Limestone	Poor	8-11	10-70 (30)	4.0	0.20	10-200 (80)	230-700
Marble	Fair	7	30-80 (40)	2.5-2.7	0.30	60-200 (100)	250
Quartzite	Excellent	11-15	20-100 (50)	2.7	0.25	140-300 (200)	230
Sandstone	Good-Poor	10-13	7-40 (20)	2.5	0.27	30-250 (180)	550
Schist	Fair-Poor	6	40-90 (50)	2.7	0.15	10-200 (100)	140-280
Tuff	Poor	3-5	1-10	2.7	0.10	10-30 (20)	640

1.5 Experimental works

The first research experimental work aimed the analysis of the efficiency of thermal drilling spallation (TDS) versus the conventional drilling methods. Then, the experiments aimed at understanding the thermal spallation mechanism, specify the geometrical characterizations of the produced spalls, optimize the heat flux, determine the temperature beyond what the spallation takes place, required stresses and exposure time to spall the rock surface, rock type effect on spallation process, evaluate the rate of penetration (ROP) and the influence on the physical properties of the rocks (porosity, permeability…).

Experiments were conducted firstly on the ceramics materials and then they were enlarged to brittle materials as granite (Rauenzahn and Tester, 1989). Norton (1925) was the pioneer in calling the thermal shock failure “spall”. He applied on similar clay material bricks sudden cooling after been heated. He observed inclined fracture plains by 45° to the heated surface, while he got perpendicular tensional cracks to the cooled surface (resumed by (Rauenzahn, 1986)). Then after, a contemporary of Norton, Preston et al. (1934) pointed out the spallation principle when he illustrated that the spallation occurs due to stresses acting on flaws parallel to the heated surface. Likewise, he was able to produce thin lamellar in fireclay spheres.

1.5.1 The Laser as heat sources

Few years later, Farra.G (1968) conducted analytical and experimental work on the interaction between laser CO_2-N_2-H_e (10.6 µm) and the rock material. He observed the mechanical response of irradiated marble and granite samples. He reported that the failure induced by laser irradiation is due to a combination of several causes:

- Inter-granular separation due to phase transformation.
- Gross Chemical changes.
- Inter-granular corrosion.
- Gas or water pocket expansion.
- Inter-granular separation due to anisotropic thermal expansion.
- Thermally induced stresses leading to failure in compression or tension.

Experimentally, he deduced that the cracking of samples is due to tensile stresses in tangential direction where the cracks are formed and propagated in the radial direction of the specimens (Figure 1.17). The cracks are related to the maximum tangential stress position beyond the irradiated zone.

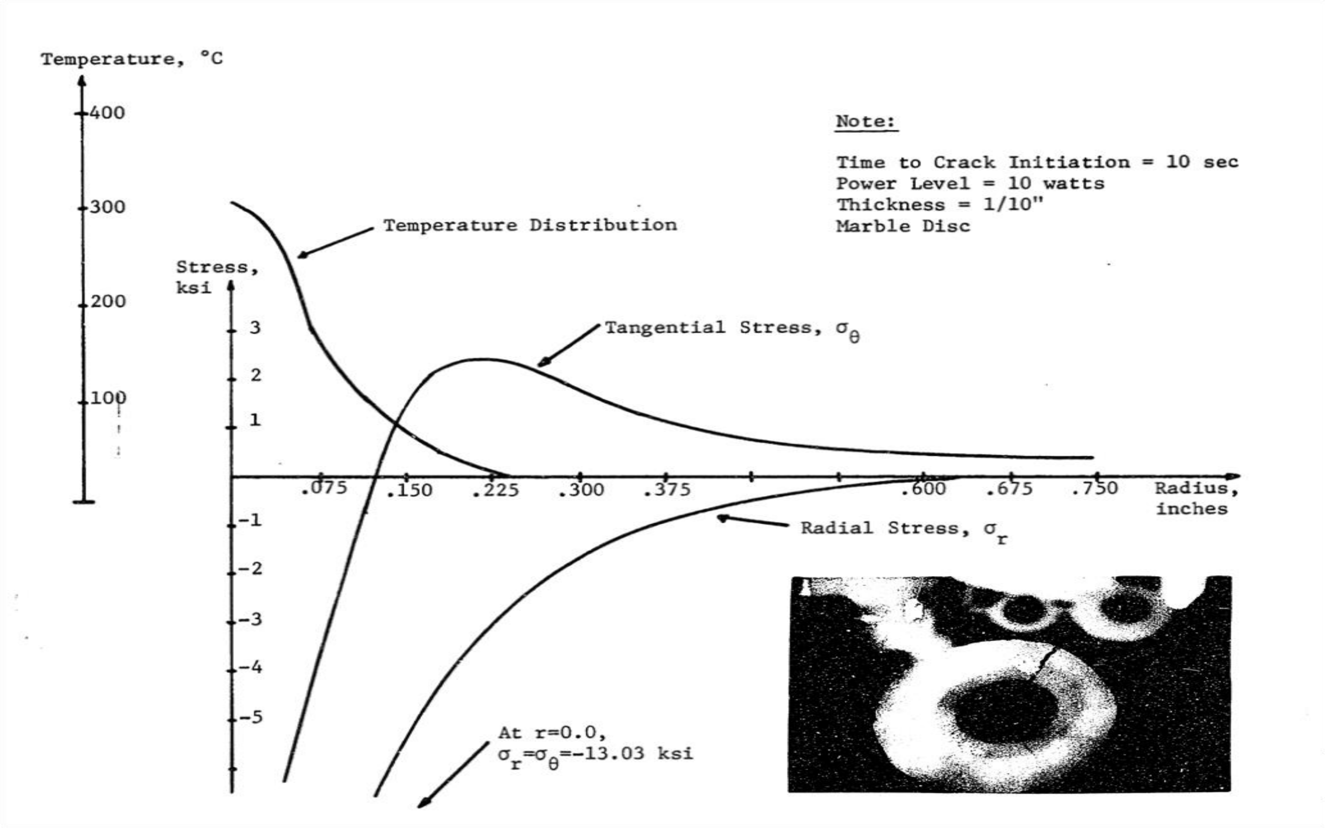

Figure 1.17: Membrane stresses as a function of radius at time of crack initiation (Farra, 1968)

He introduced a new parameter (Disc Tensile Failure Energy (D.T.F.E)) which represents "*the amount of laser energy input required to cause tensile failure in a rock disc divided by the volume of the specimen*":

$$D.T.F.E = \frac{Laser\ power\ \times Time\ of\ lasing}{\pi.R^2\ \times Specimen\ thikness}$$

He noticed that in the large discs shaped specimens, irradiated with laser power of 300 watts on a spot of 2.5 cm as diameter, the cracks were initiated after 9 seconds. In other words, a radiation of 0.4 MW/m^2 was needed to induce 72 (MPa) as compressive stress in the center of the exposed spot (Farra, 1968).

Later, Rauenzahn et al. (1989) emphasized that the radiation needed to cause the fragmentation of rock material varies from 0.5 to 10 MW/m^2. He conducted two series of experiments by using two heat sources: the Propane and the Laser.

In the propane tests, two types of granites were used (Westerly, Rhode Island and Barre, Vermont). The high heat flux is provided by the combustion of propane and oxygen. Tests were followed by using a high speed videotaping camera (Spin Physics 2000 video system). The objective area was of size of 7.5 cm square. The torch is perpendicularly located over the rock surface and at a distance of 15.2 cm or 20.8 cm. More details could be found in (Rauenzahn, 1986).

Spallation occurred after 2 seconds of exposure. The process had been held to zone of 8-10 cm in diameter was damaged by spallation. The ejection of spall was violent so that the spalls were jumping few feet upward. Spalls had chips shape, 10-20 grains in diameter and one to two grains in thickness. 500 °C at the surface was attained within less than 2 seconds.

Rauenzahn (1989) conducted few series of spallation by laser as heat sources. He used the CO_2 with wave length of (10.6 µm) to irradiate blocks of granites sawed from the same blocks used in flame-jet tests. The heating rate was approximately 1.4 MW/m^2 on 15 mm spot diameter where the initiation of the spallation began after 0.1 to 8.0 seconds. Moreover, he noticed that the spalls were more peeled away than ejected from the rock. A partial melting in the lased zone is referred to biotitic mica existence, which prevented the chips to leave the rock surface easily. Thermally, the spallation temperatures were notably higher than those in flame-jet tests (Table 1.3).

Table 1.3: Spallation Temperature in Laser and Flame-jet tests (Rauenzahn and Tester, 1989)

		Barre Granite	**Westerly Granite**
Flame-jet		472 (K)	473 (K)
Laser	100 (W)	710 (K)	520 (K)
	200 (W)	--	1120 (K)

Xu et al. (2003) conducted thermal spallation tests on Berea Gray sandstone and shale. Those samples were irradiated by 1.6 kW pulsed Nd:YAG laser. They showed that each rock type has appropriate laser beam characters to be spalled by. They specified the notion of specific energy (SE) as "*required energy to remove a unit volume of rock*". Likewise, they conducted linear tracks test that to primarily identify the laser-rock interaction zones. For Berea gray sandstone fives zones were distinguished:

- Significant melting/ strongly bonded glassy phase.
- Surface melting/cracked glassy layer.
- Scattered surface melting/weakly bonded material.
- No visible melting/material removed by thermal spallation.
- Surface scorch/no material removed.

For shale three zones were identified: deep melting/strongly bonded glassy phase, surface melting/crashed glassy layer and no visible melting/thermal spallation (Figure 1.18).

Two important factors determine the material removal rate: the maximum temperature and temperature cycling frequency. Xu et al. (2003) reported that fracture could occur with thermal stress lower than the failure strength of the rock because of the cyclic nature of the pulsed laser which causes a cyclic compressive/tensile stresses in the rock material.

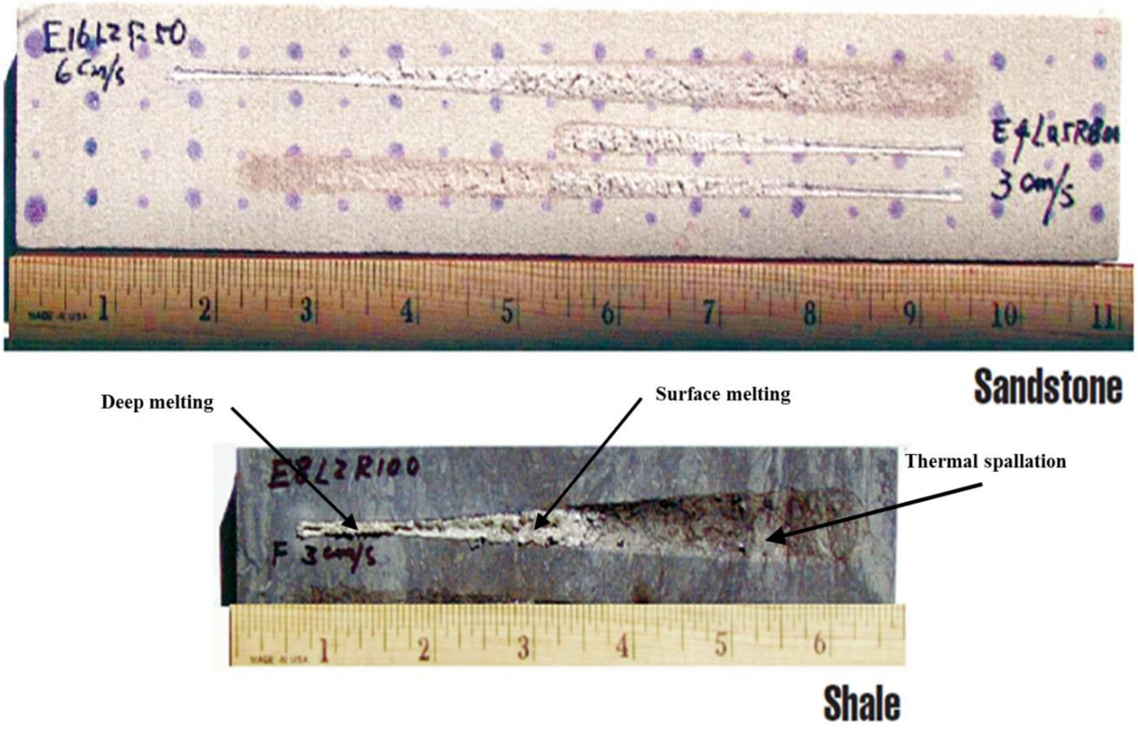

Figure 1.18: Linear tracks tests and the identified zones (Xu et al., 2003)

Xu et al. (2003) reported the threshold of laser irradiance of 9.2 MW/m^2 and 7.84 MW/m^2 for samples of Berea Gray sandstone and shale respectively. In the correspondent exposed zones they reported a total material removing by the thermal spallation.

Xu et.al (2004) obtained a hole of 25mm diameter and 100 mm in depth by using laser density of 14.15 MW/m^2 in 80 seconds. The elevated penetration rate was obtained by utilizing the pulsed laser burst method (1.6 KW pulsed Nd:YAG). They demonstrated that the thermal spallation enhances the rock permeability up to 566% compared to non-lased samples (Figure 1.19). The huge increase in the permeability resulted from the clay dehydration and micro-fractures. The micro fractures were related to high temperature gradient as well as the transition phase suffered by quartz in sandstone.

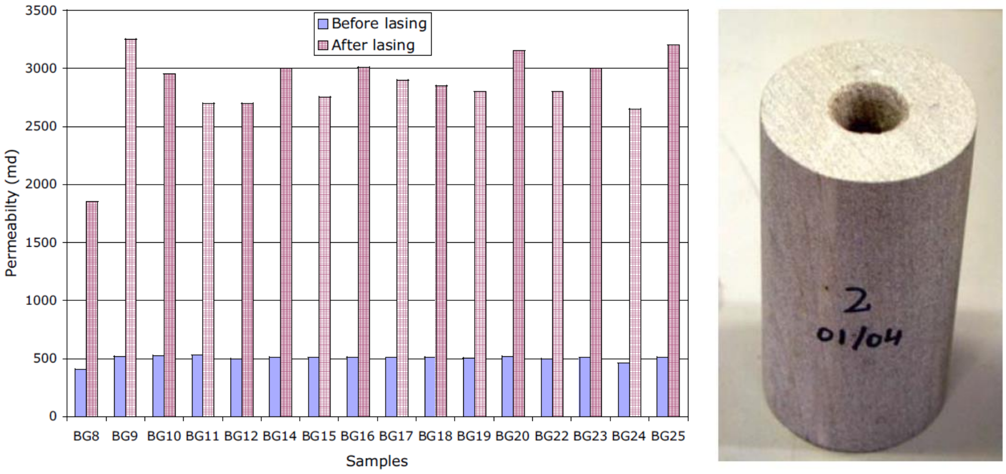

Figure 1.19: increased permeability in lased samples (Xu et al., 2004)

Ahmadi et al. (2011) (2012) examined two essential issues the exposure time and the effect of saturation on the spallation efficiency as well as the saturation liquid type. Granite and limestone samples saturated by water and heavy oil were tested. A laser density 4.85 MW/m^2 was used to obtain a hole with depth 7.2 mm in 25 seconds on the dry granite samples. They reported that further laser energy was required for the saturated rock either by water or heavy oil. A slight decrease in the rate of penetration (ROP) can be associated with rock saturation. Figure 1.20 shows the variation of (ROP) with specific energy (SE) and the saturation type.

Ahmadi et al. (2012) addressed the problem of confining pressure and its effects on the performance of laser perforation process. The confining pressure affects negatively the (ROP) and increases the (SE). This effect is related to an increase in the thermal conductivity of the rock because of the closure of the gaps between rock grains, which decreases the thermal stress. The local confining of the temperature in the treated zone is lost by the increase in the thermal conductivity as Preston’s description recommends.

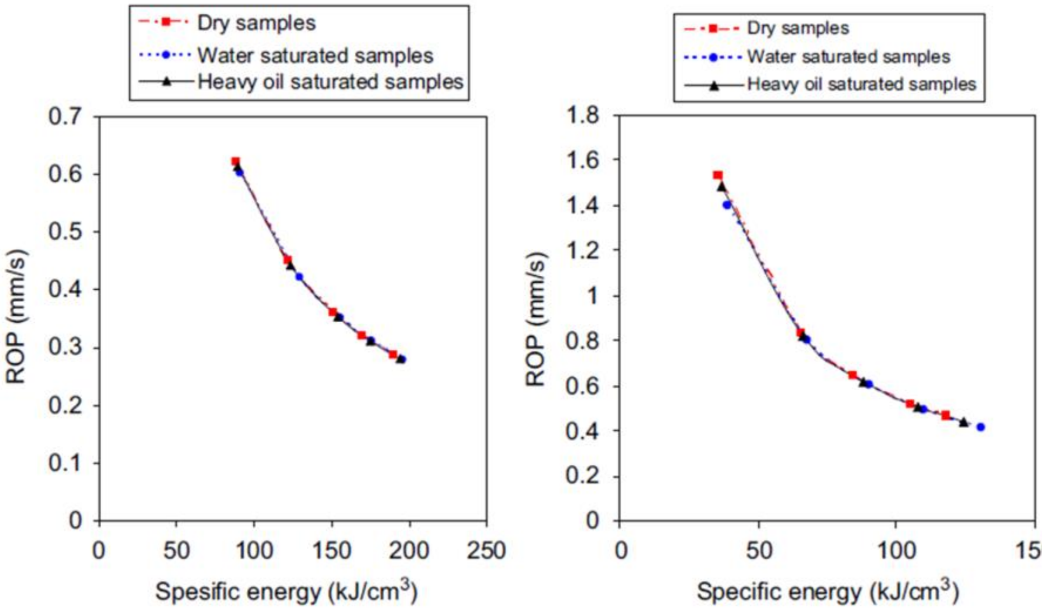

Figure 1.20: Variation of ROP according to SE and saturation liquid type (Ahmadi et al., 2011)

Ahmadi et al. (2012) showed that the confining pressure increases the strength of the rock so that the thermal spallation becomes more difficult. Figure 1.21 shows the variation of the (ROP) with the confining pressure for different saturation types.

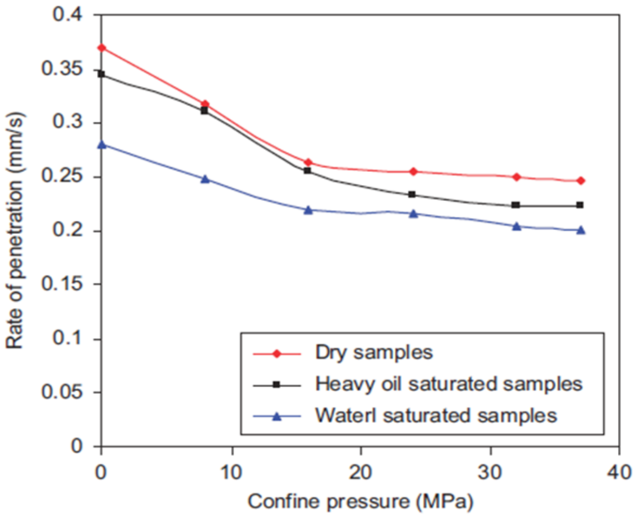

Figure 1.21: ROP variation with confining pressure in Granite (Ahmadi et al., 2012)

1.5.2 Microwaves as heat source

The microwave drilling was much less addressed than laser drilling technologies. Jerby et al. (2001) assembled an apparatus for drilling process (Figure 1.22).

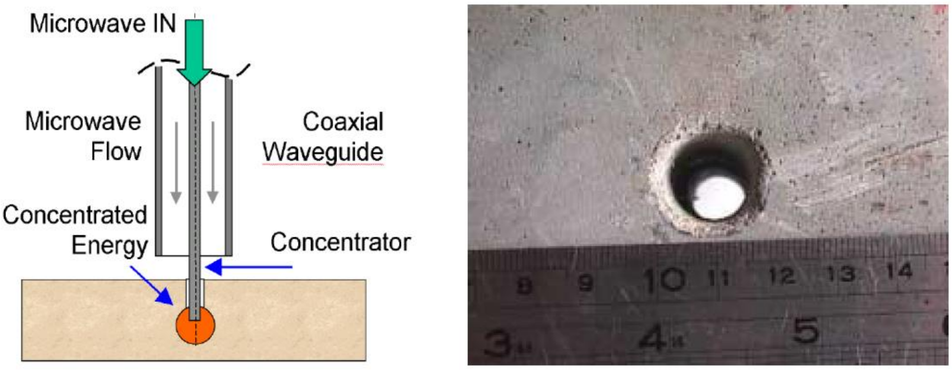

Figure 1.22: Scheme of the microwave drilling apparatus and configured hole (Jerby and Dikhtyar, 2001)

The process included softening or melting the material and then the use of concentrator pin for drilling.

Lmdroth et al. (1991) invented a method of hard rock cutting assisted by microwave by combining the thermal weakening (by microwave radiation) with a mechanical cutter. The energy deliverance is done by irradiation with waves frequency ranges from 900 MHz to 300 GHz (Figure 1.23).

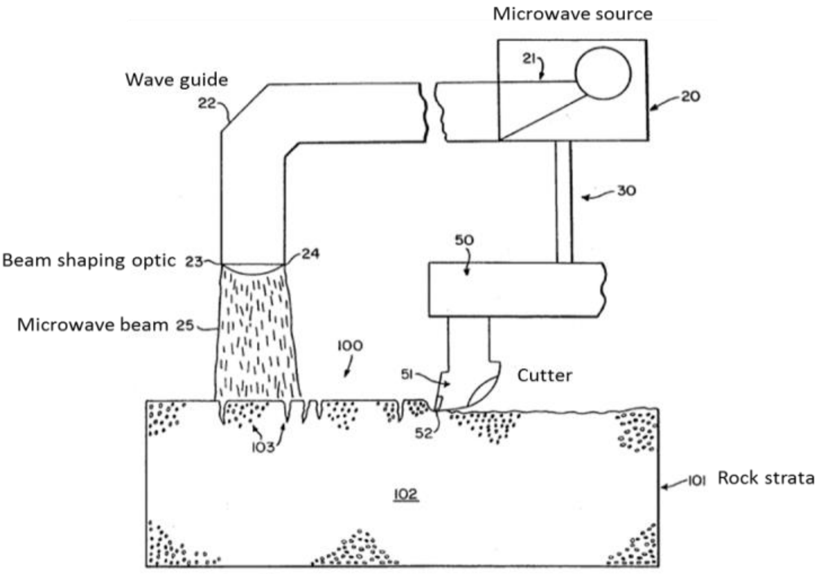

Figure 1.23: Schematic illustration of thermally weakening rock by microwaves (Lmdroth et al., 1991)

1.6 Numerical Modeling of thermal spallation:

Researchers tried to model thermal spallation process using thermo-elastic stress analysis where the stresses are related to the temperature's change:

$$\sigma = -\alpha . E . \Delta T \qquad \text{Eq 1-3}$$

α is the thermal expansion coefficient of the material, E is the Young Modulus and ΔT is the change in the temperature of the rock surface.

Germanovich (1997) modeled the thermal spallation through 2D micromechanical model. The thermal spallation was attributed to "*successive growth of inherent cracks in the surface layer subjected to high thermo-elastic compression*". Two micro-cracks densities near the heated surface were used during the modelling: high micro-cracks concentration and low one. Accordingly the critical temperatures for crack propagation initiation were introduced.

$$T_{g\ high\ concentration} = \sqrt{\frac{\pi}{a_0}}\,\frac{K_{Ic}(1-\nu)}{\alpha E} \qquad \text{Eq 1-4}$$

$$T_{cr\ low\ concentration} = \frac{K_{Ic}(1-\nu)\sqrt{\Delta}}{2ka_0\alpha E} \qquad \text{Eq 1-5}$$

$2a_0$ is the crack length, $k = \frac{2}{3\pi}$, Δ is the distance between the center of the inclined crack and the heated surface, K_{Ic} is the stress intensity factor of mode I.

He found that the critical temperature in low micro-cracks density case is higher than high micro-cracks density one. This also can be drawn consequently for the critical stresses. He demonstrated the influence of geometrical characteristics of pre-existed cracks on the critical spalling temperature and penetration rate (Figure 1.24).

(Figure 1.25) shows two important issues: the first is the thermal spallation can reach the same rate of penetration as the conventional methods. The second is to reach this (ROP), it is necessary to attain elevated temperature near to melting rock one.

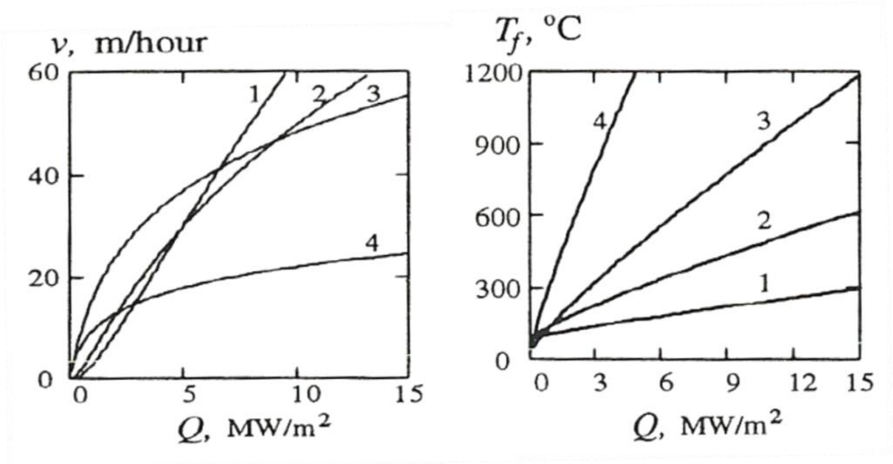

Figure 1.24: Dependence of penetration rate and free surface temperature on the rock structure, (1) $2a_0$*=0.1 mm,* Δ*=0.158 mm, (2)* $2a_0$*=0.1 mm,* Δ*=0.5 mm, (3)* $2a_0$*=1 mm,* Δ*=1.58 mm and (4)* $2a_0$*=1 mm,* Δ*=5 mm*

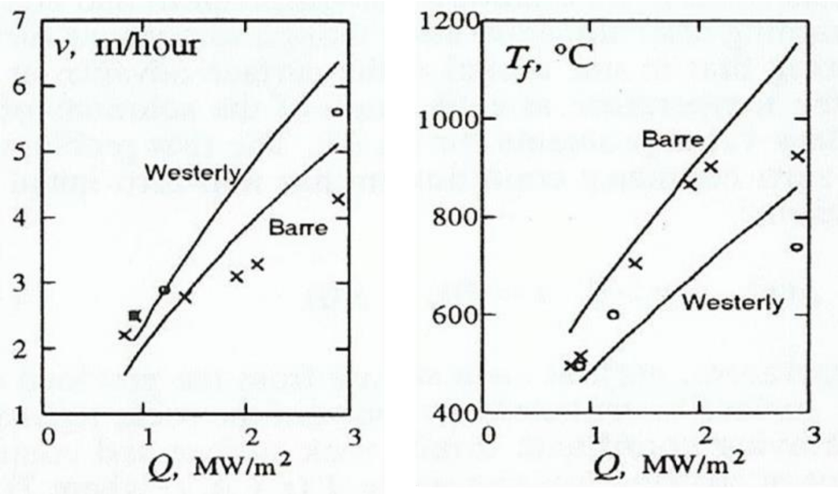

Figure 1.25: Velocity of spalling front advance and surface temperature at the moment of spalling (Germanovich, 1997)

Germanovish (1997) stated that the material spallability is function of two factors the material type as same as the heat flux. He reported that "*the same material can be non-spallable, poorly spallable or highly spallable if the heat flux varies*".

Xu et al. (2005) used the Finite Difference Method to simulate the thermal spallation by laser. They supposed that the rock spallation takes places every 0.15 seconds. Mathematically, the time difference thermo-elastic stress strain is expressed as following:

$$\dot{\sigma}_{ij} = \lambda\delta_{ij}\dot{\varepsilon}_{kk} + 2\mu\dot{\varepsilon}_{ij} - (3\lambda + 2\mu)\alpha\dot{T}\delta_{ij} \qquad \text{Eq 1-6}$$

Where δ_{ij} is Kronecker's delta, $\dot{\varepsilon}_{kk}$ is the mean strain rate, λ, μ are Lamé elastic constants.

They alternated the removed rock density by air density to mimic the removal process. The treated zone diameter was 10 mm similar to laser spot size. The obtained penetration depth was 3 mm comparing to 4 mm recorded in the experiments. The optimal energy viability is corresponding to 0.45 seconds as laser-on time (Figure 1.26).

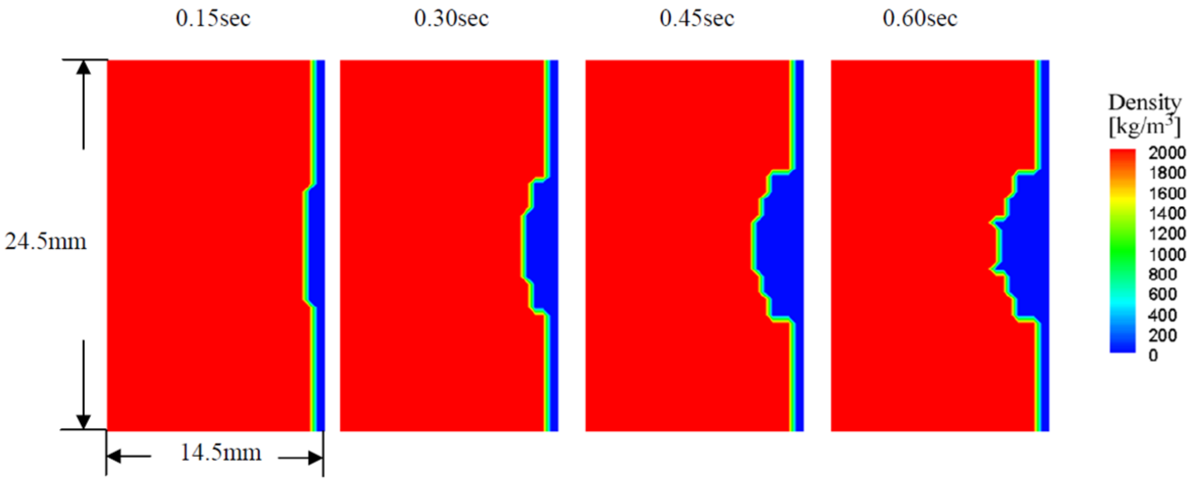

Figure 1.26: Removed rock material for different Laser-on time (Xu et al., 2005)

More than 1500° K (~1227° C) was reached within 0.45 seconds, which is above the melting temperature of almost of the rocks types. On other hand, stresses greater than 200 (MPa) were reported (Figure 1.27).

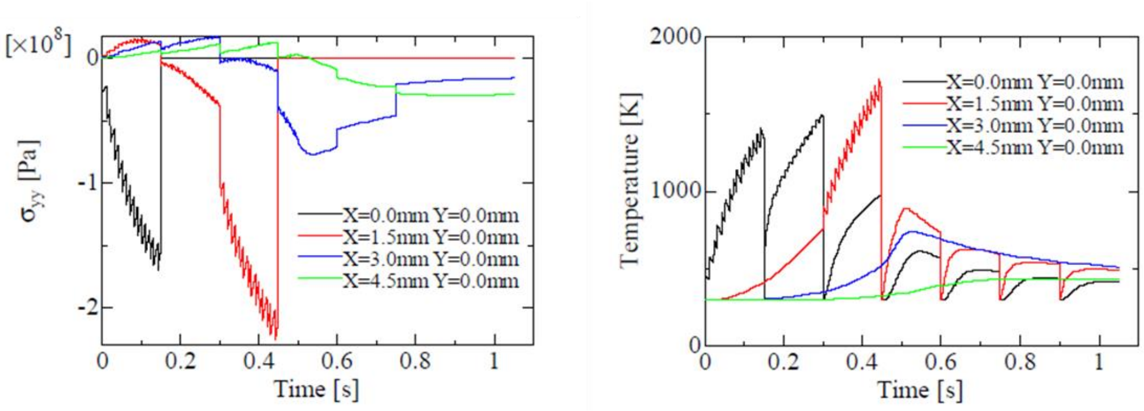

Figure 1.27: Temperature and stress profiles (Xu et al., 2005)

Walsh et al. (2011) (2012) (2013) addressed thermal rock spallation by investigation the heterogeneity influence. They suggested an explicit model to describe the spallation mechanism at the grains scale. Voronoi cells method was used to produce the rock heterogeneity. A set of randomly distributed points in the space was deployed, since then the bodies of the minerals are formed iteratively according to criterions related to their desired volumes. They considered an elastic perfectly plastic behavior for the grains. The thermal induced damage in the grains was predicted by using Johnson-Cook rule:

$$D = \int \frac{|d\varepsilon_p|}{\varepsilon_f} \qquad \text{Eq 1-7}$$

Where: ε_p is the plastic strain and ε_f is the strain at failure.

Considering that the heat transitions in rock is slower than the mechanical fracture one, they "*artificially*" increased the thermal conductivity of the rock by a factor of (10 000) without modifying other thermal properties. They supposed a gradual heating of the surface by flame-jet or hydrothermal techniques. The model was implemented in GEODYN software to simulate the spallation of Granite. More numerical details can be found in (Walsh et al., 2011). They modeled the grains interface (inter-granular contact) by a "*separate, weaker material*" with deduced behavior from (Lockner, 1998) (Lan et al., 2010).

They showed that the fracture occurs within the grains as well as at the inter-contact materials. The spall thickness is reported less than one grain diameter (Figure 1.28).

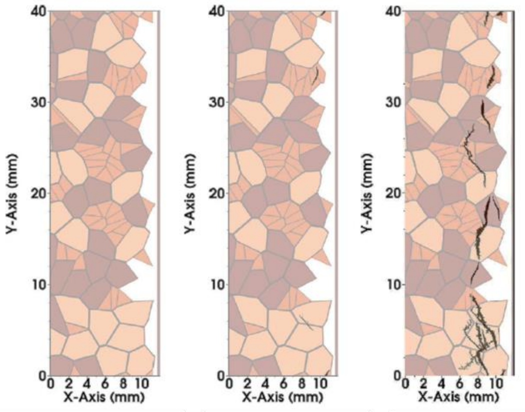

Figure 1.28: Fracture initiation and propagation during heating process (Walsh et al., 2011)

They assured that high surface temperature is behind fast spalling initiation and producing small fragments. The influence of heated surface shape (flat or rough) on spalls geometry and how fast the spalls are produced was showed. They mentioned that the flat surface is less probable to fracture than the rough one (Figure 1.29).

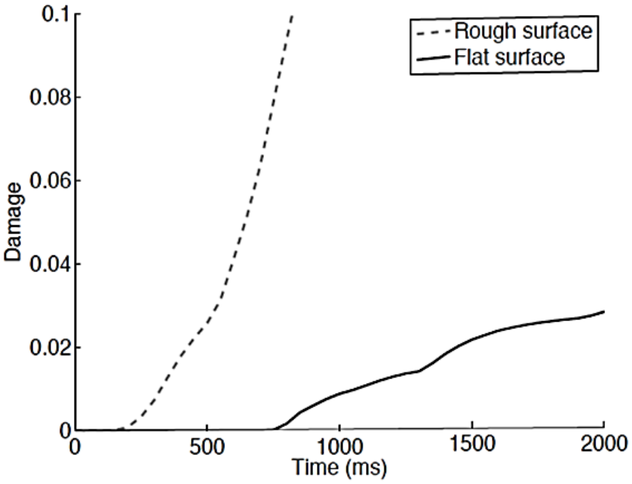

Figure 1.29: Damage comparison between flat and rough surface, (Walsh et al., 2011)

Walsh et al. (2011) confirmed that the confining pressure contributes in larger spalls size production but without increase in the penetration rate. This result is in accordance with the experimental works of Ahmadi.

The numerical analysis demonstrates that the heterogeneity of the rock is not the sole cause of the spallation process. They evoked the huge impacts of micro-porosity the water content in the closed pores in increasing the buckling risk. Walsh et al. (2013) proposed a new understanding of the traditional thermal rock spallation assisted by buckling theory by adding additional factor such as micro-pores and the water content (Figure 1.30).

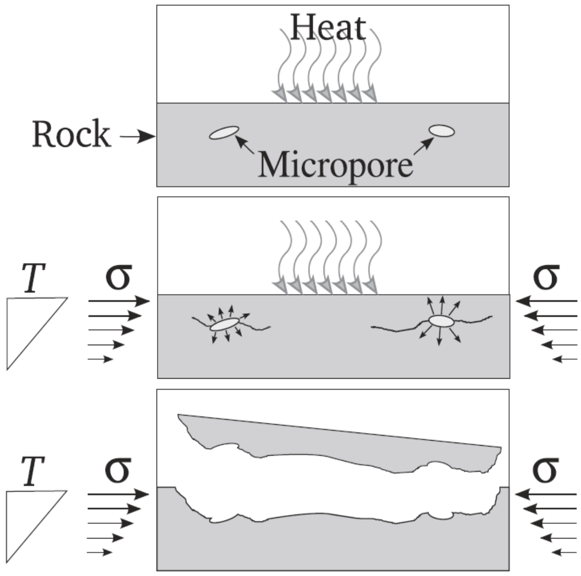

Figure 1.30: Pore-fluid enhanced spall-production model: the micro-pores serve as site for fracture initiation caused by the rapid heating. The expansion of fluid within the pores aids in fracture propagation. Fluid expansion and buckling cause the spall to be removed from the surface. (Walsh and Lomov, 2013)

1.7 Conclusion

In conventional tunneling methods, efforts are principally focused on support services as well as casting process more than on drilling operation itself. As well, the tripping process of produced debris away from the work site forms an environmental and funding challenge for operators. Additional cost is related to replacing damaged and stuck drilling bits within the rock strata, which could be reduced by use of the thermal spallation technique. The thermal rock spallation process could present some advantages regarding the mechanical and blasting methods, mainly minimizing the capital time and money costs. The performance of this method could be significantly improved using the Laser technique (Olaleye B, 2010).

In the field of thermal spallation, both the experimental and the numerical works reported the use of heat radiation density of (1~14 MW/m^2), which is recommended as ideal irradiation density to spall a rock. This high relative irradiation intensity is a result of the force needed to propagate the pre-existed flaws nearby the treated surface. Consequently, high level of stresses must be exerted on the tips of flaws to then after enlarge them until the plate failure by buckling.

However, the thermal spallation technique still encounters some barriers, in particular the increase in the penetration rate and the minimization of the energy used in this process. In the following chapters, we will propose a process which is based on the use of heating/cooling cycle, which will improve the performance of this process.

CHAPTER 2

LABORATORY INVESTIGATION OF THE ROCK-LASER INTERACTION

2.1 Introduction:

This chapter presents a laboratory study of the interaction between the rock material and a laser radiation. The study is conducted using the laser Nd:YAG, which operates with wavelength of 1064 nm and a maximum optical power of 620 Watts . Different laser power parameters will be tested. This study aims at:

- Describing the mechanism of rock removal using different laser power parameters.
- Exploring the influence of the velocity of the laser nozzle on the removal rock mechanism.
- Analyzing the damage localization due to the laser treatment.

The experiments were conducted in cooperation with the Team of the University of Artois (IUT Béthune) of the Laboratoire de Génie Civil et géo-Environnement (LGCgE).

2.2 Experimental procedures:

This section presents on the rock material used in this research as well laser drilling system and the laboratory results.

2.2.1 Rock Materials

Tests were conducted on granite Fontainebleau samples. The samples dimensions are 40mm in length, 230 mm in with and 20 mm in thicknesses. Table 2.1 summarizes the physical properties of this rock.

Table 2.1: The thermal and mechanical properties of the tested Granite

Material properties	**Density**	**Thermal conductivity**	**Specific heat**	**Thermal expansion coeff**	**Young Modulus**	**Poisson ratio**
	Kg/m^3	W/m.K	J/kg.K	1/K	GPa	
Granite	2600	1.8	930	$7*10^{-6}$	60	0.25

2.2.2 Laser drilling system

Laboratory tests were conducted using the Laser Nd:YAG, which operates with a wavelength of 1064 nm, a maximum mean laser power of 250 W, a pulse duration between 2-20 ms and pulse energy varies between 0 to 20 Joule. The focal length is equal to 75 mm with a 250 μm minimum spot size. The frequency ranges between 10 and 12 Hz. No specific set up was used to defocus the laser beam to the desired spot sizes. The end of the nozzle was at 1 cm distance from the rock surface. Some tests were conducted on a fixed sample and a moving laser nozzle.

Figure 2.1 shows the experimental setup that contains the laser machine, the power generator and the system of the sample fixation under the nozzle. Table 2.2 provides the measured parameters during the linear track tests.

2.2.3 Experimental program:

The experimental program includes three groups:

- Group 1: Experiments conducted with fix laser head and different laser power parameters (tests: 1to 4).
- Group 2: Experiments conducted with moving laser head (constant velocity) in addition to different laser characteristics (tests: 5 to 8).
- Group 3: Constant laser power level and variant laser head velocity (tests: 9 to 11).

Table 2.2 : The parameters of Laser Nd:YAG

Test group	No of test	Energy per pulse (Joule/pulse)	Pulse width (ms)	Frequency	Laser power peak (kW)	Average power of pulsed laser (Watts)	The velocity of the Laser head (mm/s)
Fix laser head with maximum exposure time of 10 seconds	1	3.2	2	10	1.6	32	0
	2	10.14	8	10	1.2675	101.4	0
	3	20.5	15	10	1.3666	205	0
	4	20.1	15	10	1.34	201	0
constant laser head velocity with different power levels	5	20.1	15	10	1.34	201	0.4
	6	20.1	15	12	1.34	241.2	0.4
	7	15	2	12	7.5	180	0.4
	8	17.99	2.5	12	7.196	215.88	0.4
Constant laser power with increasing velocity	9	17.99	2.5	12	7.196	215.88	1.73
	10	17.99	2.5	12	7.196	215.88	7.7
	11	17.99	2.5	12	7.196	215.88	16.66

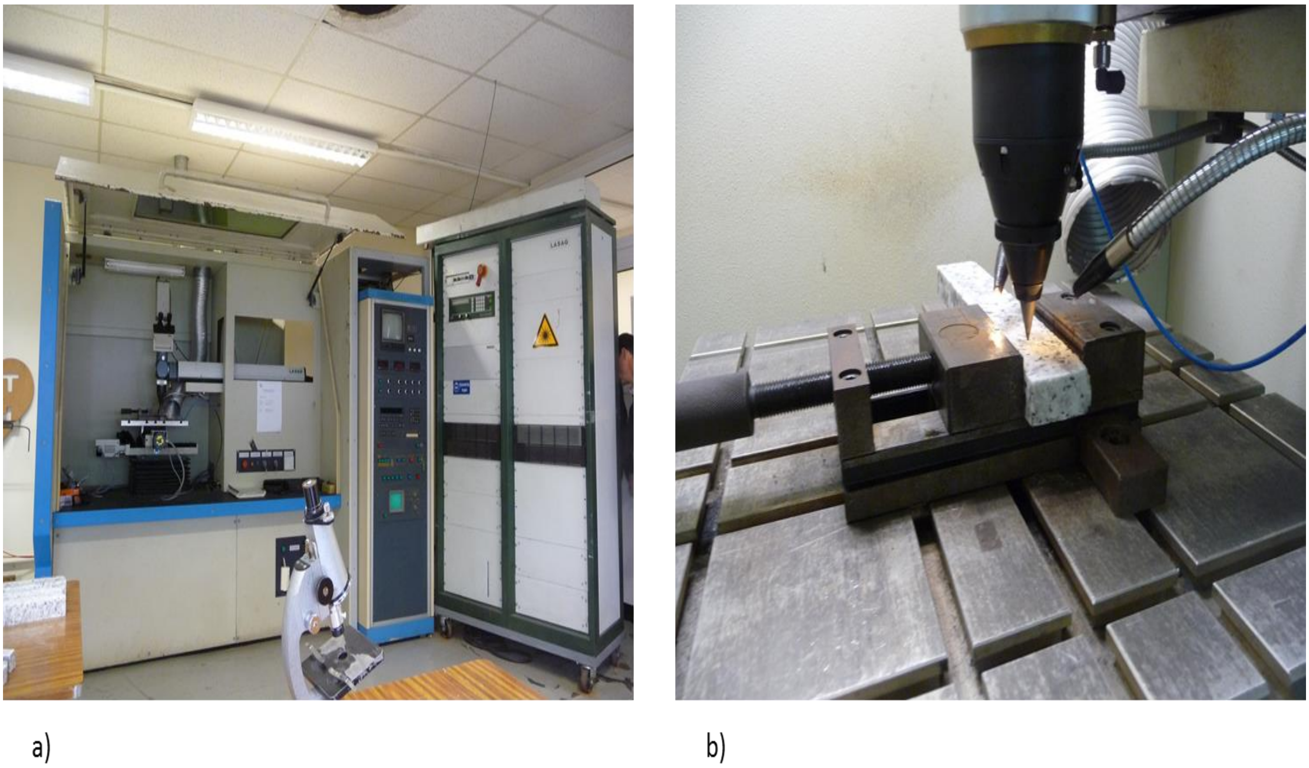

Figure 2.1: a) The Experimental setup used in the test, b) The arrangement of the sample under the laser nozzle

2.3 Laboratory results

2.3.1 Group 1

This group includes 4 tests, which were conducted with fix laser head and different laser power parameters. Figure 2.2 shows the results of the first three tests. It can be observed that the laser treatment has insignificant effect on the rock surface. The traces of the laser can't be easily distinguished on the rock surfaced. Burnt area was slightly identified at the borders of the treated spots. The penetration in tests (1, 2) can be considered as 0 mm where neither the power characteristics nor the exposure time allowed the laser to leave more deep effect. In test 3 the effect was more pronounced than in tests 1 and 2 but the penetration depth was lower than 0.5 mm.

In the fourth test, the effect of the laser treatment was deeper that observed with tests 1,2 and 3. The penetration treatment was between 1 and 2 mm. However, the rock material was efficiently removed but with the molten zone (Figure 2.3). In this test the laser was applied on the border of the sample. After the sample cooling, the material had been removed by hand pressure around the molten zone.

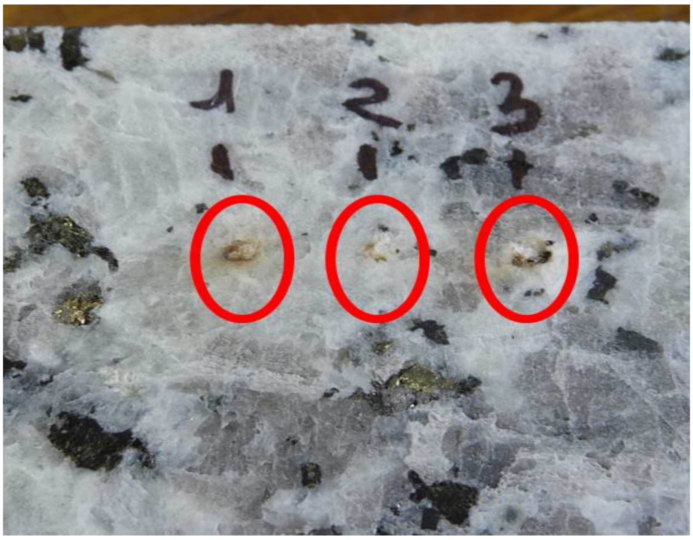

Figure 2.2: Results of the tests:
Test 1: power peak 1.6 kW, average power 32 watts, nozzle velocity 0.0 mm/s
Test 2: power peak 1.2675 kW, average power 101.4 watts, nozzle velocity 0.0 mm/s
Test 3: power peak 1.366 kW, average power 205 watts, nozzle velocity 0.0 mm/s

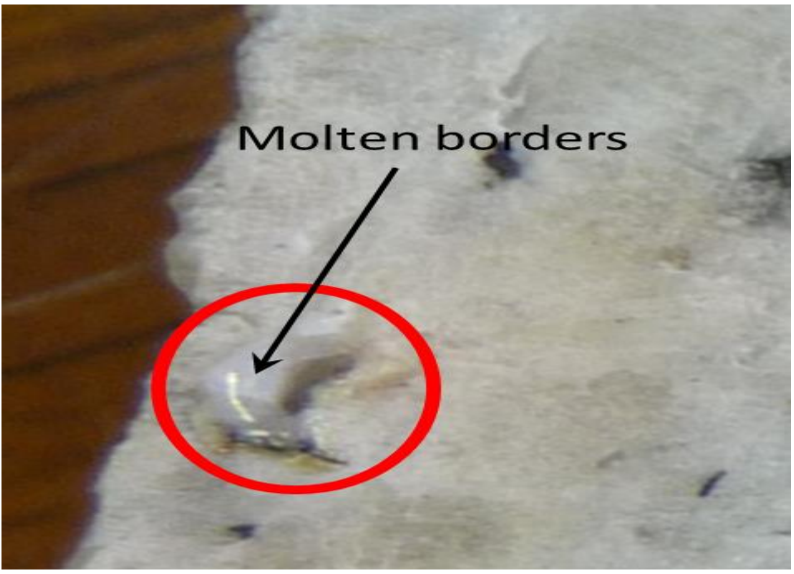

Figure 2.3: The molten border due to laser treatment in test (4): power peak 1.34 kW, average power 201 watts, nozzle velocity 0.0 mm/s

2.3.2 Group 2

This group includes 4 tests (5 to 8), which were conducted with moving laser head at a constant speed (0.4 mm/s). In these tests, we observed a significant influence of the laser treatment. Tests 5 and 6 were conducted with 20.1 Joule/pulse and a laser power peak 1.34 kW. The frequency was equal to 10 and 12 Hz, respectively. The penetration depth varied along the treatment. Some zones appeared intact because of the large pulse width. The penetration depth varied according to the grain type along the treatment line. The penetration was deeper in mica grains than in quartz grains. The material was mostly removed by melting mechanism where glassy phase formed on the surface of the rock due to the quartz grains melting. We observed that the zone with removed material was re-filled by the recrystallization of the molten material.

Figure 2.4 shows the result of test 6. We observe that the influence of the laser treatment exceeded the trajectory of the laser beam. An area 3 to 4 mm in width can be identified by the naked eye over both sides of the laser line passage. The penetration depth varied between 0 to 4 mm.

Tests 7 and 8 used higher power laser peak than tests 5 and 6 (7.5 kW) with 15 and 18 joule per pulse, respectively. Figure 2.5 shows the results of these tests. The rock material was strongly molten, but without any material removal by spallation. The material was mostly excluded by melting. The color changed over the treated zone. It varied between yellow and dark red. The color change could be attributed to the transition phase in the quartz (α to β) or to the burn of the organic impurities in the rock structure.

The molten material apparently belongs to the mica grains. We observed that the molten material refilled the space of the remove material. In some zones, the molten material recrystallized into to more resistant material than the original. By the end of the test we observed that the rock material was largely damaged in the zone adjacent zones to laser trajectory (Figure 2.6). We also observed a in the area adjacent to the laser trajectory, a high density of cracks parallel to the laser trajectory. These cracks propagated largely in depth under the laser beam path. Since the thermal stress and the melting energy for fusion are proportional to the temperature (Xu et al., 2003), the fracture in the adjacent area was due to the restriction of the high temperature within this area.

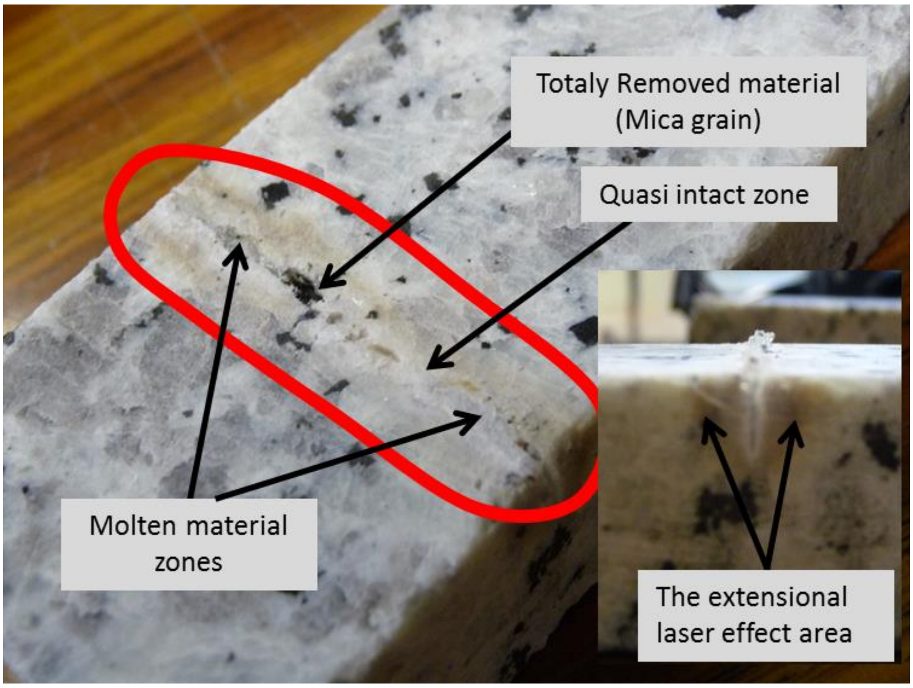

Figure 2.4: The Laser trace and the identified zones in test (6) power peak 1.34 kW, average power 241.2 watts, nozzle velocity 0.4 mm/s

Figure 2.5: Cracks in tests:
Test 7 right: power peak 7.5 kW, average power 180 watts, nozzle velocity 0.4 mm/s
Test 8 left: power peak 7.196 kW, average power 215.88 watts, nozzle velocity 0.4 mm/s

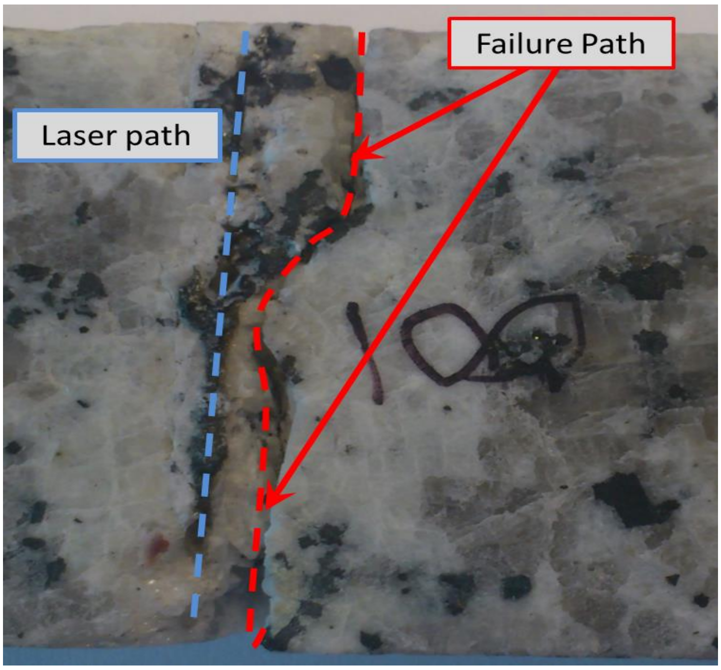

Figure 2.6: Damage induced in the area adjacent to the laser trajectory (test 8)

2.3.3 Group 3

This group includes 3 tests (9, 10, 11) which were conducted with three velocities of the laser beam (1.73, 7.7 and 16.6 mm/s). Figure 2.7 shows the impact of these tests on the rock samples. It is evident that the velocity of the laser nozzle influenced largely the laser removal performance. The increase in the velocity of the laser nozzle leaded to a gradual transformation of the impact of the laser treatment from continuous linear to continuous punctual. This change could be attributed to the non-correspondence between the relaxation time of the laser and the velocity of the laser head.

Xu et al. (2004) perforated a rock sample with rotational velocity of 60°/s (i.e. 8 m/s) using Nd:YAG laser with an average power of 1600 watts. The maximum velocity 16.66 mm/s was realized with an average laser power of laser 216 watts, which is smaller than 1600 watts. From other hand, Xu et al. (2004) reported that the melting take place beyond 600 Watts but in our study we found that the material removed by melting with lower energy level. In order to get similar linear continuous effect as in test 9 with laser head velocity as in the test (11) (16.66 mm/s), the frequency of the pulsed laser should be increased to 115 Hz and the average power per pulsed laser should also be increased to 2068 Watts.

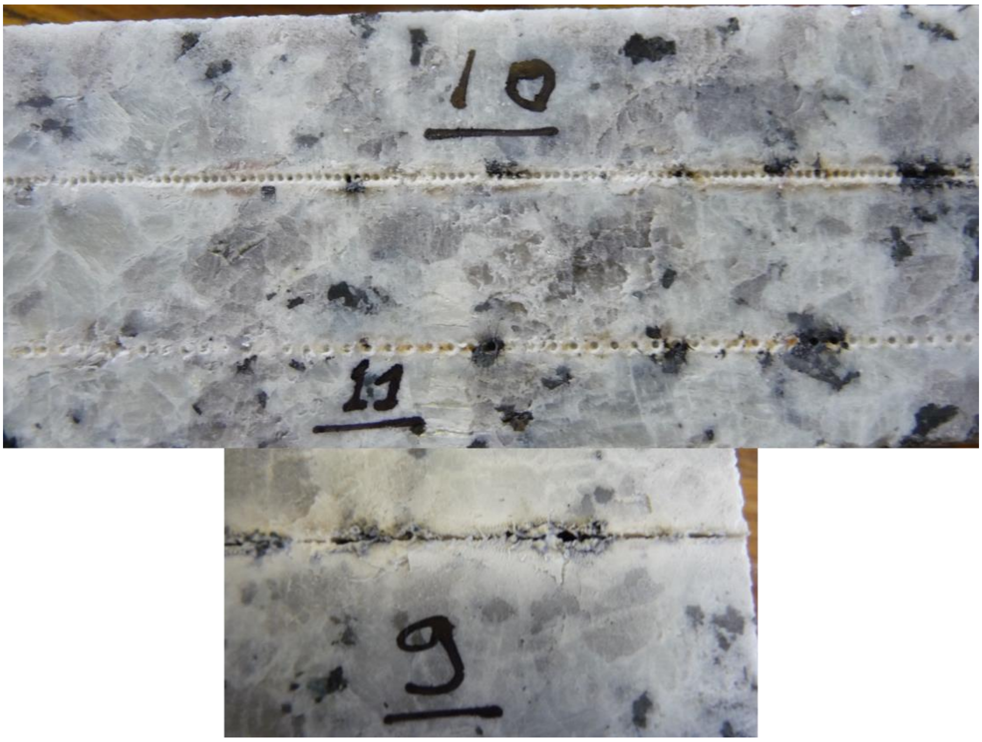

Figure 2.7: Results of tests:
Test 9: power peak 7.196 kW, average power 215.88 watts, nozzle velocity 1.73 mm/s
Test 10: power peak 7.196 kW, average power 215.88 watts, nozzle velocity 7.7 mm/s
Test 11: power peak 7.196 kW, average power 215.88 watts, nozzle velocity 16.66 mm/s

2.4 Conclusion

This chapter included a laboratory investigation of the laser-rock material interaction in order to explore the possibility of the use of the laser for rock fracture. The results of the experiments can be summarized as follows:

- The use of the laser could lead to rock material removal, but generally by melting process.
- The recrystallization of the molten rock material refills the space created by the laser treatment; consequently the removal of the rock material becomes more difficult.
- The use of the laser causes thermal damage in an area adjacent to the radiated zone.
- The velocity of the laser nozzle largely influences the rock removing process by laser. With the increase in this velocity, the trace of the laser becomes discontinuous in form of dotted line.

CHAPTER 3

USE OF THE HEATING/COOLING PROCESS IN ROCK FRACTURE: NUMERICAL ANALYSIS

3.1 Introduction:

The use of the heating/cooling process for rock fractures induces additional benefits in the process of rock fractures regarding the use of only the heating process. For instance, the heating and cooling thermal cycle will induce a cycle of compression/extension stresses, which will accelerate the rock material fracture and alteration.

Ross (1964) has invented an excavating apparatus based on this idea. This apparatus combined: high pressure, high temperature and superheated steam. He reported that this technique could penetrate the hardest granite with ten to twenty feet per hour as rate of penetration. The technique consists of three minutes of heating the rock surface and then the liquid nitrogen at 321 °F (-200 °C) strikes the preheated rock surface. Likewise the rock undergoes a thermal shock in a fraction of a second. The attained stresses were reported to be of order of one million pounds per square inch (~6900 MPa).

In this chapter we propose to analyze a similar method, which uses **microwave radiation** for heating and the **water** for cooling. This chapter includes presentation of the proposed method, followed by the numerical model used for the analysis of this method and finally analysis of the major parameters influence the method efficiency.

3.2 Description of the heating/cooling method

The process consists of two stages. The first stage concerns heating; the treated zone will be heated to temperature lower than that of the transition brittle-quasi brittle. The heat flux shouldn't be intensive, in order to allow the temperature penetration and the expansion of the rock material in the heated area relatively to the surrounding non-heated zone.

The second stage concerns the rock cooling using water. The heating power has been cut off and immediately the cooling stage starts before that treated zone relaxes and loses the restrained heat. The use of water in cooling leads to a sharp decrease in the temperature and to the creation of temperature gradient and the inversion of stresses from compression to extension. The treated zone strongly contracts and experience tensile stresses.

During the heating phase, the increase in the temperature reduces the tensile strength of the rock (Hommand-Etienne and Hourpert, 1989), which has a positive effect on the rock fracture in the treated zone. The coolant type and the temperature play major roles in stresses conversion process. The heat convection coefficient of coolant will describe the rate of the cooling process. The coolant temperature largely affects the energy dissipation and consequently the magnitude of the tensile stresses. The stresses penetration beneath treated surface is affected by both the coolant fluid and its temperature.

At the end of the cooling stage, the treated zone is expected to be spalled out by tension failure. The cyclic nature of the process has a major role in achieving an important penetration depth. Figure 3.1 presents a schematic illustration of the fracture process, which will be analyzed in the following subsections.

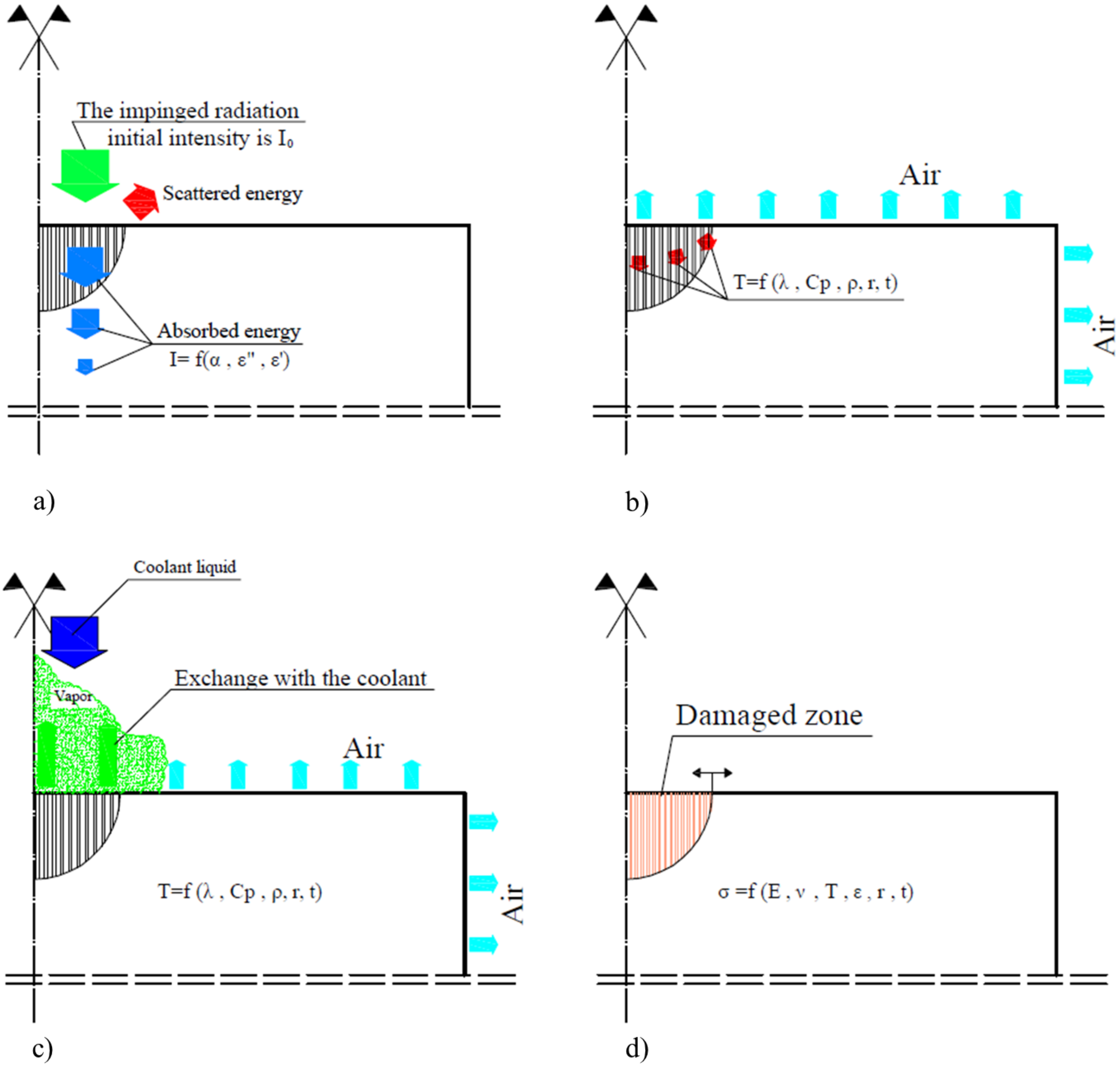

Figure 3.1: Illustration scheme of the whole process, a) heating by microwaves, b) heat transfer during heating phase, c) heat transfer during cooling phase, d) the expected damaged zone.

3.3 Numerical modeling of the heating/cooling fracture process

3.3.1 Presentation of the numerical model

Analysis of the heating/cooling fracture process includes the following physical modeling (Figure 3.2):

- The interaction between the electromagnetic waves and the rock medium.

- The heat transfer within the rock material during the heating phase as well as the cooling phase.
- The mechanical response of the rock to the heating/cooling process.

The interaction between the rock material and the electromagnetic waves requires the consideration of the wave transmission through the rock media, the wave absorption, the waves reflection at the rock surface and waves attenuation.

The heat transfer in the rock media is complex. Because the rock material is a porous medium composed of grains, pores filled by gas and water, which affect the heat transfer. In this work, the rock material is considered as a homogeneous continuous media. The cooling phase consists in the heat exchange between the rock and the coolant where the heat convection is predominant. Depending on the type of coolant, other events; are expected to occur, such as boiling and evaporation. The rate of cooling largely affects the change of compressive stresses into tensile ones.

The mechanical behavior of the rock material will be described through thermo-elastic model, where the material will be considered as elastic, isotropic and homogeneous one. The evolution of stresses due to the thermal dilatation (during heating) and contraction (during cooling) will be studied. The variation of the stresses due to different stages of the thermal process will be discussed as well the penetration depth.

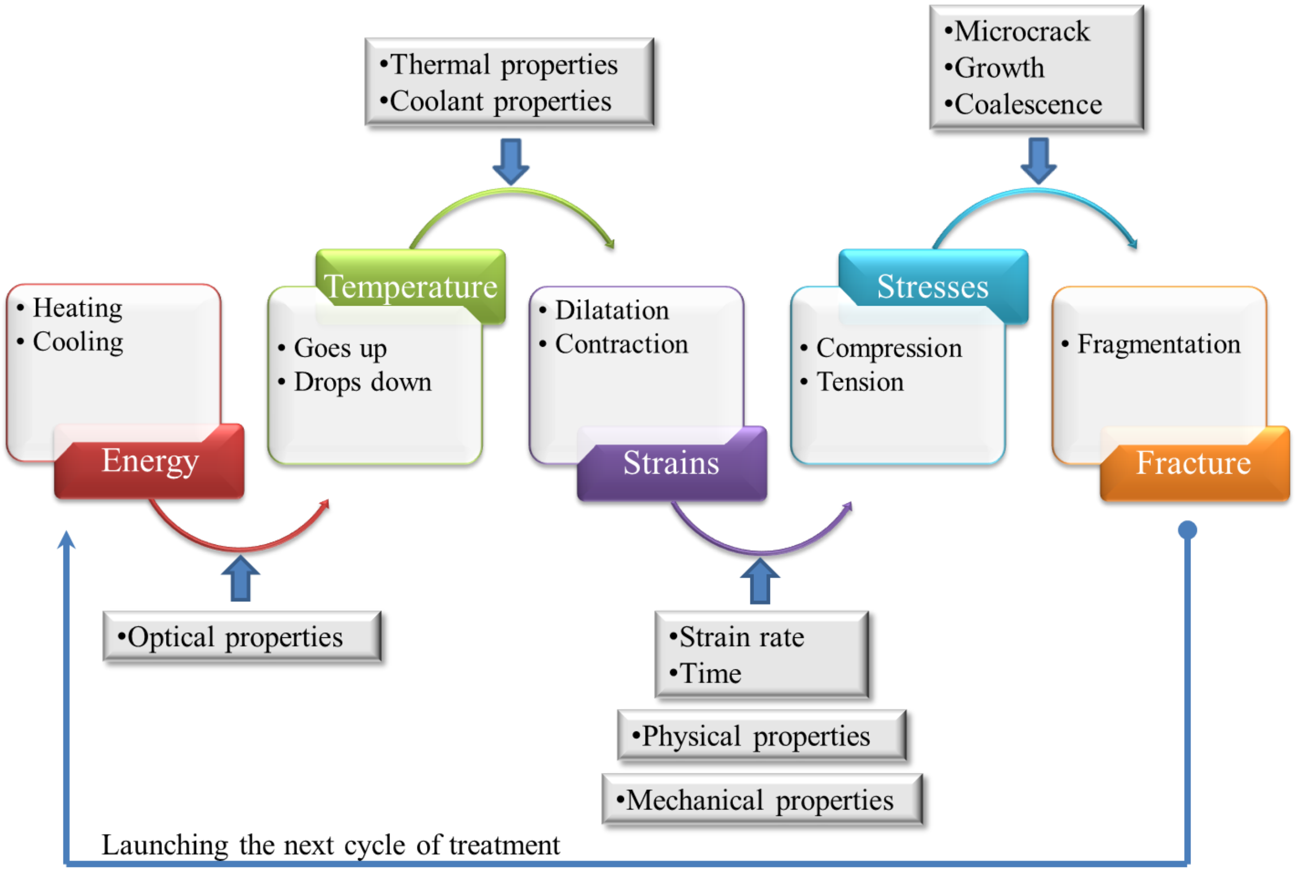

Figure 3.2: The physical events during one cycle of examined thermal treatment

3.3.2 The microwaves-rock material interaction

Micro-waves could be used as a radiation source in crushing rocks or concrete demolishing (Jerby and Dikhtyar, 2001). Electromagnetic waves are created by the vibration of an electric charge. This vibration creates a wave, which has both an electric and a magnetic component. The interaction between the rock material and the electromagnetic wave includes wave reflection, transmission and absorption. The absorptivity designates the ratio between the absorbed energy and the incident energy. The Absorptivity changes during the heating process and is a function of the rock's properties as well as the properties of the electromagnetic wave.

The wave-material modeling should take into consideration the following:

- **Electromagnetic waves**: intensity, wavelength (λ), angle of Incidence (α), polarization p (parallel or perpendicular to the plane of incidence).

- **Material:** Composition (e.g. pure metals, alloys, polymers, ceramics, composites, etc.), Temperature (T), Surface roughness, Surface and bulk defects and impurities (e.g. dust particles, abrasives, cracks, pores, oxides, etc.)

Electromagnetic waves propagation through the rock material is described by Maxwell's equations. A solution to the wave equation for the electric field $E_{(z,\ t)}$ in the case of a plane wave propagating along the z-axis can be written (Hewson, 1970):

$$E_{(z,t)} = E_0 . e^{-(\frac{w}{c})kz} . e^{i\left(\frac{w}{c}\right)nz} . e^{-iwt} \qquad \textit{Eq 3-1}$$

Where E_0 is the amplitude of the field strength, (n) the index of refraction, (k) the extinction coefficient, (w) the angular frequency of the wave and c is the light velocity in the medium. The first exponential on the right hand side describes an attenuation (damping) of the wave, whereas the last two represent the characteristics of free propagation. As the intensity of an electromagnetic wave is proportional to the square of the amplitude of electric field, the intensity will decrease over distance when the wave is passing through an absorbing medium.

The optical constants (n) and (k) can be calculated from the complex dielectric permittivity:

$$\epsilon = \epsilon_1 - i\epsilon_2 \qquad \textit{Eq 3-2}$$

$$n^2 = \frac{\epsilon_1 + \sqrt{\epsilon_1^2 + \epsilon_2^2}}{2} \qquad \textit{Eq 3-3}$$

$$k^2 = \frac{-\epsilon_1 + \sqrt{\epsilon_1^2 + \epsilon_2^2}}{2} \qquad \textit{Eq 3-4}$$

The power density absorbed by the rock material is related to the electric field (Wu, 2002):

$$p_{dis} = w\epsilon_2 \left|E_{(z,t)}\right|^2 \qquad \textit{Eq 3-5}$$

The dissipated energy is equivalent to the absorbed energy by the material. The Lambert's expression governs the absorbed energy (Zhou et al., 1995):

$$\mathrm{I}_{(z)} = I_0 \mathrm{e}^{-2\alpha.z} = I_0 . e^{-\frac{z}{D_p}}$$

Eq 3-6

Where I_0 is the incident power density, and z is the power penetration depth beneath the irradiated surface, and the D_p the depth at which the power drops to (1/e) from its original value, $D_p = 1/2\alpha$. The Attenuation coefficient is expressed as a function of the dielectric properties and the wave length:

$$\alpha = \frac{2.\pi}{\lambda} . \sqrt{\frac{\varepsilon' . \left[\left(1 + tg^2(\delta)\right)^{\frac{1}{2}} - 1\right]}{2}}$$

Eq 3-7

$$tg(\delta) = \frac{\varepsilon''}{\varepsilon'} \qquad \left\{ \begin{matrix} \lambda \; wave\ length \\ \varepsilon'' \quad loss\ dielectric\ factor \\ \varepsilon' \quad dielectric\ constant \end{matrix} \right\}$$

Eq 3-8

The material’s absorptivity A is expressed as:

$$A = log\left[\frac{I_0}{I_{(z)}}\right] = \log(e^{\alpha z}) = \alpha . z . \log(e)$$

Eq 3-9

3.3.3 Heat transfer in the rock material

The heat transfer in the rock material is governed by the general equation of heat transfer:

$$\rho . c . \frac{\partial T}{\partial t} = \nabla . (\mathrm{k} \nabla T) + \mathrm{Q}$$

Eq 3-10

Where :

- T(x,y,z,t) : Temperature (°K)

- ρ : Density of the rock (kg/m^3)
- C : Specific heat of the rock (J/kg.K)
- k : Thermal conductivity of the rock (W/m.K)
- t : Time (sec)
- Q : Volumetric heat generation (W/m^3) expressed in the equation *(Eq 3-5)*.

The heat exchange with the surrounding environment is governed by the expression:

$$q = -h_C.\left(T_s - T_{inf}\right) \qquad \textit{Eq 3-11}$$

T_s denotes the temperature t the rock surface, T_{inf} is the temperature of the external fluid and h_C is the coefficient of the heat exchange between the coolant and the rock surface.

The thermal process is composed of two stages. In the first one, the rock surface is heated up to a desired temperature. According to the power density, rock composition and exterior temperature, the treated rock surface will reach the desired maximal temperature after certain time. During this stage the heat exchange with the surrounding environment occurs with the air at ambient temperature. The temperature is restrained in a small zone beneath the treated spot, because of the low thermal conductivity and diffusivity of the rock material.

The second stage concerns the cooling process using water as coolant. The temperature decreases at a certain rate, which depends on the difference between the rock temperature and the coolant temperature as well as the rate of energy dissipation from the rock material. The dissipation process is directly related to the exchange heat coefficient between the rock surface and the coolant as well as the nature of the coolant.

Figure 3.3 presents a scheme of the temperature variation during the heating/cooling process.

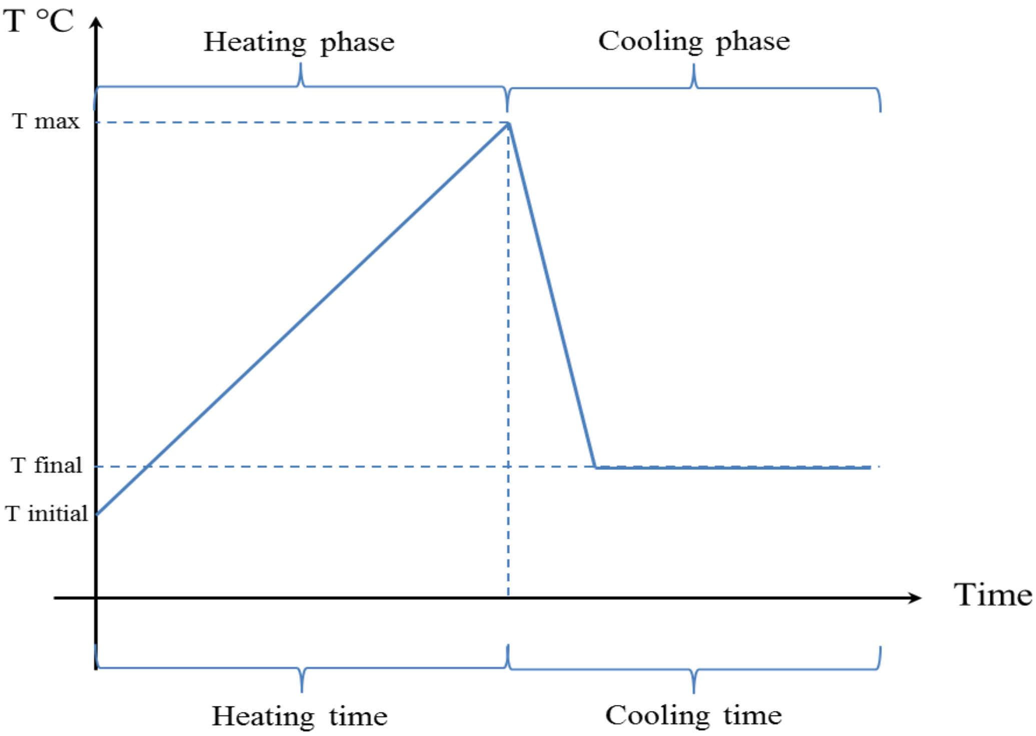

Figure 3.3: Temperature expected profile on the treated rock surface

The efficiency of the heating/cooling process depends mainly on the heat exchange coefficient and the temperature of the coolant. In the following section we give a description of the influence of these two factors.

Coefficient of the heat exchange h_C

At the end of the heating phase, the temperature of the rock surface is largely higher than that of the coolant liquid (water). The heat transfer occurs by boiling (Karwa, 2012). This process is called the "quenching process" in the metallurgy industry. The heat transfer in boiling occurs by phase change process, which results in rapid vapor bubble formation, their growth and departure from the surface. Four distinguished heat transfer regimes can be observed during boiling at the heated surface (Figure 3.4): film boiling, transition boiling, nucleate boiling and single-phase natural convection.

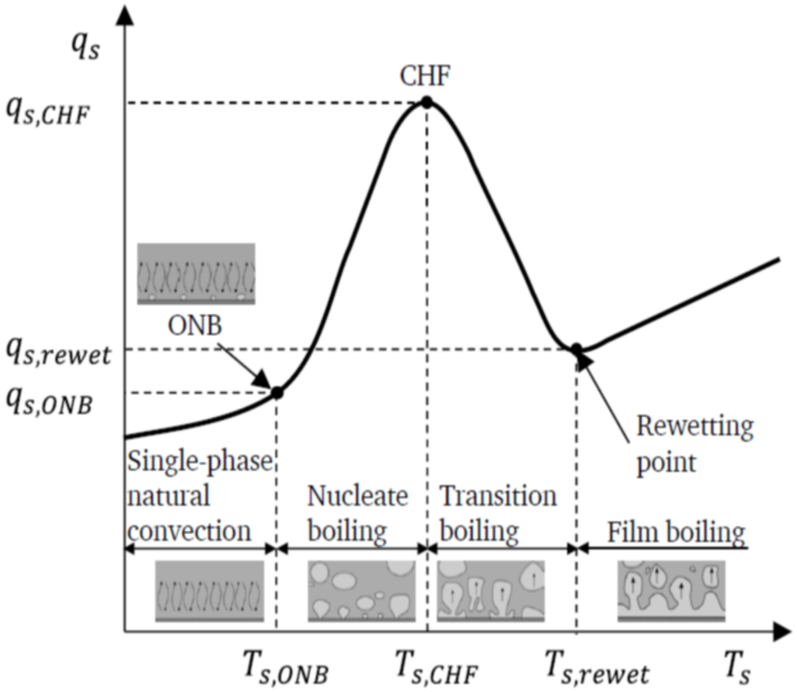

Figure 3.4: Nukiyama's curve presented by (Karwa, 2012)

Film boiling occurs when the surface temperature $T_s \geq T_{s,rewet}$. It is characterized by a stable layer of vapor, which is formed between the heated surface and the liquid. Vapor is generated at the liquid-vapor interface and then escapes into the liquid above. The end of this regime is referred to the Leidenfrost point [4] or the minimum heat flux point or the rewetting point. The heat flux and the surface temperature at this point are referred to the rewetting heat flux, $q_{s,rewet}$, and the surface rewetting temperature, $T_{s,rewet}$, respectively.

Transition boiling is an unstable intermediate regime between nucleate boiling and film boiling. It occurs when the surface temperature ranges between $T_{s,CHF}$ and $T_{s,rewet}$. The boiling mode fluctuates between nucleate boiling and film boiling. At the end of this regime, the heat flux reaches its maximum value.

Nucleate boiling is a two-phase natural convection process. During this phase, the bubbles nucleate, grow and leave the heated surface. The end of this zone is marked by the onset of nucleate boiling called (ONB) point.

Single-phase natural convection occurs at low surface temperature. At this temperature, the vapor bubble immediately condenses in sub-cooled liquid t. The main mode of heat transfer here is the natural convection.

The boiling film reduces the contact between the liquid and the solid (Karwa et al., 2011). Consequently low cooling rates will be obtained because of continuous insulation between the liquid and rock surface. Through the transition-boiling regime, the absorbed heat flux decreases below the critical heat flux, because of a thin layer of low thermal conductivity of vapor (Karwa et al., 2011). Figure 3.5 describes the different regimes of heat transfer during the cooling process.

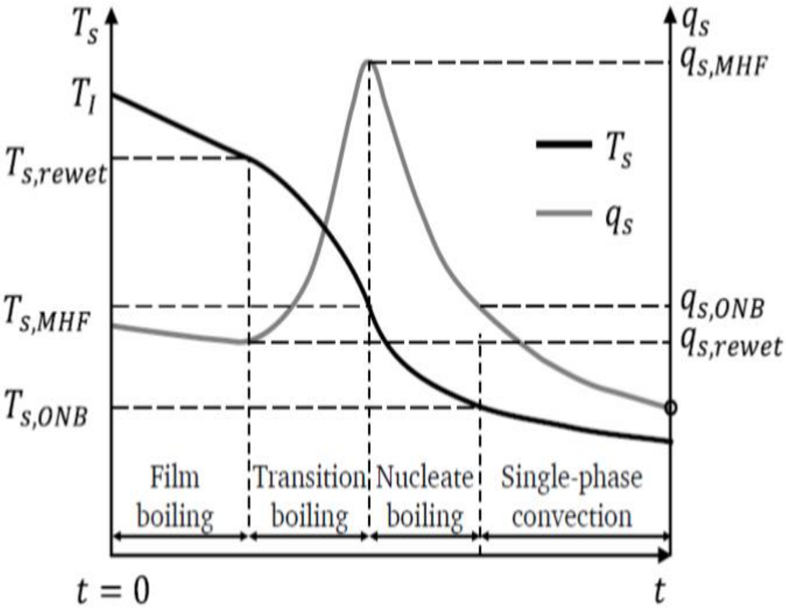

Figure 3.5: Cooling profile over the time (Karwa, 2012)

The efficiency of the proposed thermal process largely depends on the efficiency of the cooling stage, which consists in the increase in the rate of heat exchange. Consequently, the nucleate boiling is privileged in the process. Due to the imperfection of the rock surface, the bubbles begin to rise due to buoyancy forces and may merge with other isolated bubbles to form jets or columns. Because the detaching bubbles are quickly replaced by liquid, the effective thermal conductivity of the fluid layer close to surface is high (Comsol, 2011).

Faghri et al. (2006) indicated that the heat transfer mechanisms in the nucleate boiling include:

- Transient heat conduction from the heating surface to the adjacent liquid.
- Natural convection on inactive areas of the heating surface.
- Evaporation from the micro layer underneath the vapor bubble.

Consequently the heat flux during the nucleate boiling is the sum of three corresponding heat flux of the previous mechanism:

$$q_{total} = q_{conduction} + q_{convection} + q_{evaporation} \qquad \text{Eq 3-12}$$

After the calculation of this heat flux the heat exchange coefficient can be calculated according to (Faghri and Zhang, 2006):

$$q_{total} = h_c(T_s - T_{sat}) \qquad \text{Eq 3-13}$$

T_s is the surface temperature, T_{sat} the water saturation temperature (100 °C). Figure 3.6 illustrates the dependency of the heat exchange coefficient on the heat flux. Two zones can be distinguished: the first concerns the evaporation process (a) while the second corresponds to boiling (b) (Karwa, 2012).

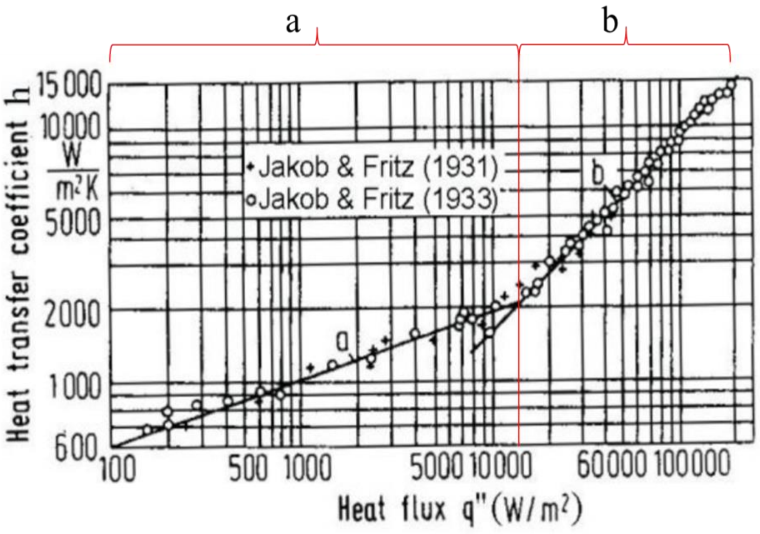

Figure 3.6: Heat transfer coefficient variation with the heat flux

The issue of cooling by water has been mainly addressed using experimental research, because the numerical modeling of the nucleate boiling is complex. In this work we use a simplified model based on the equivalent heat transfer coefficient for the cooling phase. Gorenflo (1993), cited by (Faghri and Zhang, 2006), suggested the following expression for the heat exchange coefficient:

$$h_C = h_0 . F_{PF} . \left(\frac{q^"}{q_0^"}\right)^{nf} . (\frac{R_p}{R_{p0}})^{0.133} \quad , \quad 0.0005 < p_r < 0.95 \qquad \textit{Eq 3-14}$$

- h_0: is the reference heat transfer coefficient at fixed reference conditions.
- $\frac{p}{p_r}$ is the reduced pressure
- $p_{r0} = 0.1, \ R_{p0} = 0.4\,\mu m, q_0^" = 2 * 10^4\ W/m^2$
- The pressure correction factor is:

$$F_{PF} = 1.73 p_r^{0.27} + [6.1 + \frac{0.68}{1-p_r}] p_r^2 \qquad \text{for the water}$$

- The exponent:

$$nf = 0.9 - 0.3 p_r^{0.3} \qquad \text{for the water}$$

- The surface roughness R_p is in μm and it takes the value 0.4 for unknown surface roughness this factor is expected to have a crucial influence on the cooling process.
- $q"$ is the heat flux (W/m^2).

The maximum temperature of the rock surface and the coolant temperature

Both the maximum temperature of the surface and the coolant temperature largely control the dissipation of the heat energy. When the water touches the heated surface, it heats up till the saturation point. At this point, it begins to evaporate. Both the temperature and nature of the coolant vary during this process. Figure 3.7 shows the water temperature variation with the heat energy during the different phases.

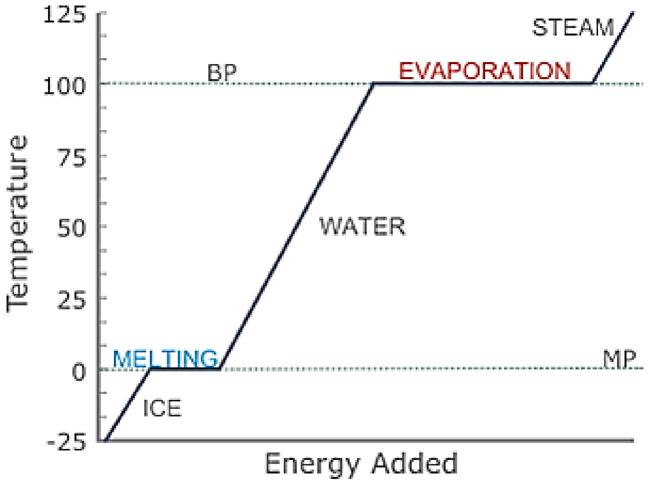

Figure 3.7: Water temperature variation with heat energy and the corresponding phases

3.3.4 Thermo-mechanical behavior of the rock material

During the heating process, the treated zone locally expands and creates compressive stresses within the treated zone. The compressive stresses could exceed the crack initiation limit. For the granite, this limit is around 30%~39% of the compressive strength (Vasconcelos and Lourenço, 2008) (Eberhardt, 1998). The pre-existed micro-cracks within the rock material extends in parallel to the treated surface according to the compressive stresses direction (Preston and White, 1934) (Rauenzahn, 1986) (Eberhardt, 1998) (Figure 3.8).

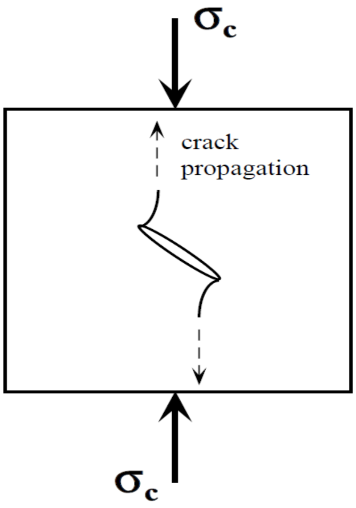

Figure 3.8: Crack propagation during compression

During the cooling process, the treated zone dramatically shrinks because of the high-energy dissipation rate. Shrinkage creates tensile stresses within the treated zone. The previously initiated micro-cracks in the heating phase become concentration points of the tensile stresses. These micro-cracks propagate perpendicularly to the tensile stresses direction (Eberhardt, 1998) (Figure 3.9). When the tensile stresses exceed the tensile strength of the rock, the fracture is created in the rock.

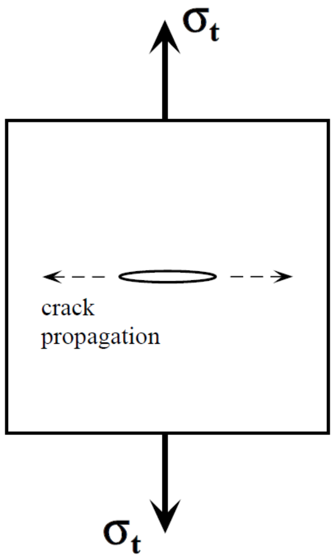

Figure 3.9: Crack propagation during tension

The heating phase induces a reduction of the tensional strength of the rock material, which could attain 33% (Hommand-Etienne and Hourpert, 1989). This reduction facilitates the rock fracture. Figure 3.10 presents a schematic illustration of the rock removal procedure due to the presence of inherent crack within the rock material.

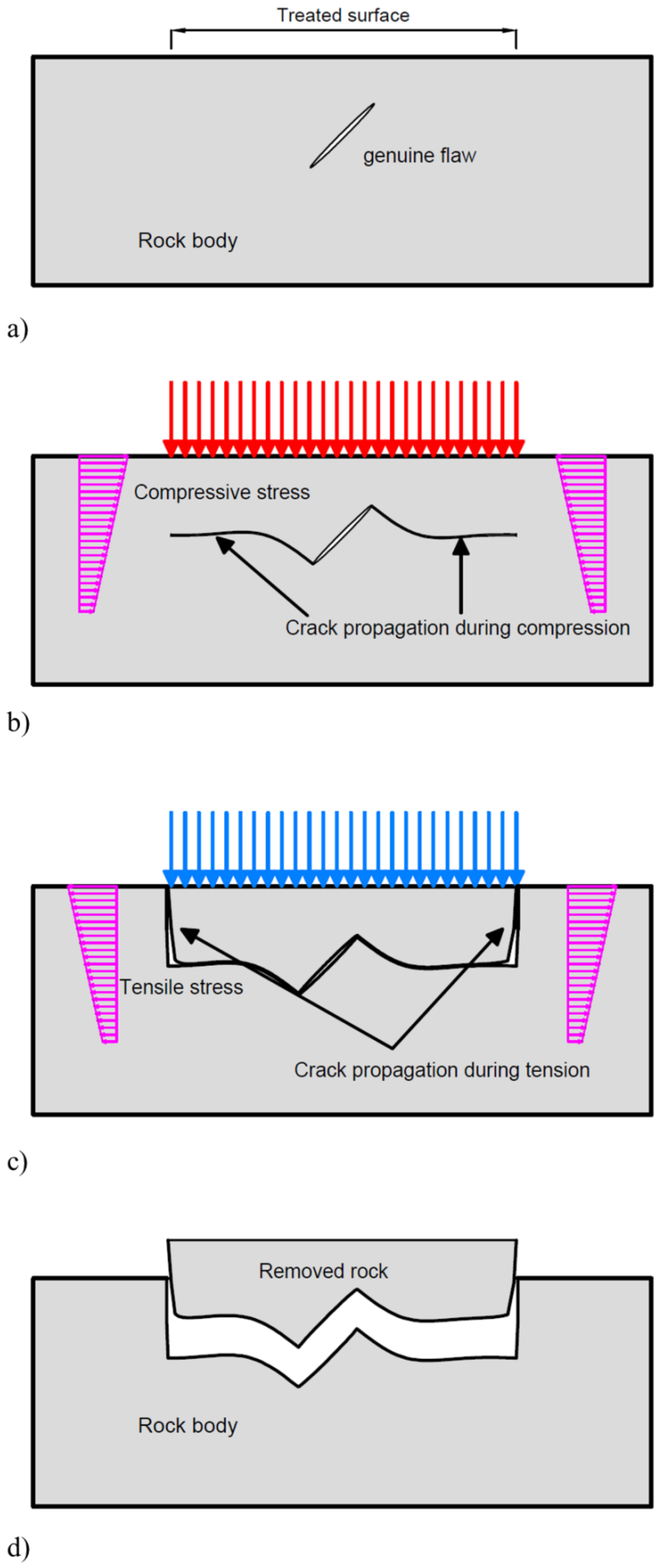

Figure 3.10: Schematic illustration of the removing rock process, a) Intact rock, b) Crack propagation due to compressive stresses in parallel to the treated surface during heating phase, c) Crack propagation due to tensile stresses during cooling phase and d)The removed part of the rock body

At the mesoscopic level, the rock material is composed of different grains with different percentage. These grains differ by volume, physical and thermal properties as well as the mechanical ones. This heterogeneity induces a heterogeneous distribution of the stresses at the grain scale (Van de Steen et al., 2003). During the heating phase, the crystals of the rock expand differentially due to the difference in the coefficient of thermal expansion and induce inter or intra granular cracks (Walsh and Lomov, 2013) (Walsh et al., 2012) (Hommand-Etienne and Hourpert, 1989). The size of the grains has a significant role in the creation and development of cracks. In large crystals the intra-crystalline are dominant, but in small grains the inter-crystalline are predominant.

During cooling phase, the crystals contract also differently according to their different volume and thermal expansion. This differential contraction induces tensile stresses at the crystals and the cementation. Failure occurs when the tensile stresses exceed the strength of the crystals or the cementation. The processes of damage initiation, accumulation and interaction are primarily tensile (Lan et al., 2010).

The size of the damaged zone is related to the penetration of the temperature beneath the treated surface as well as the rate of the energy dissipation. The penetration depth is expected depends on the cooling rate. The amplitude of the tensile stresses depends on the difference between the maximum temperature of the heated surface and the coolant temperature

However, to simplify the numerical model, the behavior of the rock material is described using an isotropic linear elastic constitutive law:

$$\sigma_{ij} = C_{ijkl.}(\varepsilon_{kl} - \alpha \Delta T \delta_{kl}) \qquad \textit{Eq 3-15}$$

C_{ijkl} is the elastic modulus tensor, α is the thermal expansion coefficient, T is the temperature, δ_{kl} is the Kronecker delta.

Both temperature and pressure influence the thermal expansion coefficient. The latter increases with the increase in the temperature (Huotari and Kukkonen, 2004) and decreases with the increase in the confining pressure (Heuze, 1983).

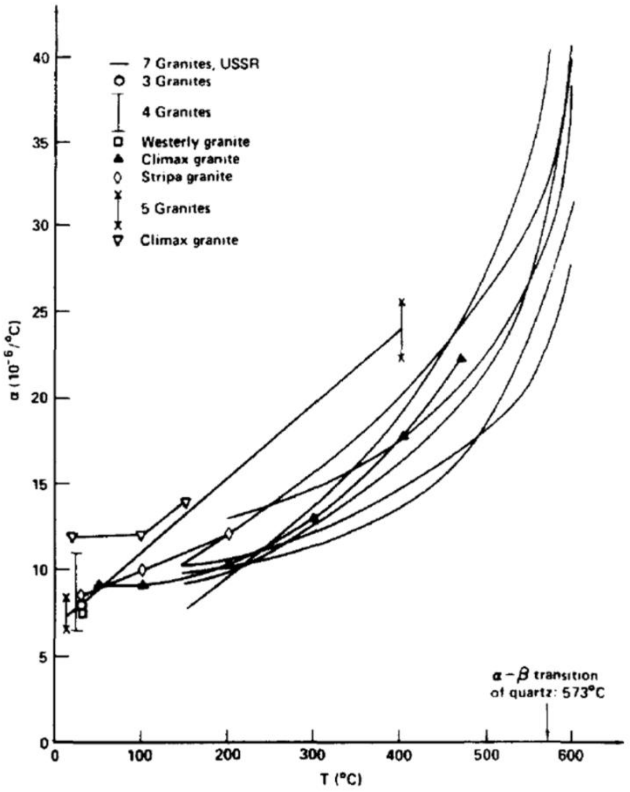

Figure 3.11 Thermal expansion coefficient variation with temperature (Heuze, 1983)

3.4 Numerical model

The heating/cooling process was analyzed using software COMSOL MULTIPHYSICS 4.2. COMSOL Multiphysics is a powerful interactive environment for modeling and solving the scientific and engineering problems. Variety of physical modules is provided in the software. It has the capacity to assembly many conventional models for one type of physics to form one multiphysics model and eventually solve the coupled physics phenomena and do so simultaneously. The variables, expressions, or numbers can be directly applied to solid and fluid domains, boundaries, edges, and points by means of powerful mathematical tool of the PDEs and ODEs modules. COMSOL Multiphysics then internally compiles the set of the equations those represent the entire model.

Figure 3.12 and Figure 3.13 show the boundary condition as well as the mesh used in the analysis. Thanks to the material and boundary condition of symmetry, a 2D axisymmetric finite element model was used. Three modules were used in the modelling: the electromagnetic waves module to model the propagation of the microwaves within the sample, the heat transfer module to model the temperature distribution in the rock material and the solid mechanics to analyze the mechanical response of the rock material. The modules were interconnected through common variables:

- The electromagnetic waves stimulation was related to heat transfer by the variable in the equation (Eq 3-5) that represents the heat source term in heat transfer equation (Eq 3-10). The treated zone was considered as the entry of the waves to the sample.
- The boundary conditions in the heat transfer model were considered through the heat exchange coefficient during each phase (heating, cooling) by the use of the equation (Eq 3-11). The non-treated sides were considered in contact with the air around the sample.
- Once the temperature distribution is obtained, it will be used by the solid mechanics to solve the mechanical problem through the use of thermal expansion coefficient. The behavior of the material was considered isotropic elastic one. The displacements at the bottom of the sample were constrained. Other sides had free displacements.

Free triangular mesh was used in the model. The mesh was extra fine under the treated surface and got coarser towards the extremities of the sample. The frequency domain solver was used to solve the electromagnetic equations. The time dependent solver was used to solve the heat transfer and mechanical problems. The time stepping was selected by the use of backward differentiation formula (BDF) that is a multistep formula based on numerical differentiation for solutions to ordinary differential equations. The solution was computed by using 2th-grade polynomial in terms of backward differences. The time interval used to store the solution was selected to be 1.0 second in the heating phase and 0.01 second in the cooling phase.

3.5 Application to granite sample

3.5.1 Presentation of the sample properties and boundary condition

The numerical model is used for the analysis of the thermal treatment of a granite simple 40 mm in diameter and 40 mm in height. The treated zone has circular shape 5 mm in radius. The porosity of the granite is about 1% so we can neglect it, even though it is expected to enhance the rock removal (Walsh and Lomov, 2013). The dielectric and loss dielectric factors of the granite are taken equal to 5.753 and 0.1, respectively (Ulaby et al., 1990). The attenuation coefficient is equal to 1.0785 (1/m). Table 3.1 summarizes the granite properties (Lockner, 1998) (Vosteen and Schellschmidt, 2003) (Seipold and Huenges, 1998) (Chaki et al., 2008). The heat convection coefficient h_c of the air that surrounds the sample is equal to 10 $W/m^2.K$. The surrounding air temperature is 25 °C. The initial temperature of the rock is 25 °C.

Table 3.1 Granite properties used in the simulation

Material properties	**Density**	**Thermal conductivity**	**Specific heat**	**Thermal expansion coeff**	**Young Modulus**	**Poisson ratio**
	Kg/m^3	W/m.K	J/kg.K	1/K	GPa	
Granite	2600	1.8	930	$7*10^{-6}$	60	0.25

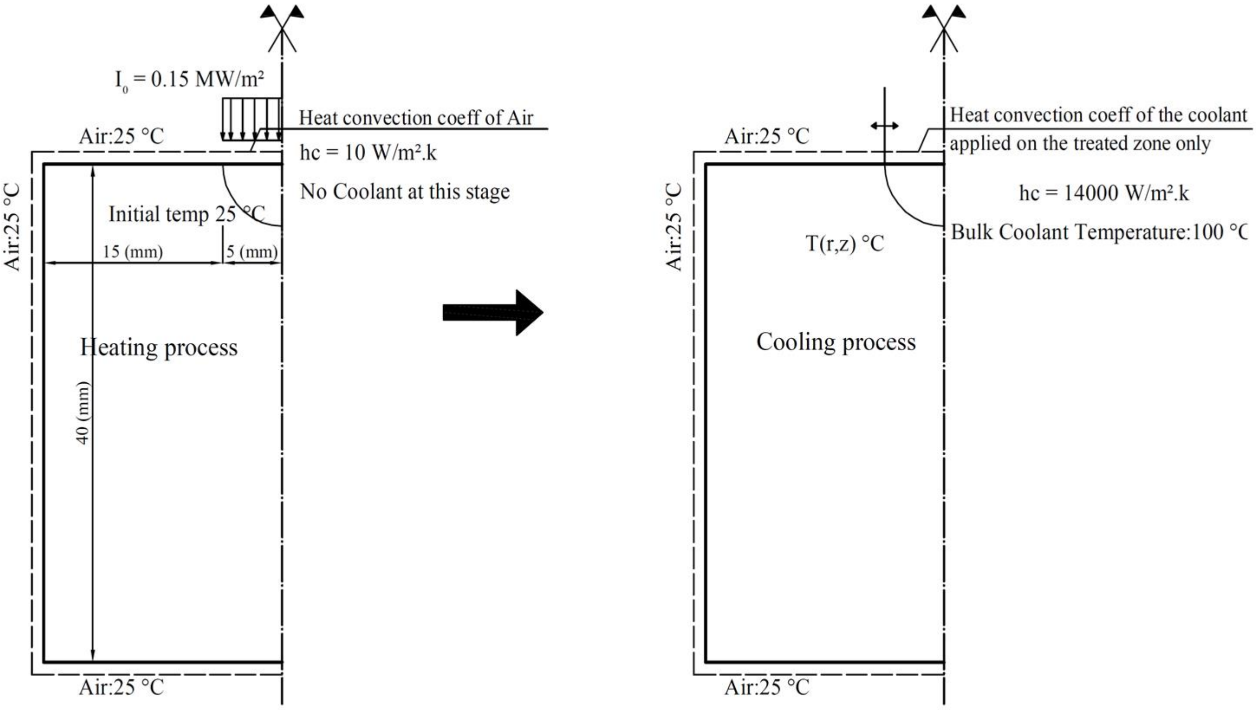

Figure 3.12 Presentation of the mode, the initial and boundary conditions

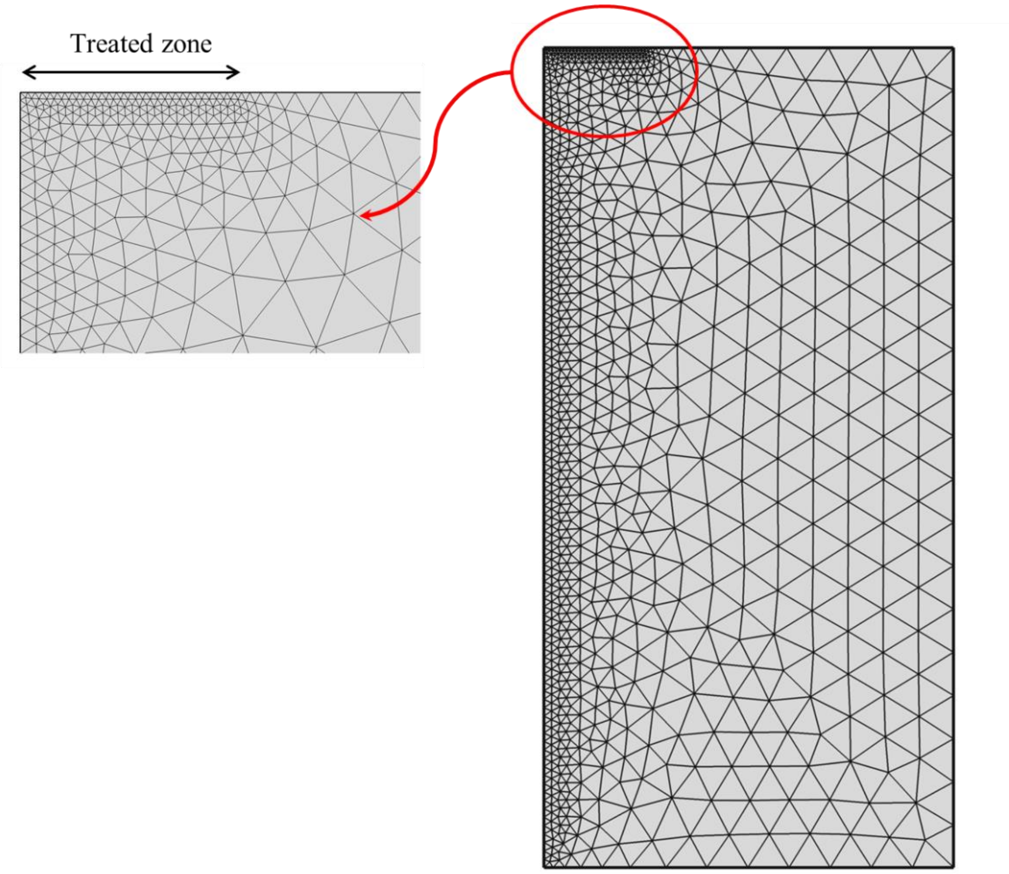

Figure 3.13 The adopted geometry and mesh

The coefficient of the heat exchange over the treated zone varies according to the phase heating or cooling (Figure 3.14). In the heating process this coefficient is equal to 10 W/m².K while during the cooling phase, it is calculated according to (Eq 3-14).

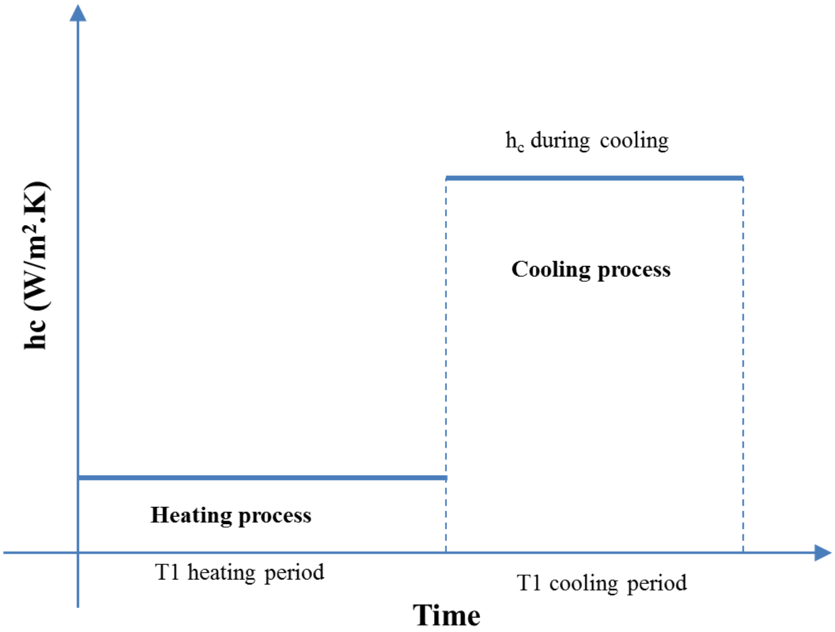

Figure 3.14 Variation of the heat exchange during the thermal treatment

3.5.2 Numerical results

Results concern both the thermal and mechanical responses.

3.5.2.1 Thermal response

Figure 3.15 shows the variation of the temperature in the treated zone. The temperature reaches 340 °C after 50 seconds of heating. During the cooling process, the temperature rapidly drops to (110 °C) after 1 second of cooling, while the temperature of the surrounding environment reaches (100 °C) after 10 seconds. This rapid drop of the temperature is strongly related to the coefficient of the heat transfer h_C.

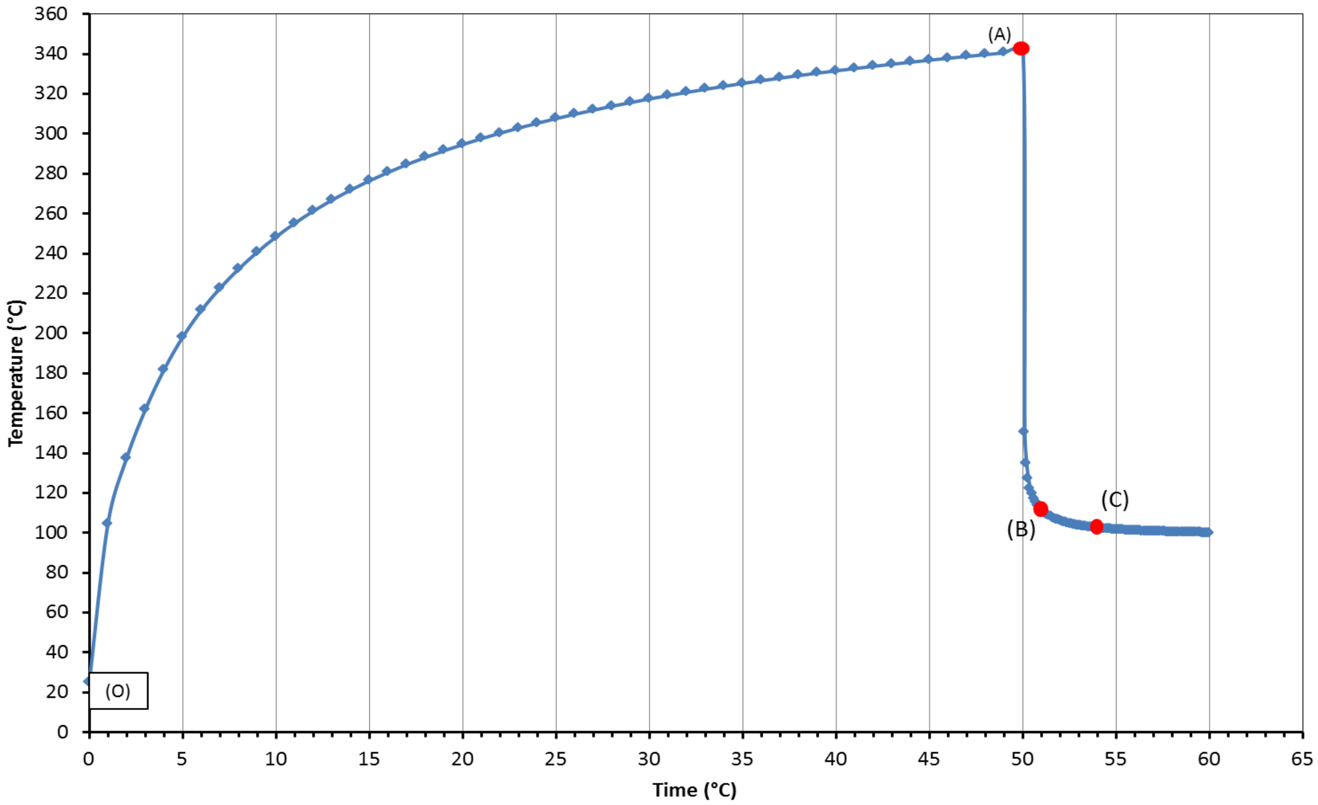

Figure 3.15 Temperature profile over the treated zone

Figure 3.16 shows the temperature variation at different times of the thermal process (t = 50, 51, 52, 53, 54 sec). We observe that the temperature is largely restrained within the treated zone. The maximum temperature is reached at the center of the sample with attenuation towards the non-treated zone. The temperature reaches 190 °C at the borders of the treated spot, and 120° C at 1 mm from the border (curve A, Figure 3.16).

During the cooling phase, the temperature at the heated spot drops rapidly to 110 °C after one second (curve B). In the non-treated zone the cooling process occurs but at lower rate than the heated spot. At the extremity of the sample, the temperature stays quasi-stable due to the weak conductivity of the rock material.

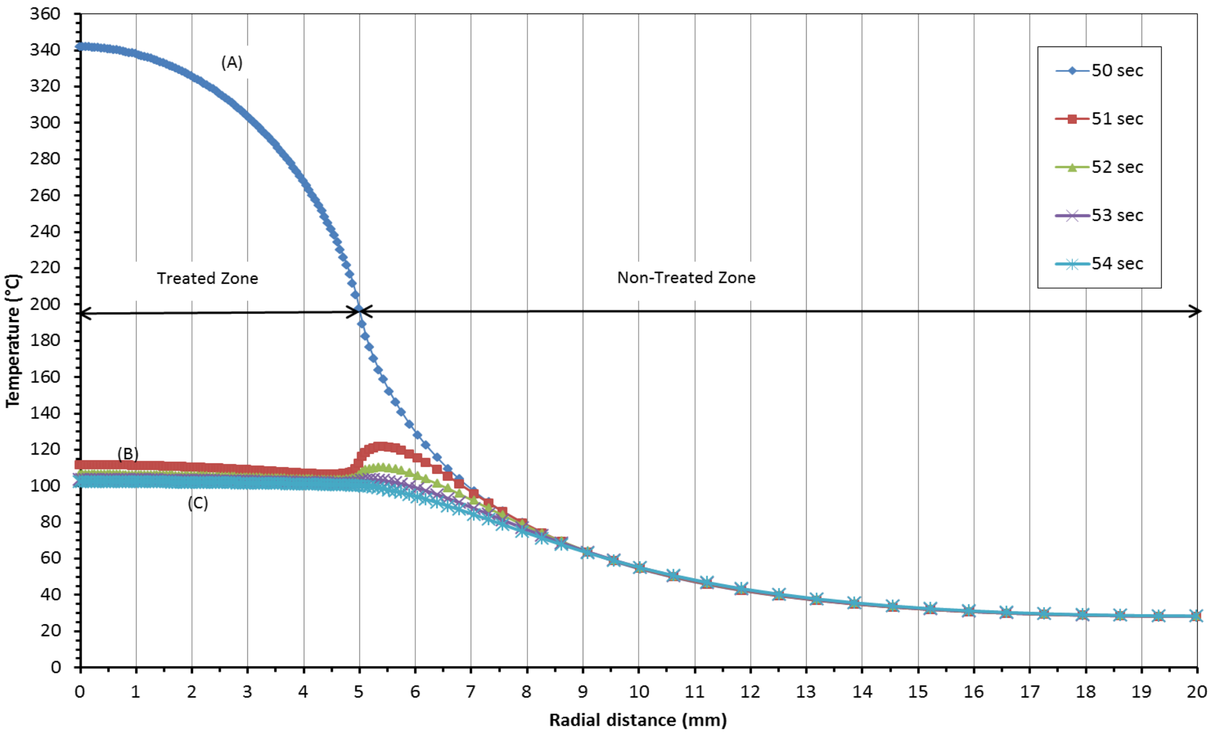

Figure 3.16: Temperature variation over the radial distance of treated surface

The variation of the temperature with the distance beneath the treated zone is shown in (Figure 3.17). During the heating phase, the rate of the temperature increase with depth is higher than that with the horizontal distance. This is related to the nature of the heating resources (microwaves). During the cooling phase, the temperature of the subsurface areas decreases rapidly up to 2 mm in depth. Under this depth, very slight change in temperature is recorded. From thermal point of view, the cooling effect is confined to 2 mm under the treated surface.

Figure 3.18 shows the temperature profiles in the subsurface areas. We observe that the profiles are similar to that at the surface of the treated area. A difference of 30 °C is recorded between the maximum temperatures of two layers. That means a temperature gradient of 60 °C /mm.

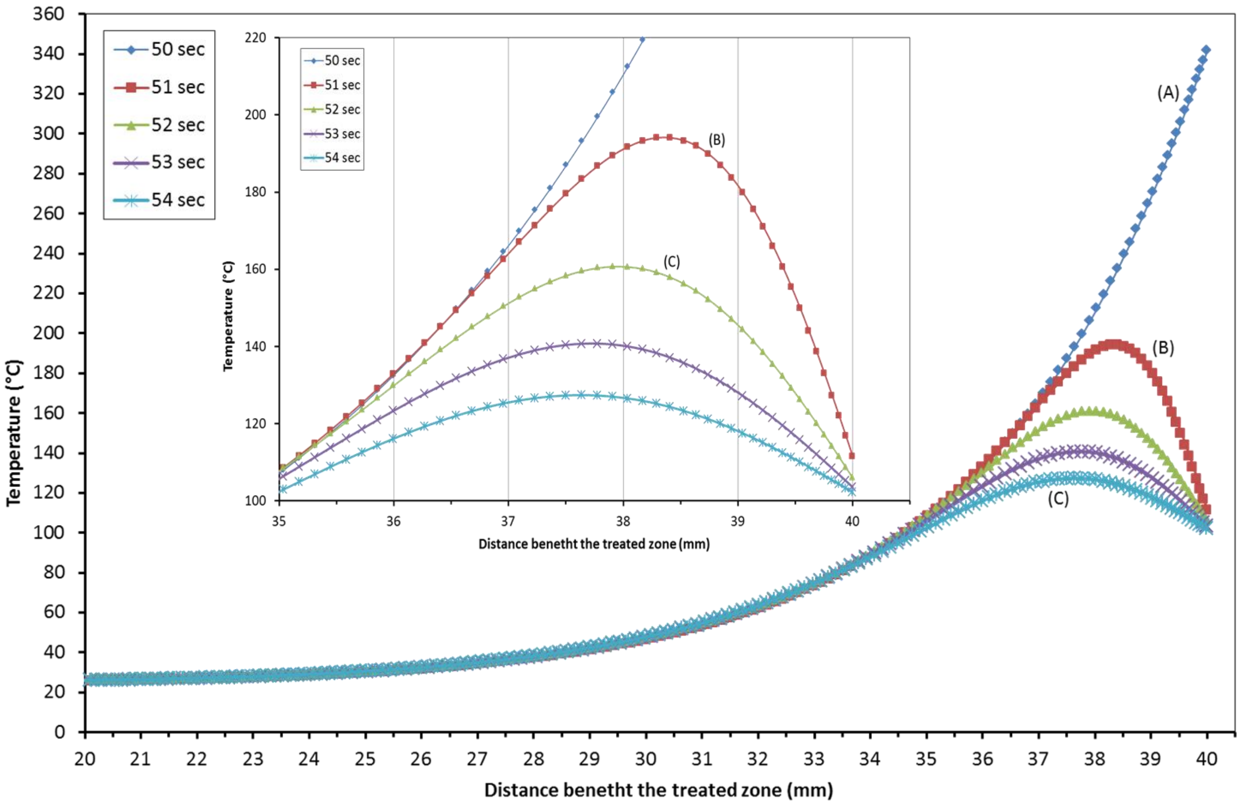

Figure 3.17: Temperature variation with the depth beneath the treated surface

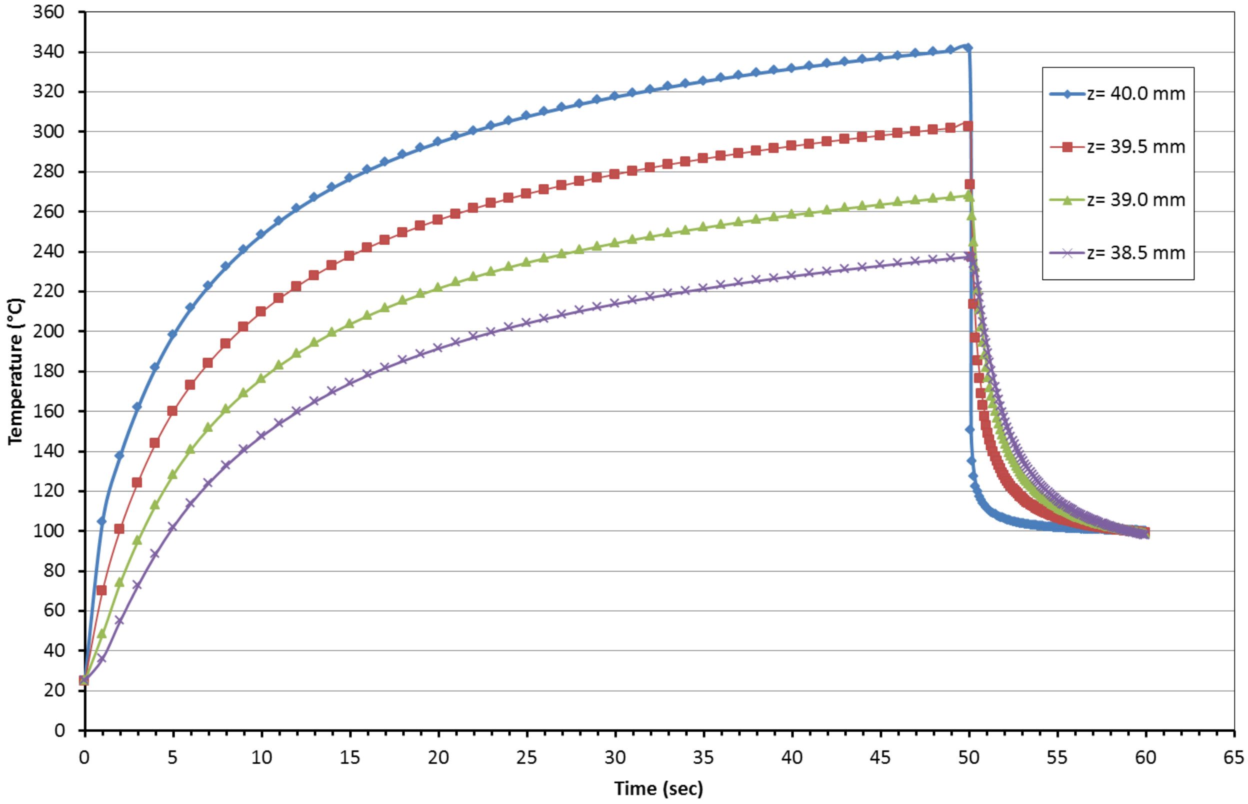

Figure 3.18: Temperature profiles in the subsurface areas under the treated surface

Influence of the heating period

Figure 3.19 shows the influence of the heating period on the variation of the temperature at the surface of the treated area. The maximum temperature increases with the increase in the period of heating. The increase is important up to 50 sec, but then reduces. After 50 seconds of heating, the maximum temperature reaches 340 °C while after 200 seconds it reaches 390 °C. That means additional heating during 150 seconds results in a temperature increase of 50 °C.

These results recommend a heating time of 50 seconds. This time is less than that suggested by (Ross, 1964), which is equal to three minutes. After the 50 seconds the temperature does not undergo significant variation. So this period of heating could be described as the yield time to get the maximal temperature i.e. below this period the desired max temperature would not be reached and no micro-cracks would be initiated where it needs 44 seconds to initiate cracks in the granite (Finnie et al., 1979).

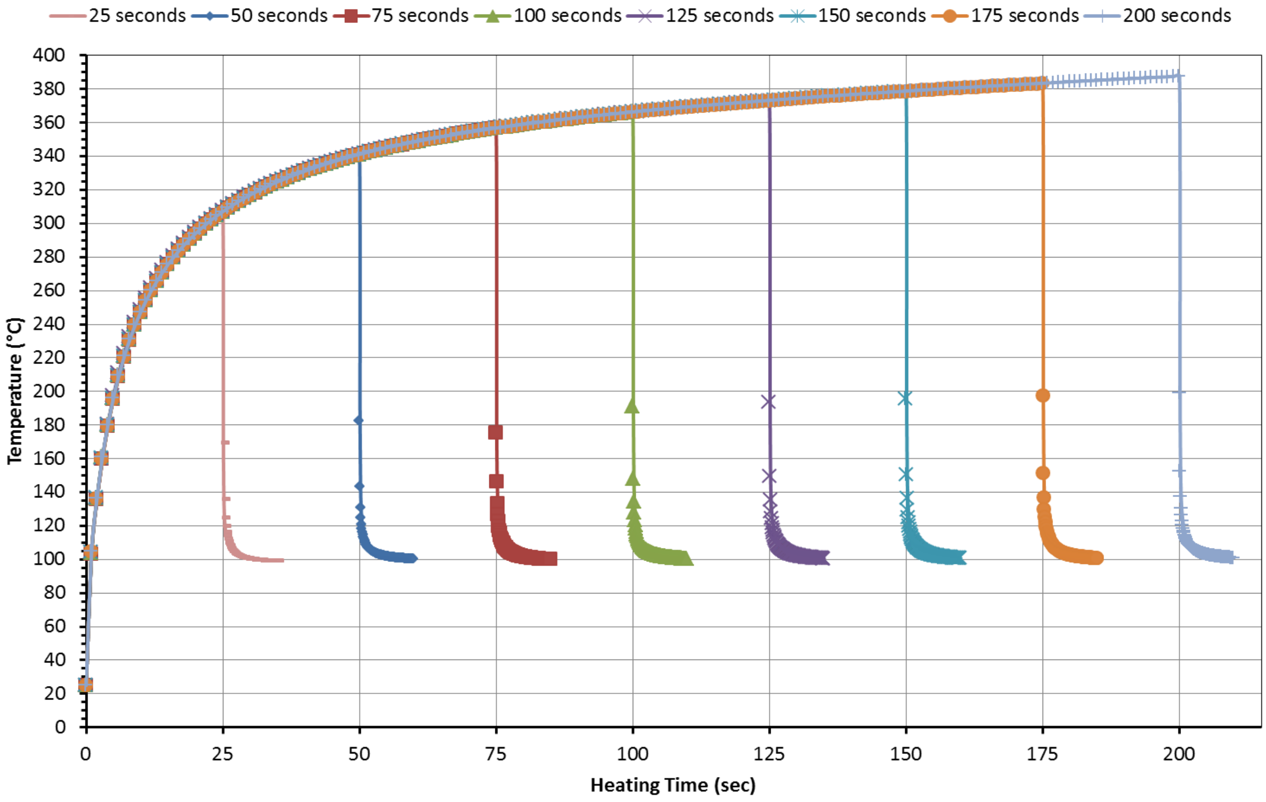

Figure 3.19: Temperature profile due to different time of heating just between (25 and 200 seconds).

Influence of the Heat exchange coefficient and the coolant temperature

The heat exchange coefficient between the heated surface and the coolant is a crucial factor in the cooling process. Analyses were conducted with 7 coolants (Table 3.2) where heat exchange coefficient varies between 4 and 113000 W/(m^2.K).

Table 3.2 : Heat convection coefficient values (Vlachopoulos and Strutt, 2002)

Type of coolant	W/m².K
Air free convection	4 to 28
Water free convection	300 to 1500
Air forced convection	4 to 570
Water forced convection	300 to 17000
Oil forced convection	50 to 2000
Boiling Water	3000 to 60000
Condensing Water vapor	5000 to 113000

Figure 3.20 shows the influence of the heat exchange coefficient on the variation of the temperature at the surface of the heated area. We observe an important influence of this coefficient. At low values of this coefficient, the temperature decreases slowly. After 10 sec, it does not reach the coolant temperature. With this low value of the heat exchange coefficient, the heat will be transmitted to the surrounding area before the effect of cooling reaches the subsurface areas. Consequently, we cannot obtain the objective of changing the compressive stresses into tensile stresses. At high values of the heat exchange coefficient, the temperature drops very quickly at the surface. Consequently we obtain good performance of the process at high values of the heat exchange coefficient.

Figure 3.21 shows the influence of the temperature of the coolant on the variation of the temperature at the heated surface. It shows that the decrease of this temperature from 100 to 20°C does not affect the instantaneous drop of the temperature at the beginning of the cooling process, but it affects the temperature at the end of the cooling process. Since the instantaneous drop constitutes the major factor in the efficiency of the process, the temperature of the coolant (in the range 20 - 100 °C) is not important in determining the cooling profile. As the temperature difference between the attained maximum temperature and the coolant temperature is expected to have the major effect on the mechanical response, the maximum temperature could be risen by increase in the power intensity to maintain the same effective temperature difference.

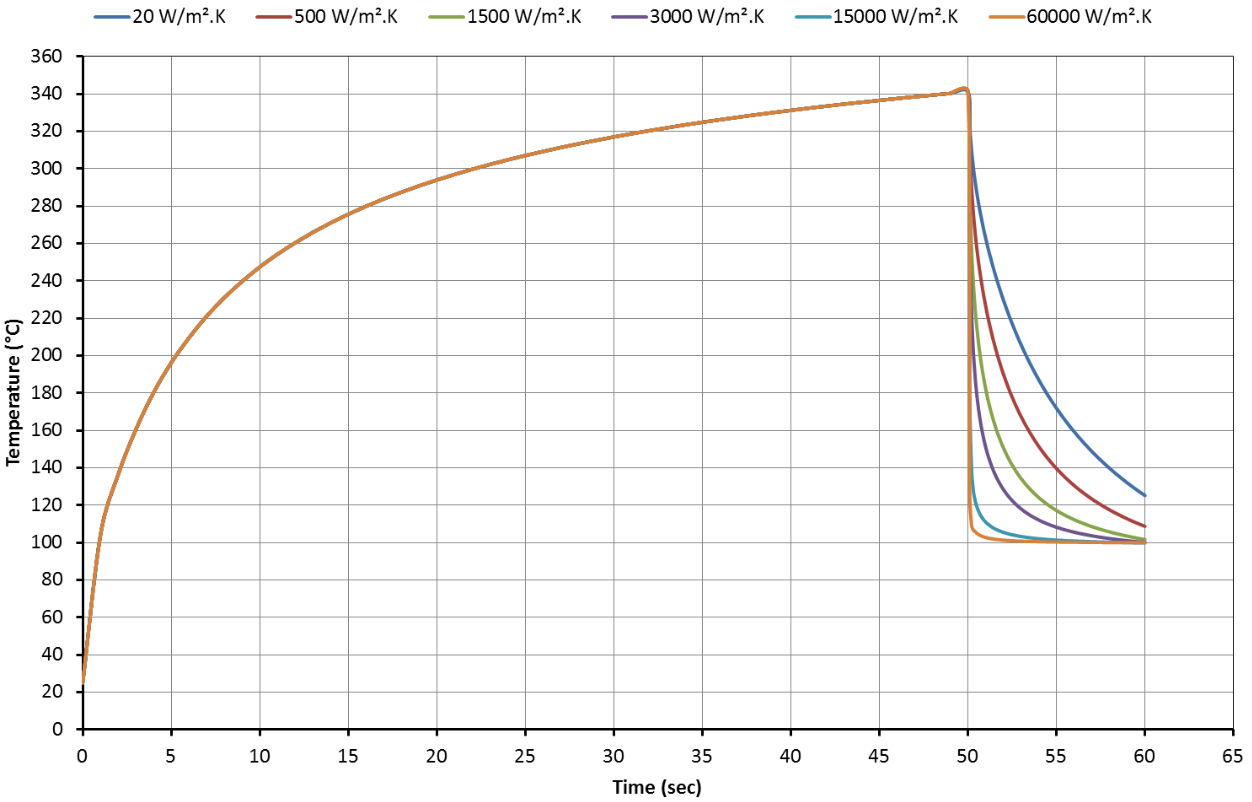

Figure 3.20 Temperature profile according to different values of heat exchange coefficient

Influence of the power intensity on the temperature profile:

Figure 3.22 shows the power intensity variation on the temperature profile. The increase in the power intensity from 0.15 MW/m² to 0.45 Mw/m² caused an increase in the maximum temperature from 340 °C to 975 °C.

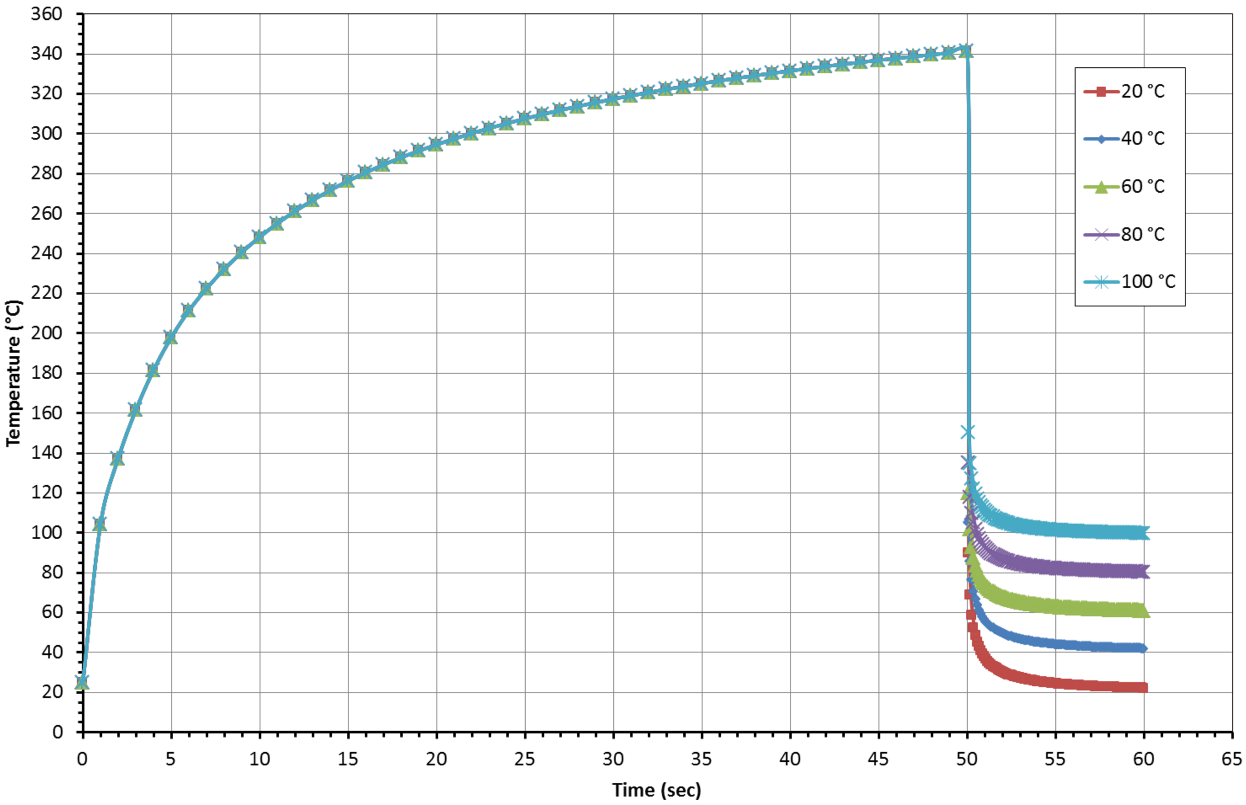

Figure 3.21 Coolant Temperature influence on the temperature profile

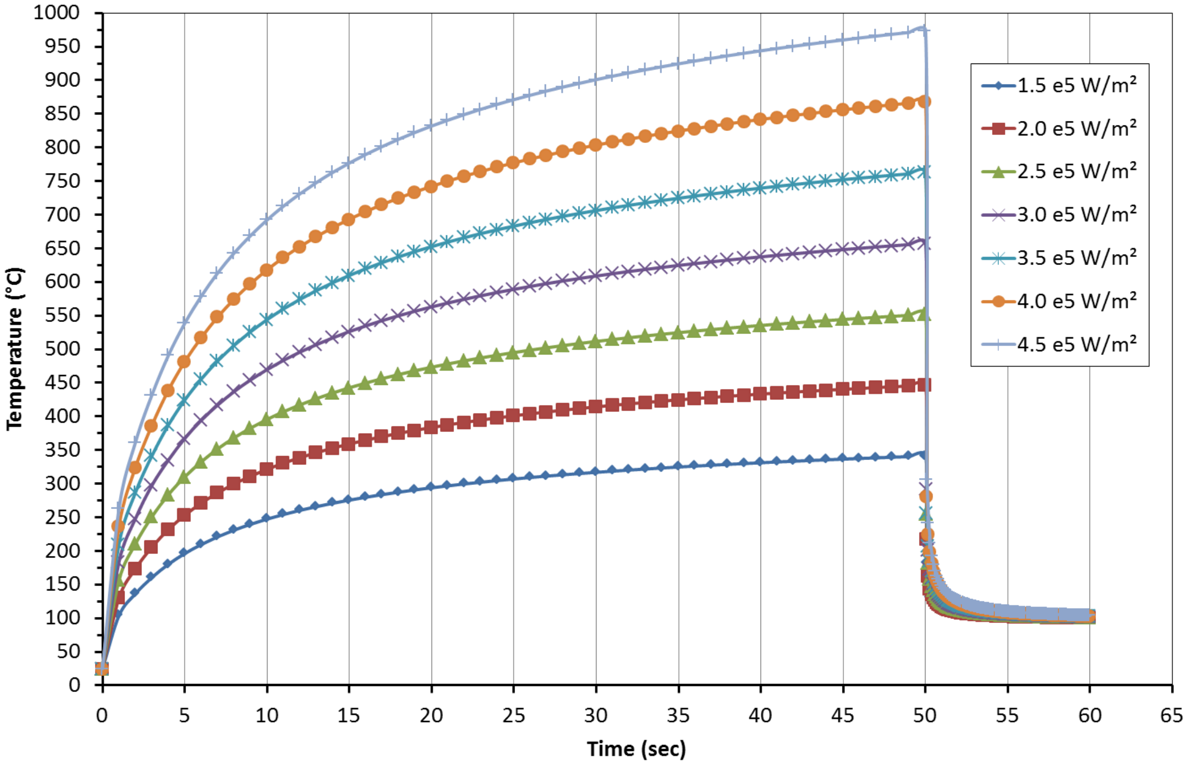

Figure 3.22: The Temperature profile according to different power intensity

3.5.3 Mechanical response

The mechanical response of the sample will be investigated according to the following issues:

- The capacity to transform the compressive stresses into tensile ones during the heating/cooling process.
- The penetration of the tensile stresses.
- The influence of some parameters on the efficiency of the heating/cooling process.

3.5.3.1 Reference case

Figure 3.23 shows the distribution of the radial stress at the surface of the sample at different times (t = 50, 51, 52, 53 and 54 sec). We observe that at the end of the heating stage (curve A), the treated area is totally submitted to compression. This result is consistent with the Preston description (1934). The magnitude of the compressive stress attains 70 (MPa) at the center of the treated area. In the non-treated area, we observe compression radial stress up to 20 mm from the sample center. The variation of the radial stress agrees with the observations of Farra (1968). At this level of compressive stress, the crack initiation threshold of the granite is theoretically attained, which is experimentally estimated to be between 20~30% of the compressive strength (Vasconcelos and Lourenço, 2008) (Eberhardt, 1998). Therefore, the sample is potentially damaged and the micro-cracks are theoretically initiated and a reduction in the compressive strength is expected to be 16% (Hommand-Etienne and Hourpert, 1989) (Chaki et al., 2008).

Immediately after the cooling phase, we observe an important change in the radial stress. In the treated area, the radial stress change from compressive stress to tensile stress. At the center of the sample, the tensile stress reaches 25 MPa. Toward the outside of the treated area, we observe a drop of the tensile stress, but we do not observe a change to compressive stress. The amplitude of the radial stress decreases with time. After 4 sec of cooling (curve C), the radial stress at the center of the sample drops to 5 MPa.

Figure 3.24 shows the distribution of the tangential stress at the surface of the sample at different times (t = 50, 51, 52, 53 and 54 sec). We observe that at the end of the heating stage (curve A), the treated area is submitted to “negative” tangential stress. The magnitude of this stress attains 70 (MPa) at the center of the treated area. In the non-treated area, a “positive” tangential stress is noticed. Immediately after the cooling phase, we observe an important change in the tangential stress. In the treated area, the tangential stress changes from “negative” to “positive” stress. At the center of the sample, the tangential stress reaches 25 MPa. Out of the treated area, we observe a small variation in the tangential stress. The amplitude of the tangential stress in the treated area decreases with time. After 4 sec of cooling (curve C), the tangential stress at the center of the sample drops to 5 MPa.

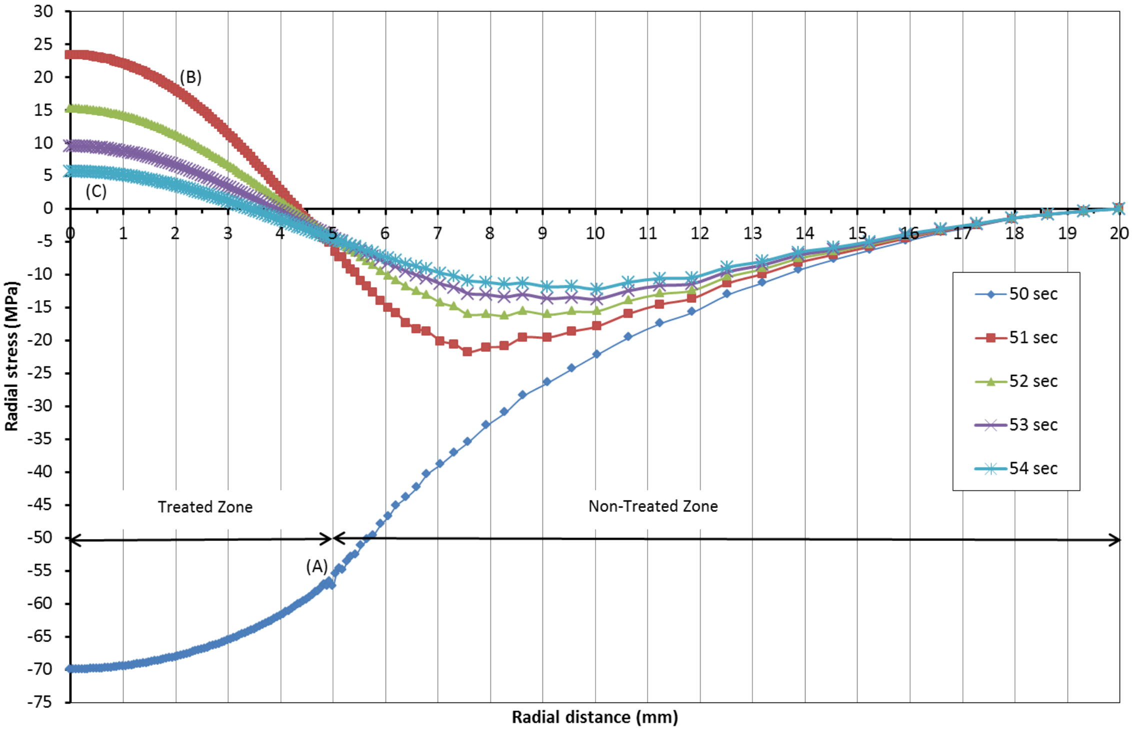

Figure 3.23: Radial stress variation over the treated zone at different moments

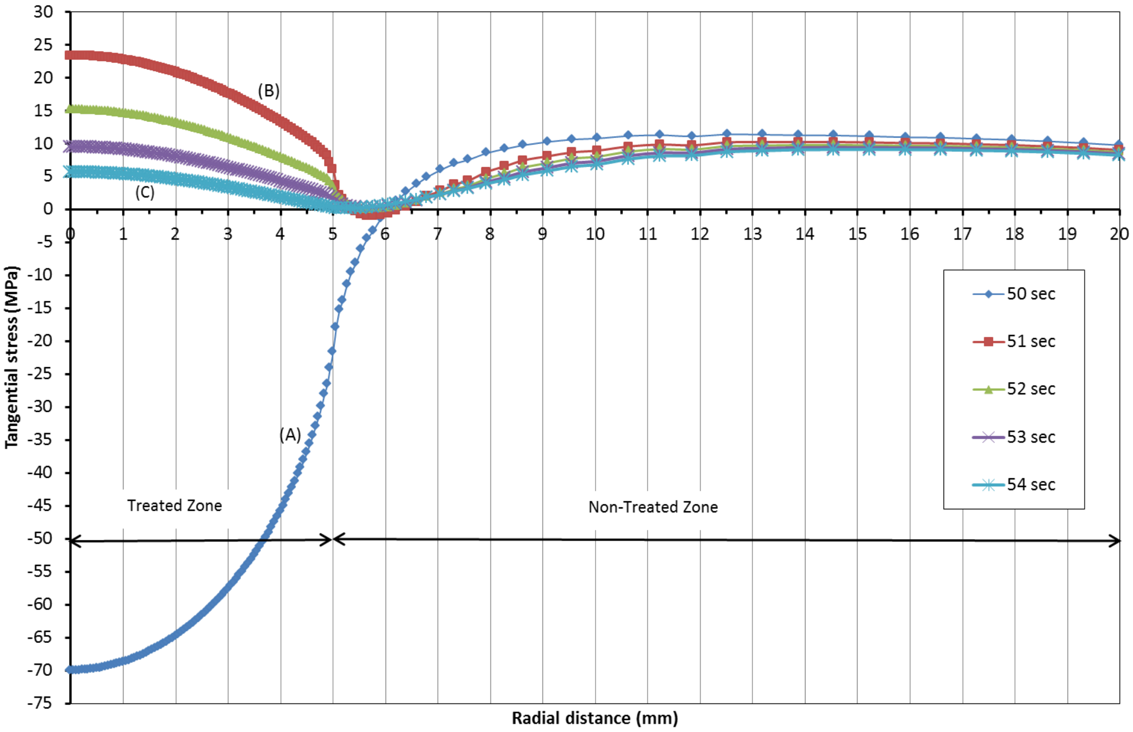

Figure 3.24: Tangential stress variation over the treated surface at different moments

Figure 3.25 presents the spatial distribution of both the temperature and radial stress in the sample at t = 50 and 51 sec. At the end of the heating stage (t = 50 sec, figure a), we observe a concentration of the high temperature in the zone close to the treated zone (till 5 mm of depth). In the beginning of the cooling phase (t = 51 sec, figure b), the temperature of the treated area drops to 120 °C; the temperature of the non-treated zone becomes higher than in the treated area.

Concerning the radial stress, we observe at the end of heating phase (t = 50 sec, figure c) compressive stress in the zone close to the treated area with a magnitude, which decreases with the distance from the treated area. At the beginning of the cooling phase (t = 51 sec, figure d), we observe a change from compression to tension in a small zone close to the surface of the treated area, while tensile stress stays in the other zone.

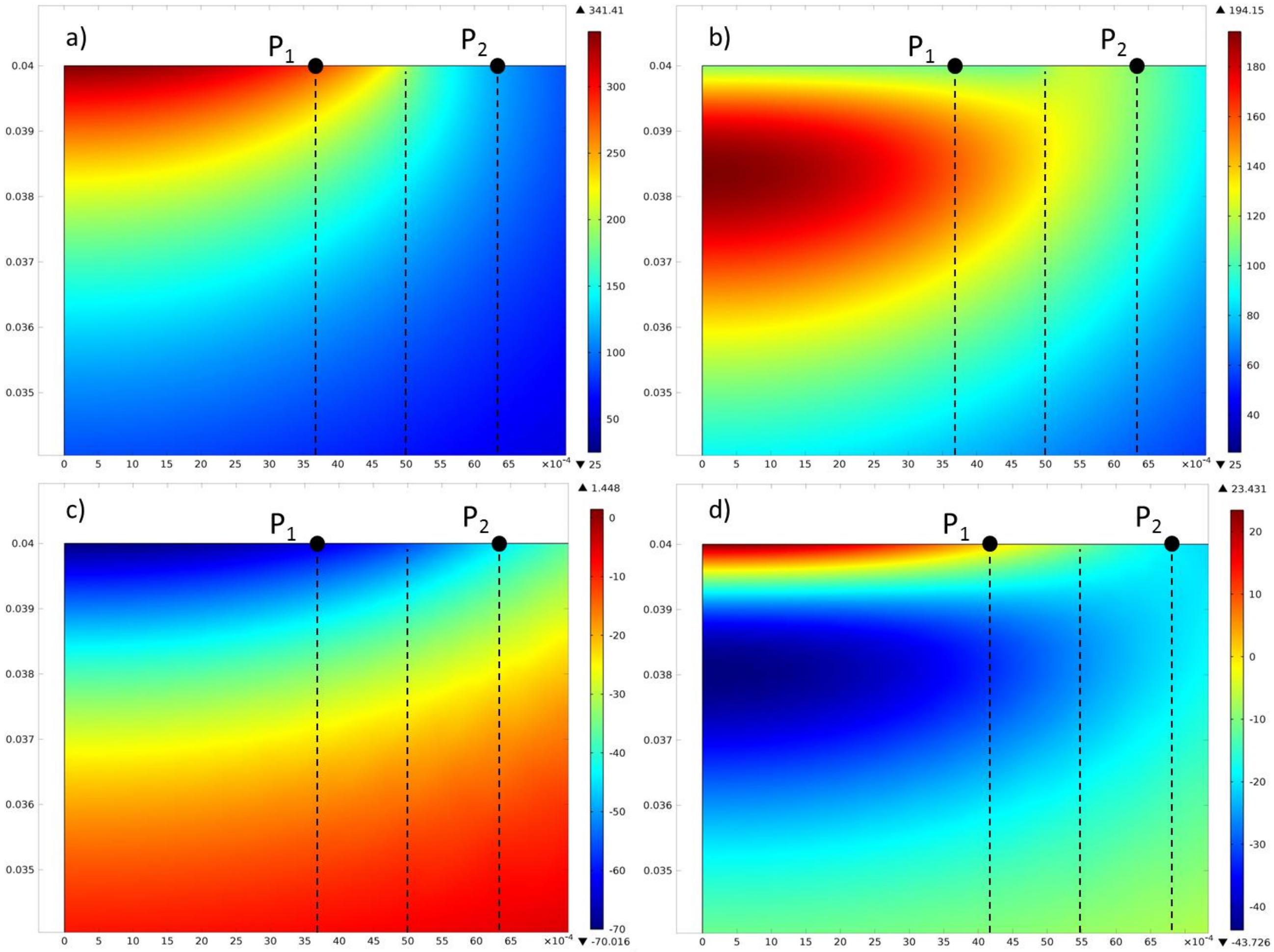

Figure 3.25: a) Temperature spatial distribution at the second 50, b) Temperature distribution at the second 51, c) Radial stress distribution at the second 50, d) Radial stress distribution at the second 51 second

3.5.3.2 Parametric analysis

Influence of the heat exchange coefficient h_c

A parametric study was conducted to illustrate the influence of the heat exchange coefficient on the stress distribution. Analyses were conducted with power intensity = 0.15 MW/m², heating time = 50 seconds and coolant temperature = 100 °C. Figure 3.26 shows the influence of ***hc*** on the stress distribution. We observe that the change in ***hc*** influences both the nature of the radial stress (compressive or tensile) as well as the magnitude of this stress. At low values of ***hc*** (20 and 50 W/(m^2.K), the cooling phase does not transform the radial stress from compression to tension. While at high values of ***hc*** (1500 W/(m^2.K)), we observe a transformation of the radial stress from compression to tension. The amplitude of the tensile stress depends on the value of ***hc.***

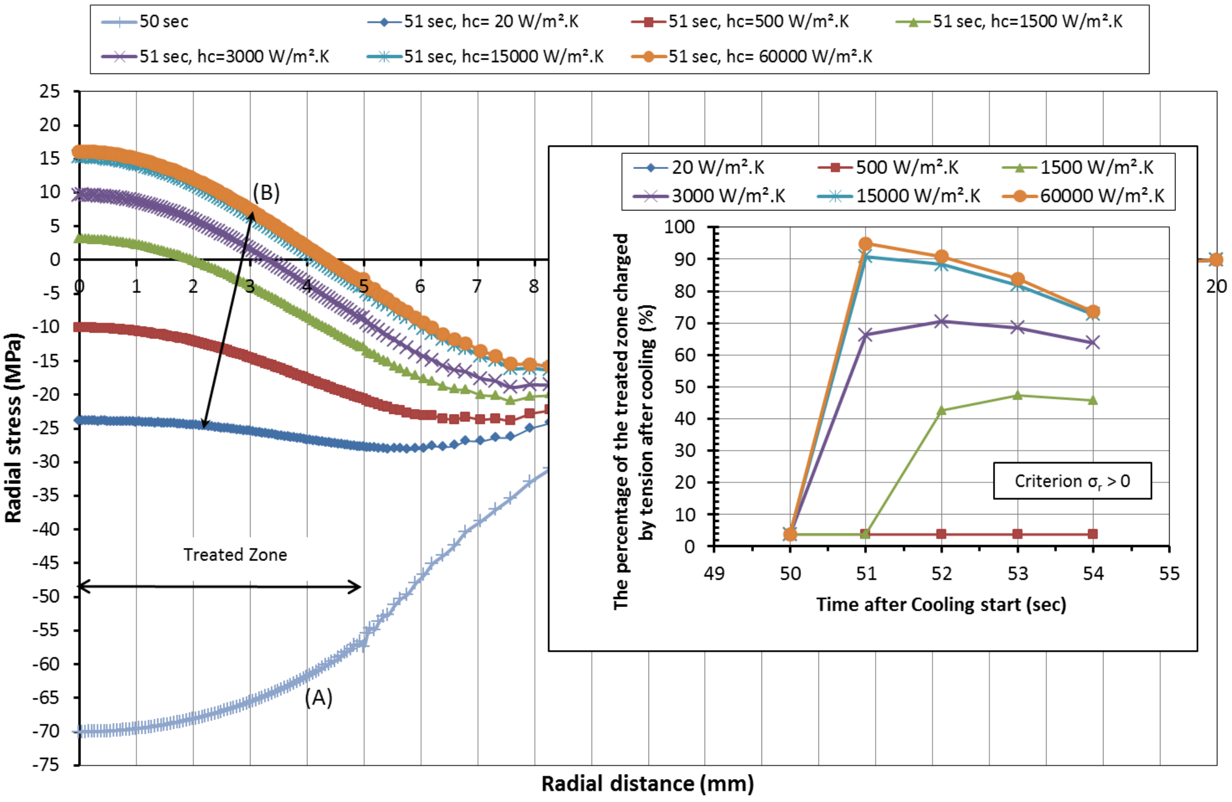

Figure 3.26: The effect of heat exchange coefficient on the conversion process

Figure 3.27 illustrates the variation of the stress with the value ***hc***. At the beginning of the cooling phase (t = 51 sec), we observe tensile stress for ***hc*** higher than 3000 W/(m².K), while we observe compression stress for ***hc*** lower than 500 W/(m².K).

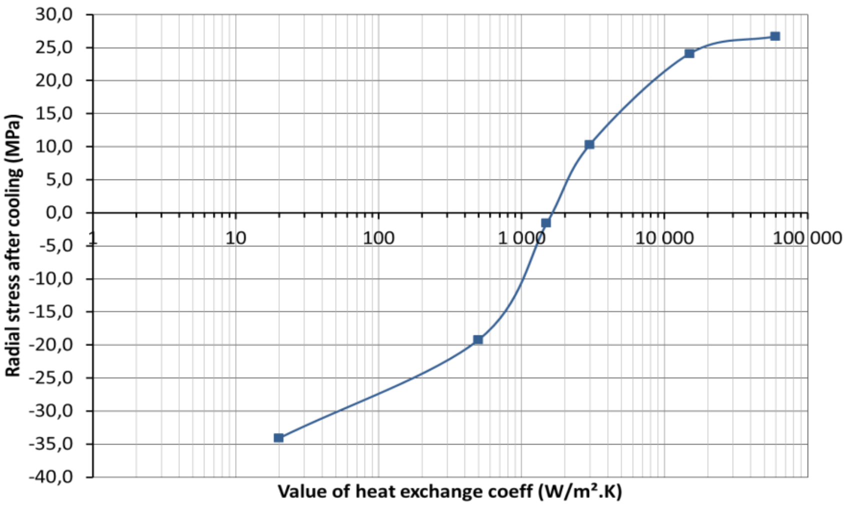

Figure 3.27: variation of stress value with heat exchange coefficient after cooling start (moment: 51 sec)

Influence of the power intensity *I*

The increase in the power intensity affects the heating and cooling phases (Figure 3.28). At the end of the heating phase, it leads to an increase in the compressive stress due to the increase in the maximum temperature. In the beginning of the cooling phase (t = 51 sec), the increase in the power intensity induces an increase in the tensile stress as well as in the extension of the area subjected to tensile stress.

Figure 3.29 shows the influence of the power intensity and the induced tensile at t = 51 sec. We observe a linear variation between these parameters. A high level of irradiation leads to high temperature in the treated zone. This elevated temperature could exceed the melting point of the rock material and negatively influences the performance of the thermal treatment.

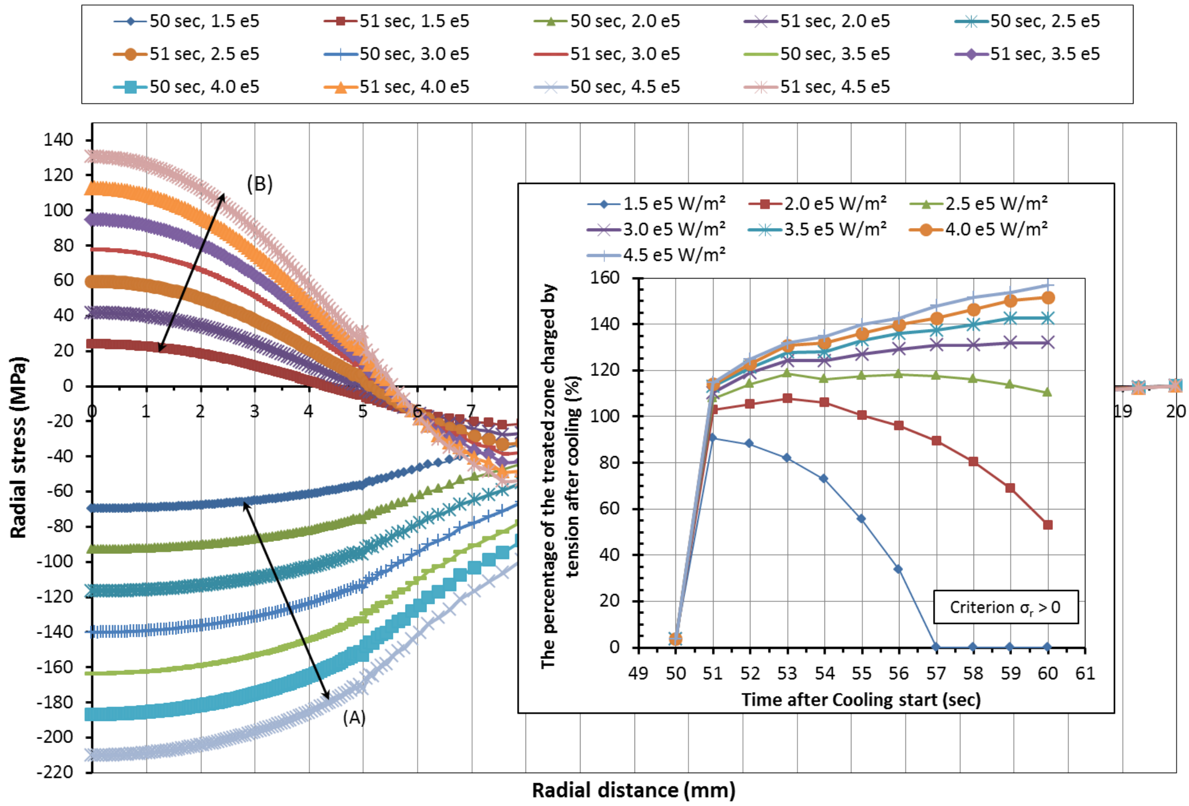

Figure 3.28: Influence of the power intensity on the conversion process

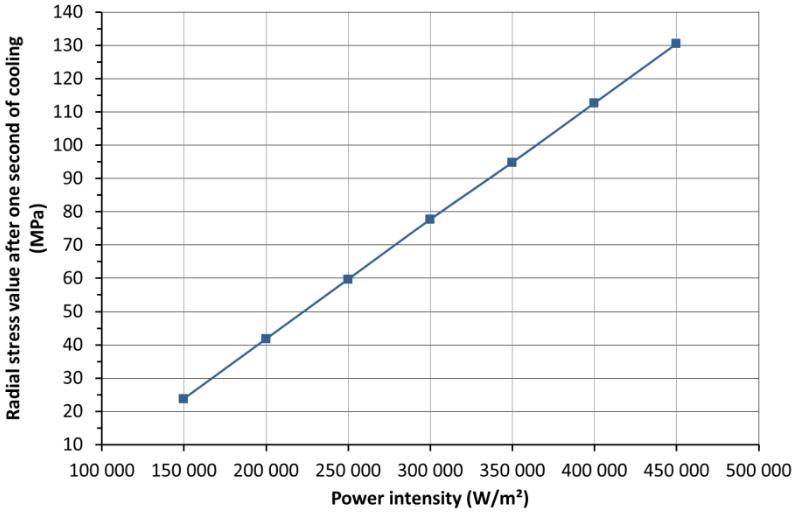

Figure 3.29: The relationship between power intensity and the induced tensile stress (at moment: 51 sec)

Influence of the coolant temperature T_{ext}

Figure 3.30 presents the influence of the coolant temperature on the stress variation during the heating/cooling process. It shows that the decrease in the coolant temperature from 100 to 20° C, induces an increase in the tensile stress in the treated area as well as in the extension of the zone subjected to tensile stress. Figure 3.31 shows the variation of the amplitude of the tensile stress with the coolant temperature. It shows a linear variation between these parameters. The decrease of the coolant temperature from 100 to 20°C leads to an increase in the tensile stress from 23 to 55 MPa.

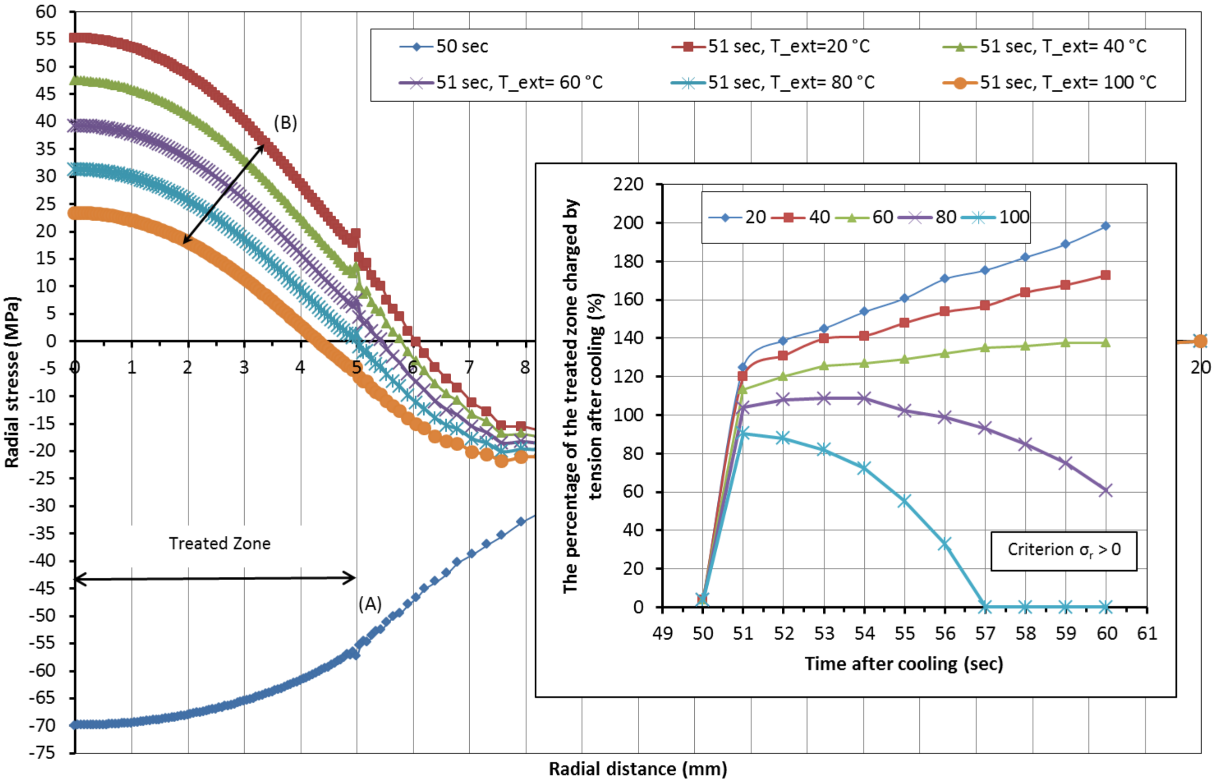

Figure 3.30: Influence of the coolant temperature on the conversion process

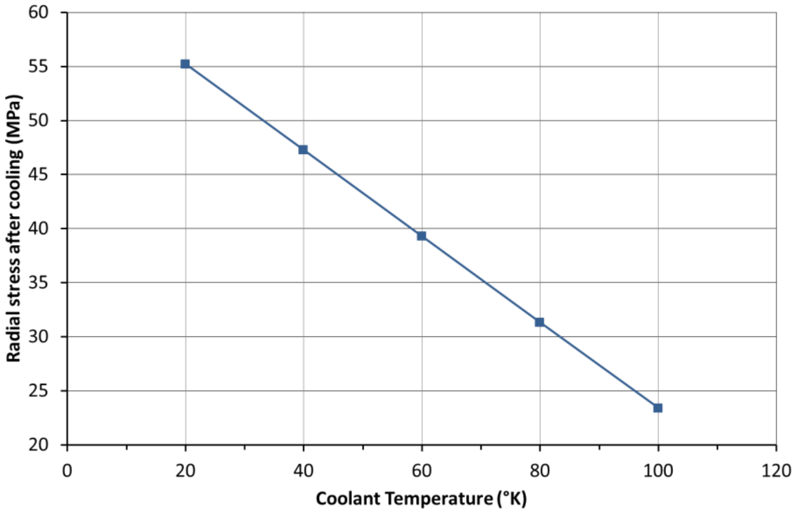

Figure 3.31: Variation of induced tensile stress with coolant temperature (at moment: 51 sec)

3.5.3.3 Penetration depth (PD)

The penetration depth is a crucial parameter in the thermal process. It describes the efficiency of the proposed method. The depth of the thermal damage by heating was estimated to one or two grains size (Rauenzahn and Tester, 1989) and (Walsh et al., 2011) (Walsh et al., 2012).

Figure 3.32 shows the variation of the radial stress with depth at different time intervals t = 50, 51, 52, 53 and 54 sec. At the end of the heating phase, compression is induced in the sample up to 10 mm in depth. During cooling phase, three zones can be observed: the contracted zone, the compressed zone and low tensile stress zone. In the first zone, the tensile stress is largely restrained in the superficial layers beneath the treated zone. The tensile stresses in this zone show quasi-linear variation with depth (from 0 MPa to 25 MPa). Below this depth, a part of the sample is still submitted to compression (between 5 MPa to 45 MPa). The last zone is submitted to lows tensile stress.

A simple criterion is used to evaluate the penetration depth. This criterion is related to the change in the nature of the stress (from compression to extension). Figure 3.33 shows the variation of the penetration depth during the cooling phase. We observe firstly an increase in the penetration depth. It increases up to 0.40 mm during the 3 first seconds (t = 53 sec). Then it decreases gradually and disappears after 7 sec of cooling. The low value of the penetration depth (0.4 mm) could be attributed to:

- The coolant (Water at 100 °C) is unable to create the required difference between the preheated spot temperature and the coolant temperature; this difference is important to transform the compressive stress into tensile stress. In other words, the energy extraction in this case is not sufficient.
- The maximum reached temperature at the end of the heating phase is not sufficient to generate the desired temperature gradient.

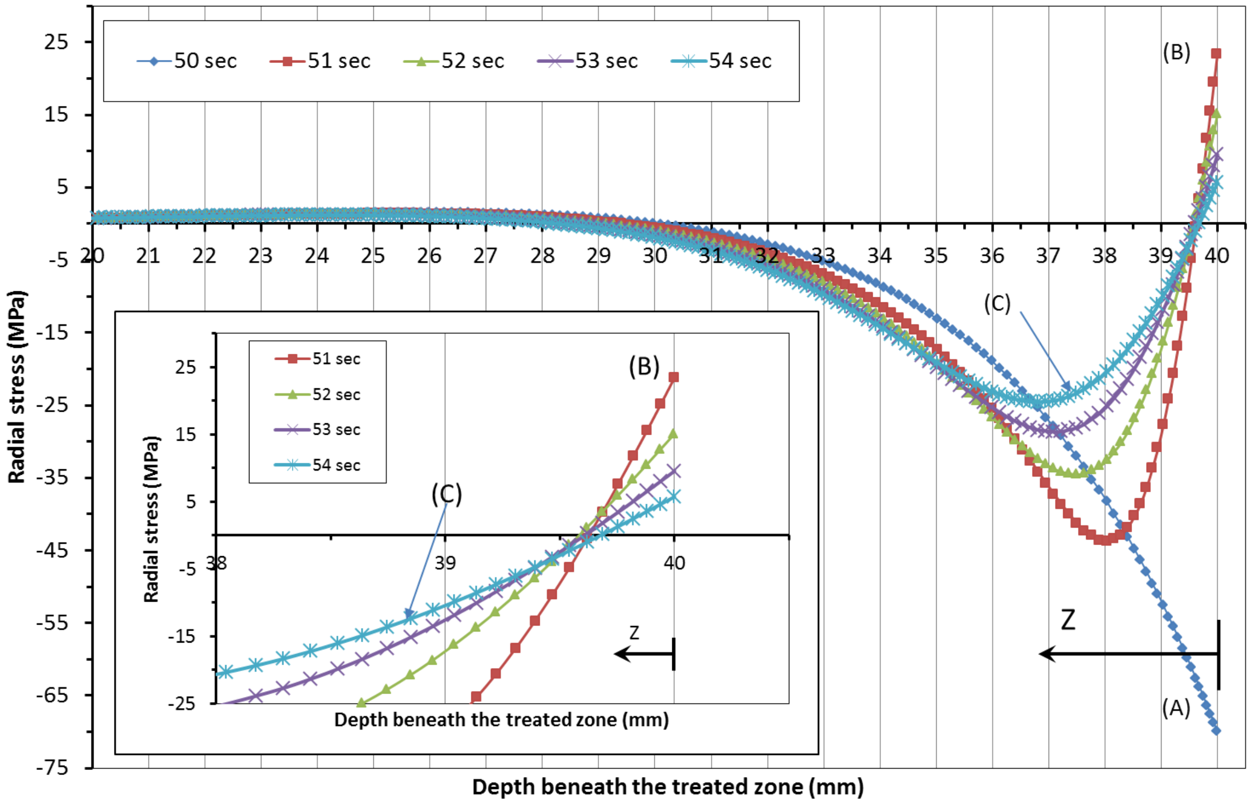

Figure 3.32: Radial stress profile with the depth of the sample at different moments

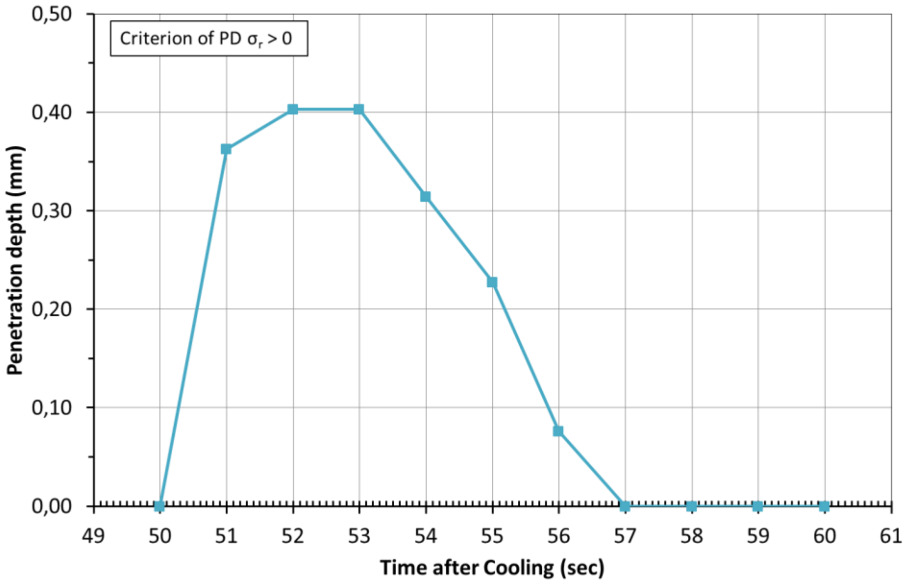

Figure 3.33: Variation of penetration depth over the cooling time

Influence of the irradiation density

Figure 3.34 shows the influence of the irradiation density on the penetration depth. At lower irradiation level (0.15 MW/m^2), the penetration depth is low (0.4 mm). The increases in the irradiation density induce an increase in the penetration depth. At high irradiation energy (> 0.35 MW/m^2), the penetration depth increases up to 1 mm. However, at high radiation density (0.45 MW/m²) the heating phase induces a temperature close to the melting point of the rock material (between 900 °C and 1200 °C.), which is not recommended for spallation. Figure 3.35 shows a quasi-linear variation between the penetration depth and the irradiation intensity.

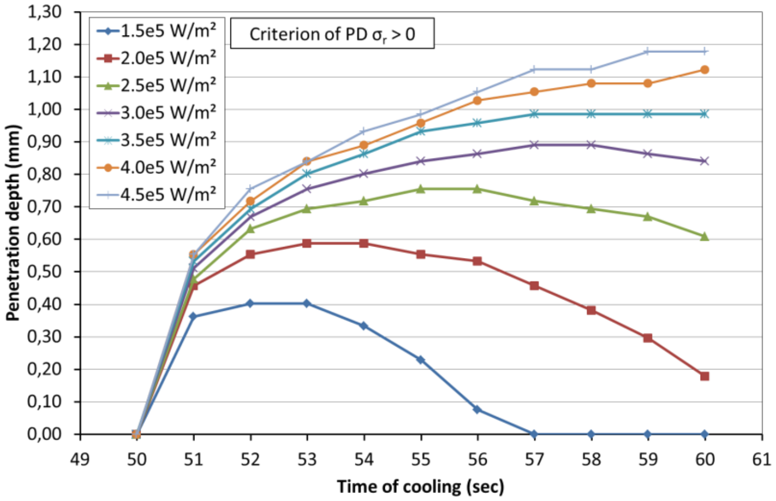

Figure 3.34: Variation of penetration depth with time due to different irradiation density

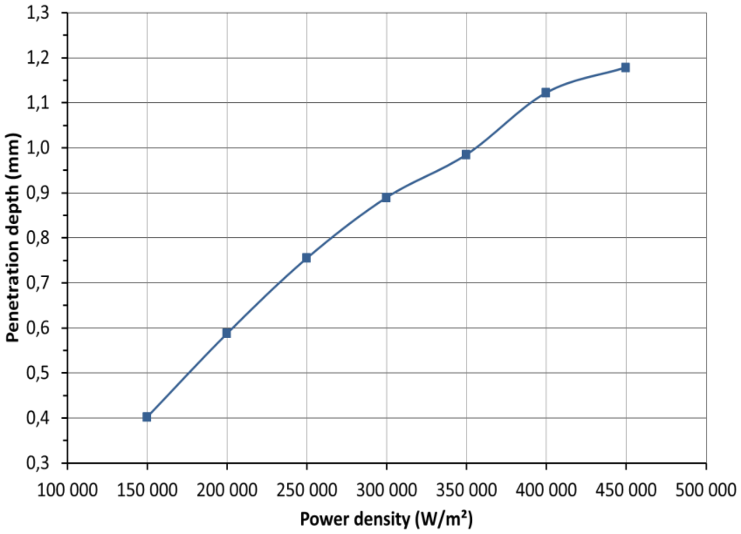

Figure 3.35: The maximum attained penetration depth as a function of the power density

Influence of the heat exchange coefficient h_c

Figure 3.36 shows the influence of the heat exchange coefficient on the penetration depth. We observe an increase in the penetration depth with the increase in h_c.

The increase in the penetration depth is significant when $\mathbf{h_c}$ increases from 20 and 15000 W/(m².K), then the increase in the depth becomes very low beyond 15000 W/(m².K).

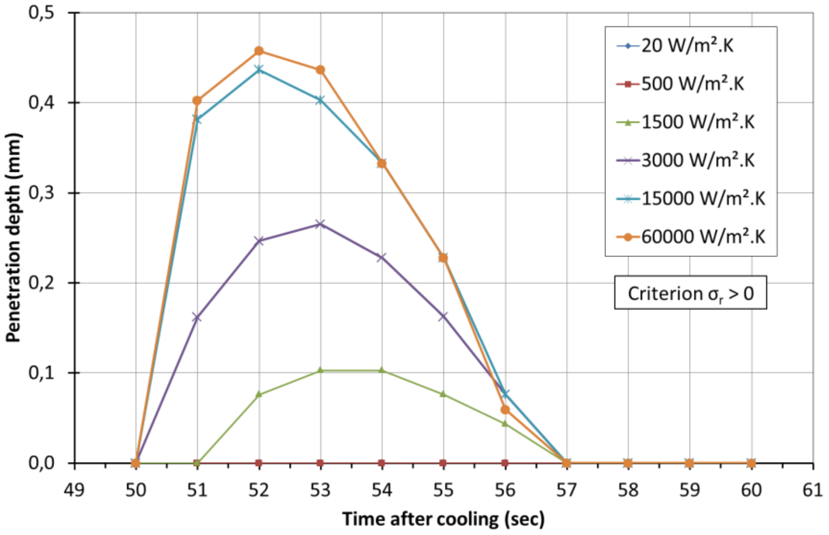

Figure 3.36: The profile of the penetration depth over time due to the variation of heat exchange coefficient

Influence of the coolant temperature

Figure 3.37 (a) and (b) show the influence of the coolant temperature on the penetration depth. We observe an increase in the penetration depth with the decrease in the coolant temperature. At high values of the latter (100 and 80 °C) the penetration depth is low (0.6 mm), at a coolant temperature of 60°C, the penetration depth increases to 1 mm, and attains 1.8 mm at a coolant temperature of 20°C.

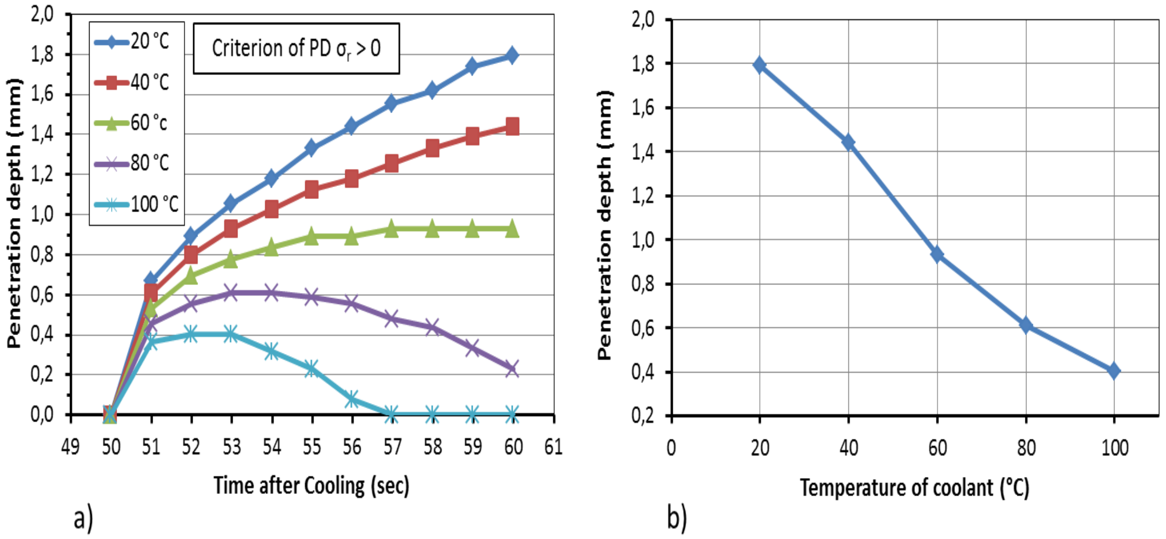

Figure 3.37: a) Evaluation of the penetration depth according to different coolant temperatures, b) Variation of maximum attained penetration depth with coolant temperature

Influence of heating period

Figure 3.38 (a) and (b) show the influence of the heating period on the penetration depth. We observe an increase in the penetration depth with the increase in heating period. At low values of the heating period of the latter (25 and 50 sec °C) the penetration depth is low (0.4 mm), at heating period of 150, the penetration depth increases to 0.8 mm, and attains 1.35 mm for a heating period of 300 sec.

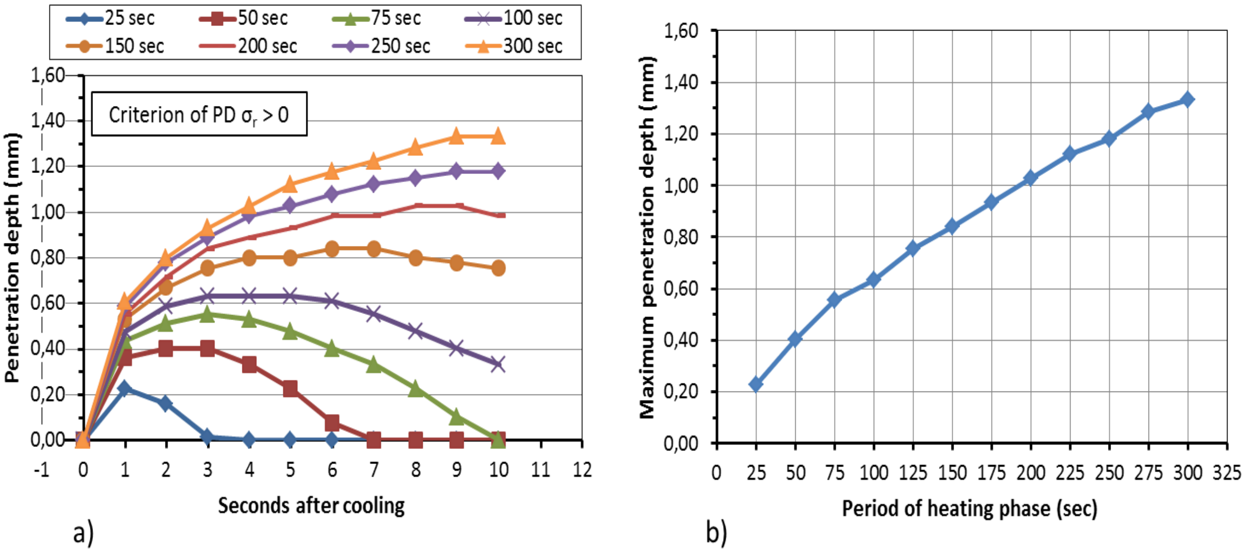

Figure 3.38: a) variation of penetration depth profile according to different heating period, b) variation of penetration depth with heating period

3.6 Summary and conclusion

This chapter included a numerical investigation of the efficiency of the heating/cooling process in rock material fracture. It showed that the heating stage induces compressive stresses around the heated surface, which could exceed the rock compressive strength and consequently lead to rock fracture or to the initiation/development of micro-racks. The cooling phase transforms the compressive stresses into tensile stress in a zone close to the treated area. This change in the nature of the stresses could amplify the rock fracture or the initiation/development of micro-cracks, because the rock strength to tensile stresses is lower than that to compressive stresses.

Parametric analysis showed that the efficiency of the thermal treatment depends on the following parameters: the density of the irradiation energy, the period of the heating phase, the heat exchange coefficient and the temperature of the coolant.

The increase in the energy irradiation density has positive influence on both the thermal and mechanical aspects. It leads to an increase in the maximum temperature, in the penetration depth as well as in the compressive and tensile stresses. Consequently it has a positive role in the rock treatment. However, a high level of irradiation density could lead to rock melting; attention should be taken to avoid this phenomenon. The increase in the heating period has an important influence on the penetration depth. The increase of this period from 25 sec to 300 sec leads to an increase in the penetration depth from 0.2 mm to 1.35.

Analysis showed also an important role of the heat exchange coefficient. The increase of this coefficient leads to an increase in both the tensile stress and the penetration depth. The temperature of the coolant affects also the magnitude of the tensile stresses as well as the penetration depth. The decrease of this temperature from 100° C to 20° C leads to an increase of about 400% in the penetration depth.

The repetition of the heating/cooling process leads to a cyclic change in the stresses around the treated area from compressive to tensile stresses. This cyclic change plays an important role in the rock deterioration. In the following chapter, we present a deep analysis of this phenomenon.

CHAPTER 4

ANALYSIS OF THE CYCLIC THERMAL PROCESS AND ITS INFLUENCE ON THE PENETRATION RATE

4.1 Introduction

In the previous chapter the rock fracture due to the heating/cooling process was analyzed using an elastic linear model for the rock material. Since both the heating/cooling process and the induced strains (stresses) induce damage in the rock material, analysis should take into account this damage. In addition, we have considered only one cycle of heating/cooling. Since this cycle leads to a rock spallation in the treated area with only 1 mm in depth, we have to repeat this cycle in order to reach significant excavation depth.

This chapter presents a numerical modeling of the rock excavation using the heating cooling process taking into account the rock material damage and the repetitive loading heating/cooling process.

In the first part of the chapter, we present the numerical model used in the analysis with a particular focus on the damage law, then the application of this model to the first heating/cooling cycle and finally its application to the following cycles.

4.2 Presentation of the adopted continuum damage model

4.2.1 The damage Constitutive law

The rock materials have generally brittle behavior. Their fracture is usually represented by the formation of new micro-cracks or the propagation of the existing cracks due to either mechanical or thermal loadings. The initiation, propagation and coalescence of these micro-cracks result in the degradation of the rock material strength and relatively its mechanical properties Like the Young modulus. Since the mechanistic theories of failure promotes the initiation of the fracture due to the concentration of stresses on the tips of the pre-existing flaws within the intact material, the thermal spallation of rocks theory was completely established on this idea. Similarly, the induced damage by the proposed Heating/Cooling process to induce the Rock Fracture (HCRF) will be analyzed by the use of the same theories.

The cracks in the rock material are classified in four types:

- Grain boundary cracks (crack associated with grain boundaries).
- Intra-granular cracks (cracks which lie totally within the grain).
- Inter-granular cracks (cracks which extend from a grain boundary crossing into another grain).
- And multi-granular cracks (cracks which cross several grains and grain boundaries).

The modeling of the crack initiation, propagation and coalescence process in the brittle material like rocks is very complex where many factors influence the initiation and propagation process in the rock structure like:

- Critical crack length
- Critical crack orientation
- Direction of crack propagation
- The stability of crack propagation and so many others.

However, the continuum damage mechanics was suggested to evaluate the induced damage within the rock material mechanical as well as thermal loads. The continuum damage mechanics was first introduced by (Kachanov, 1958) and further developed by (Lemaitre, 1985) (Kachanov, 1986) (Chaboche, 1988). The damage process has been taken into account by introducing the damage variables into the constitutive equations of the system (Liang et al., 2006).

In this chapter the continuum damage mechanics will be used to evaluate the induced damage by the proposed heating/cooling process.

Damhof et al. (2008) isotropically modeled the transient temperature damage in granular coarse grained refractory material by using elasticity-based (thermal shock) damage. The proposed damage law took into account the dependencies of the damage parameters on the temperature. The maximum attained temperature was the leading parameter of the induced thermal damage within the material where an isotropic thermal expansion due to the uniform temperature was assumed. They associated the thermal damage to the local mismatches in elastic and thermal properties of the rock components. Likewise, they proposed to model the thermal damage the variable d_{th}:

$$d_{th} = 1 + \sin\left(\frac{1}{2}\pi\left(3 - \left(\frac{k_{th} - k_{th,i}}{k_{th,c} - k_{th,i}}\right)^{\phi}\right)\right) \qquad \text{Eq 4- 1}$$

Where: k_{th} represents the attained maximum temperature. $k_{th,i}$: denotes the initial temperature for thermal damage and $k_{th,c}$ denotes the critical temperature for thermal damage. When k_{th} approaches $k_{th,c}$ the thermal damage would become 1.0. The calculated damage variable was about 0.4 corresponding to 1500 °C at the treated surface after 10 seconds of exposure (Damhof et al., 2008).

The previous form and similar ones of damage variable can’t be used in the evaluation of the damage induced by the proposed heating/cooling treatment. In heating phase, as the temperature increases the strains will also increase so that the damage will evolve. Whilst in cooling phase, the temperature decreases and consequently the evolved strains in heating phase will regress so that no damage will be evolved in this stage paradoxically with the propositions of the heating/cooling mechanism. The main degradation in the rock material strength is expected to occur during cooling phase due to extensile stresses exceed the tensile strength of the rock material.

Relatively, the evolution of the thermal damage should be evaluated depending on the change in the state of stresses from compressive (heating phase) to extensile (cooling phase). In the following paragraphs, the adopted constitutive damage law stresses based will be presented.

The adopted damage law depends on that was described by Zhao et al. (2005). He developed a continuum damage mechanics based constitutive model to simulate the failure and the impact resistance of laminated and monolithic automotive glazing subjected to head impact.

An isotropic damage was employed to introduce the degradation in the material due to damage process. The stiffness matrix of the damaged material is expressed as next:

$$K_{ijkl}^{d} = \frac{(1-D)E_0}{2(1+\nu)}\left(\delta_{il}\delta_{jk} + \delta_{ik}\delta_{jl}\right) + \frac{(1-D)E_0\nu}{(1+\nu)(1-2\nu)}\left(\delta_{ij}\delta_{kl}\right) \qquad \text{Eq 4- 2}$$

E_o and ν are initial Young modulus and the Poisson ratio. D is the isotropic damage variable.

The damage component consider one basic damage mode (Sun and Khaleel, 2004): Damage caused by principal normal stress components that manifests as an opening mode of failure (mode I).

The damage caused by maximum shear stress components (mode II) was neglected. Since the mode II crack propagation was usually dominated by the mode I growth in the experimental scale so that there is a common perception that normal tensile stress is the only driving force for crack propagation (Melin, 1986 cited by Sun and Khaleel, 2004).

The damage due to normal principal stresses was assumed to obey to simple linear damage evolution law in harmony with the failure mode I. This is expressed as:

$$D_i = \begin{cases} 0 & \sigma_i \leq \sigma_{threshold} \\ \dfrac{\sigma_i - \sigma_{threshold}}{\sigma_{cr} - \sigma_{threshold}} & \sigma_{threshold} < \sigma_i < \sigma_{cr} \\ 1 & \sigma_i \geq \sigma_{cr} \end{cases} \qquad \text{Eq 4- 3}$$

Where: σ_i is the principal stress component, $\sigma_{threshold}$ is the threshold of damage initiation and σ_{cr} is the critical damage value. Since the failure behaviors of rocks under tension and compression are different so that the suffix (i) denotes either the tensile or compressive stresses (Liang et al., 2006).

In the experimental works, the thermal damage during heating phase was already determined to reach 30% at this level of temperature 340 °C (Hommand-Etienne and Hourpert, 1989). In addition, the objective of the present analysis is to evaluate the induced damage by the cooling effect. So the induced damage by compressive stresses won't be taken into account in the calculation. Likewise, the damage due to extensile stresses will only be evaluated during the cooling phase.

The isotropic material degradation will be modeled as loss of the material stiffness:

$$\tilde{E} = (1 - D_t)E \qquad \text{Eq 4- 4}$$

Where: E is the Young's modulus of the intact material. D_t is the induced damage by the extensile stresses.

The irreversibility of the cracking and damage process was taken into account through a comparison between the actual calculated damage value at the time increment n_{th} and the corresponding value of the preceding time increment $(n-1)_{th}$ using the relationship:

$$D_i = \max(D_i^n, D_i^{n-1}) \qquad \text{Eq 4- 5}$$

4.2.2 The computational model and damage implementation in Comsol

The numerical model used in this analysis is similar to that used in the previous chapter (section…). A 2D-axisymmetric coupled electromagnetic waves, heat transfer and solid mechanics finite element model was used to simulate the whole process in the Comsol Multiphysics. Additional variables were added to consider the damage evolution as well as the stiffness and the strength degradation. Figure 4.1 shows the flowchart of the used algorithm to calculate the damage.

No damage was considered during the heating phase so no degradations in the stiffness or the strength were taken into account. Whilst during the cooling phase, the damage was allowed to evolve due to tensile stresses. Once the temperature and the stresses were analyzed in the model, the damage evaluation process started according to (Eq 4-3). If the principal extensile stress exceeds the threshold of the crack initiation $\sigma_{threshold}$, the damage starts to evolve. Thereafter, the stiffness and the strength of the rock material were consequently updated due to the actual caused degradation to be used later in the next time step calculation. The rock material behavior is elastic-brittle.

To maintain the durability of the achieved damage, numerical procedure was conducted. This procedure consists of examining the time derivative of the evolved damage [d(D, t)]. If this time derivative is positive the damage calculation will continue otherwise the damage calculation will stop and the previous time step damage value will be considered in the following time step calculation.

We used “the effect of the internal memory” of COMSQL to save and retrieve the damage value.

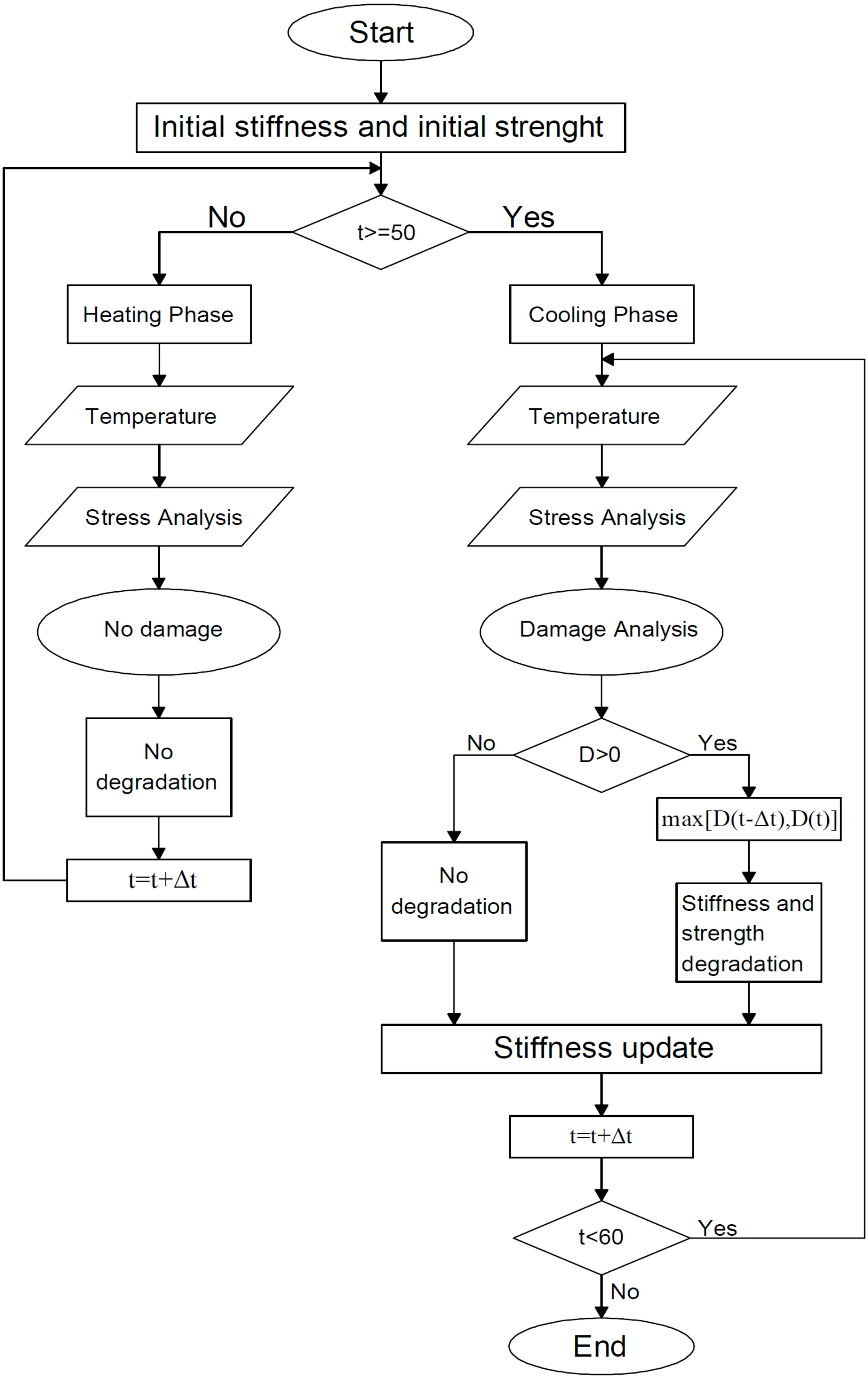

Figure 4.1: Flowchart of the followed algorithm to calculate the damage

4.3 Analysis of the first cycle of the heating/cooling process:

4.3.1 The application model:

Figure 4.2 illustrates the 2D axisymmetric model with the initial and boundary conditions. Analyses are conducted on the granite material. Table 4.1 summarizes the mechanical and thermal properties used in the analysis.

Table 4.1: Thermal and mechanical properties of the Granite

Material properties	**Density**	**Thermal conductivity**	**Specific heat**	**Thermal expansion coeff**	**Young Modulus**	**Poisson ratio**
	Kg/m^3	W/m.K	J/kg.K	1/K	GPa	
Granite	2600	1.8	930	$7*10^{-6}$	60	0.25

The damage evolution was limited to the mechanical properties represented by Young's Modulus. No damage was considered into the thermal neither into the physical properties of the rock material. Concerning the thermal treatment: heating period of 50 seconds, initial power intensity of 0.15 MW/m^2, heat exchange coefficient 14000 $W/m^2.K$, coolant temperature 40 °C were considered in the model.

The tensile strength of the granite was taken as 10 (MPa) at the ambient temperature. The crack damage initiation threshold was inductively extracted from the work of (Hommand-Etienne and Hourpert, 1989). This value was taken as 30% of the tensile strength of the rock material where this proposition as well agrees with the results of (Eberhardt, 1998) (Vasconcelos and Lourenço, 2008).

Free triangular mesh was used in the model. The mesh was extra fine under the treated surface and got coarser towards the extremities of the sample. The time stepping was selected by the use of backward differentiation formula (BDF). The time interval used to store the solution was selected to be 1.0 second in the heating phase and 0.2 second in the cooling phase to optimize the calculation time.

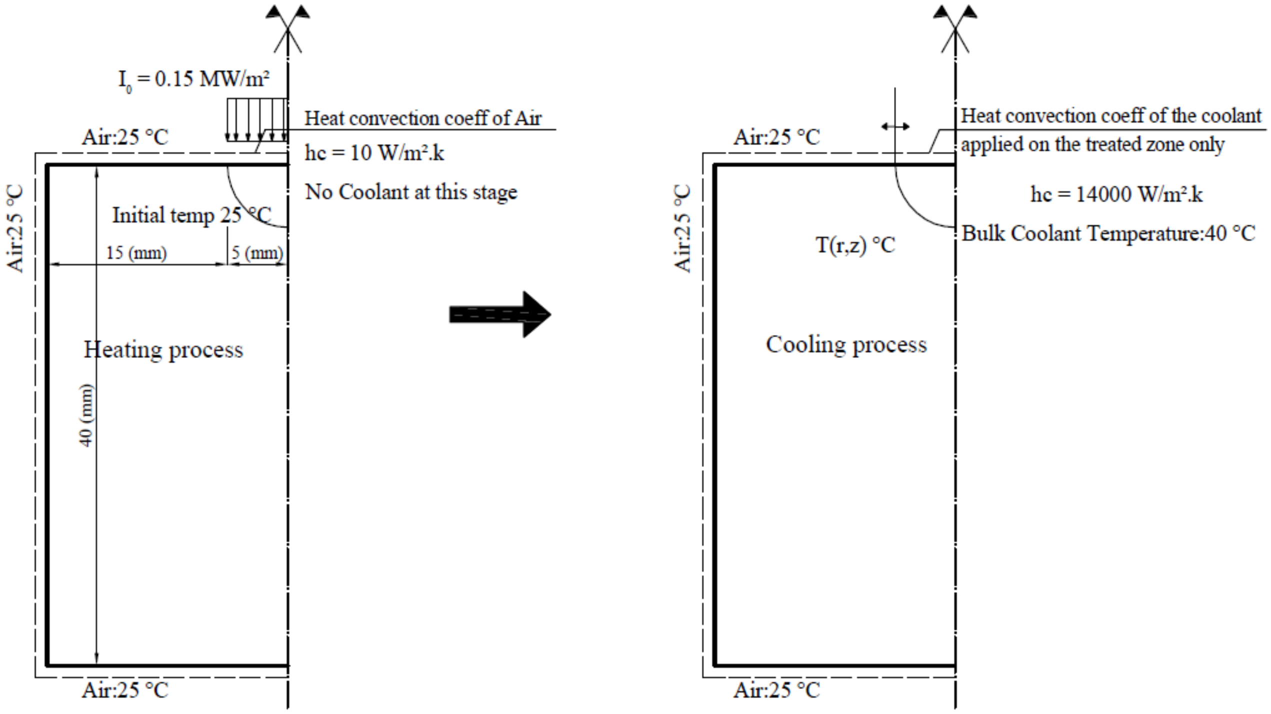

Figure 4.2: The 2D axisymmetric model and the initial and boundary conditions

4.3.2 Results:

Figure 4.3 shows the evolution of the damage variable during the heating/cooling cycle at the surface of the treated area. As expected, the heating phase does not induce damage. The latter is induced during the cooling process. The damage variable increases rapidly during cooling. It attains about 0.6 after one second of cooling and 0.98 after 4 seconds. We observe that the rock material at in the treated area is totally damaged after 4 seconds of cooling.

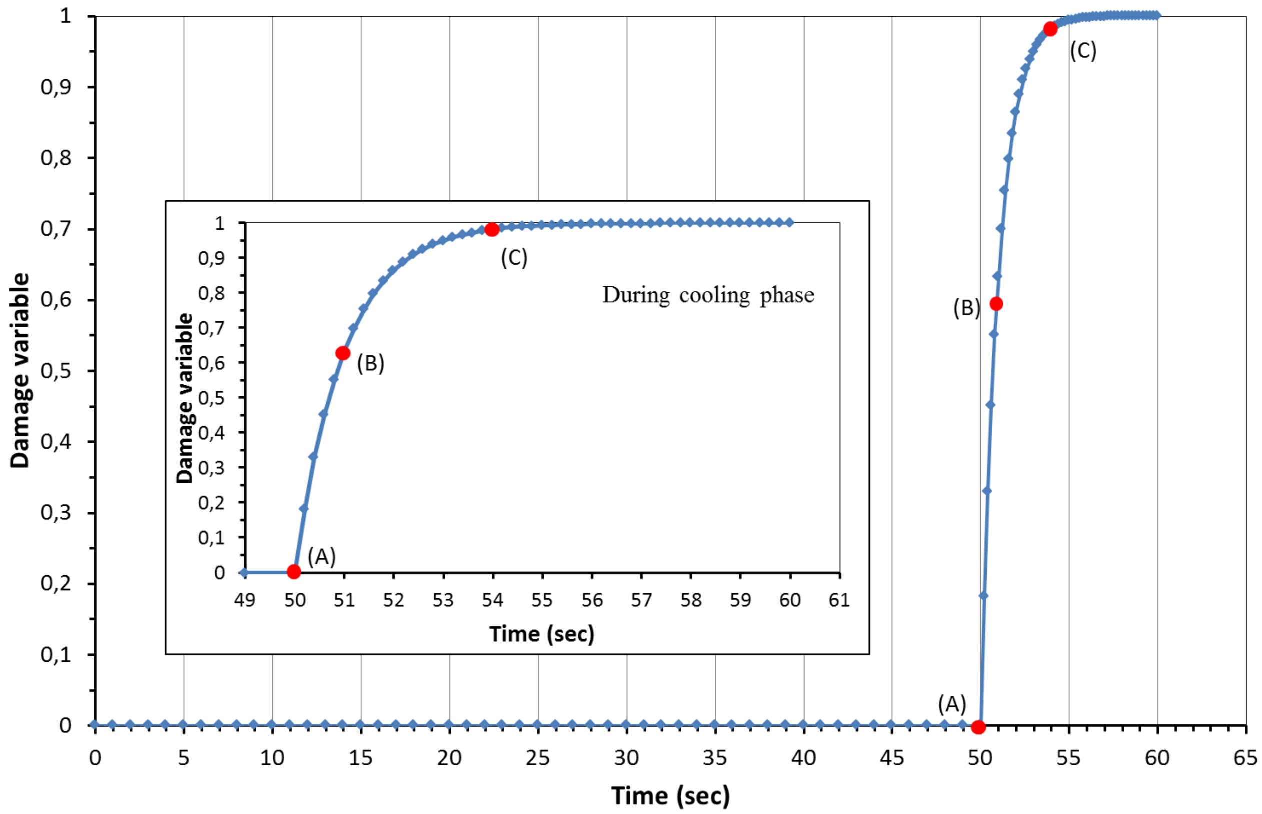

Figure 4.3: Damage variable variation over the time of treatment, Subfigure: damage variation during cooling phase

Figure 4.4 shows the variation of the radial stress at the treated surface during the heating/cooling process after damage evolution (b) and its comparison with the results obtained in the previous chapter (without considering the rock damage) (a). The degradation in radial stress is evident over the treated spot where the value of the stress approaches the zero at the end of cooling period.

The damaged spot size is close to that predicted in the previous chapter (6 mm in radius). This size measures after the adoption of the damage constitutive law 5.5 mm. The value of the radial stress dropped sharply after four seconds of cooling. At the beginning of the cooling phase, the radial stress didn’t decrease significantly until a very high level of damage. This matter is related to the size of the finite element in the model as well as the choice of the damage law itself (Ozbolt and

Ananiev, 2007). As the finite element size gets finer, the material behavior shows more plastic behavior than brittle one.

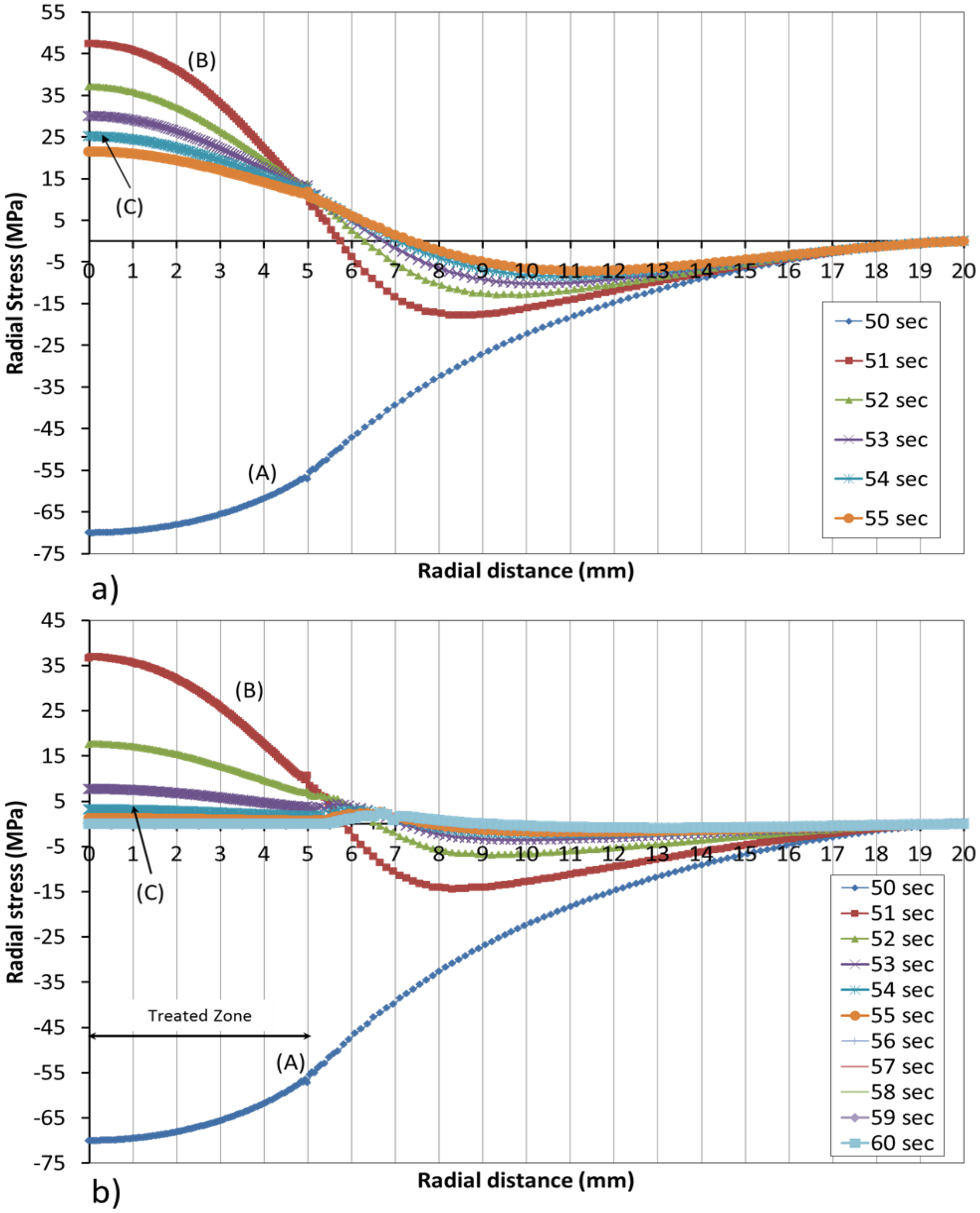

Figure 4.4: Radial stress variation at the treated surface: a) without damage, b) with damage during different moments of cooling process

Same behavior can be observed in the variation of tangential stress over the treated surface (Figure 4.5). The damage influence on the adjacent areas around the treated zone is more pronounced through the tangential stress than in the radial one. As well, the damage occurred in the non-treated zones where the tangential stress decreased significantly.

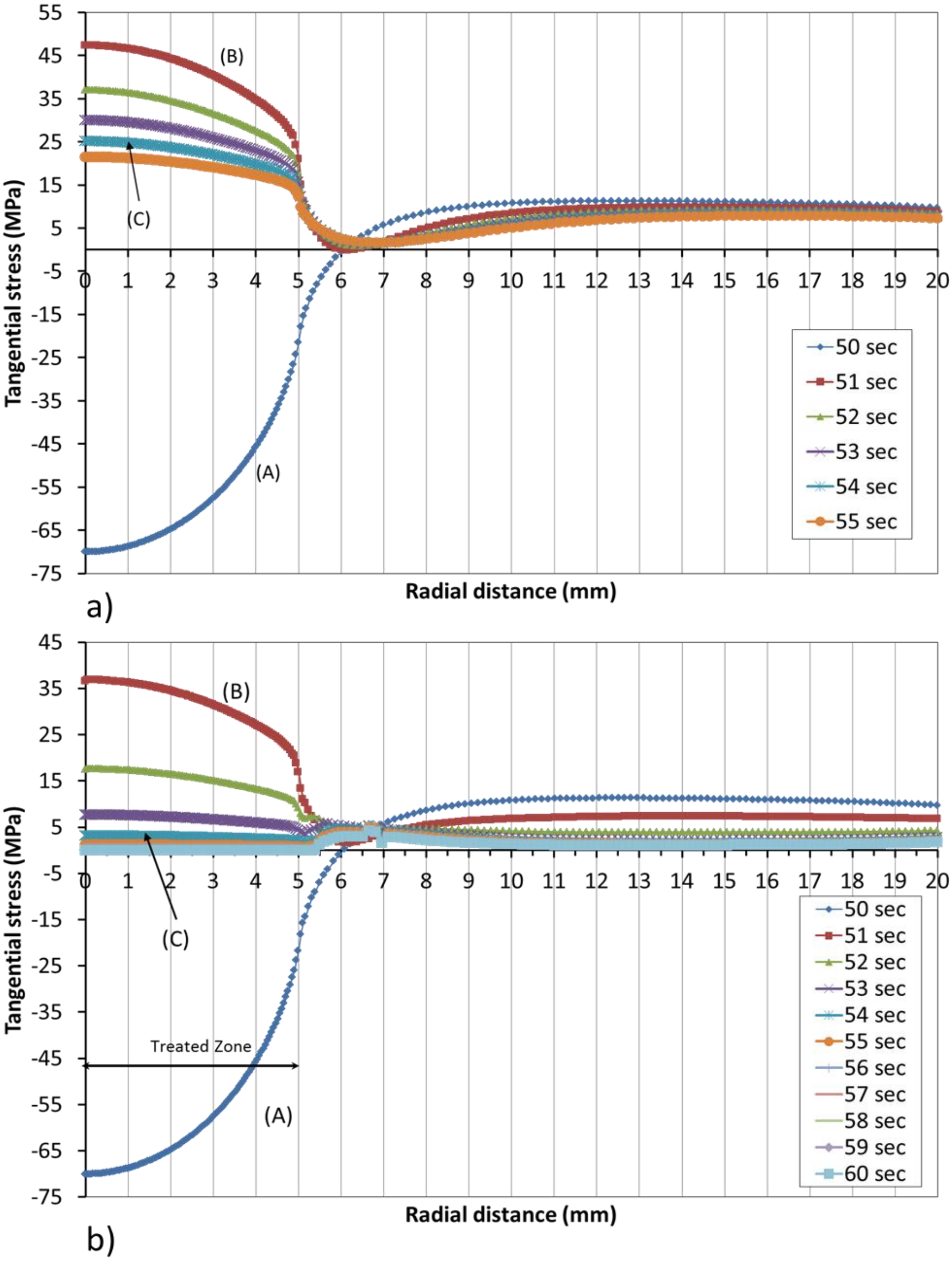

Figure 4.5: Tangential stress variation at the treated surface during different moments of cooling process

Figure 4.6 shows the evolution of the damage variable at different depths of the sample axis. At depth of 1 mm, we observe an evolution of the damage variable similar to that at the sample layer, but with a delay of about 3 sec, which is due to the delay of the heat transfer in the sample. At this depth, the damage variable reaches 1 after 8 seconds. At depth = 1.1 mm, we observe an attenuation of the damage variable evolution. The damage variable increases at a lower rate than that at the sample surface with a maximum value of 0.8 after 8 seconds. At a depth of 1.5 mm, the damage variable undergoes small increase with a maximum value of about 0.2 mm.

The damage decreases with depth because of the weak thermal rock diffusivity that has negative role in delivering the cooling effect to the deepest layers. In addition, the coolant temperature doesn't stay as at the start of cooling phase so that the coolant loses his ability to extract more energy from preheated rock material.

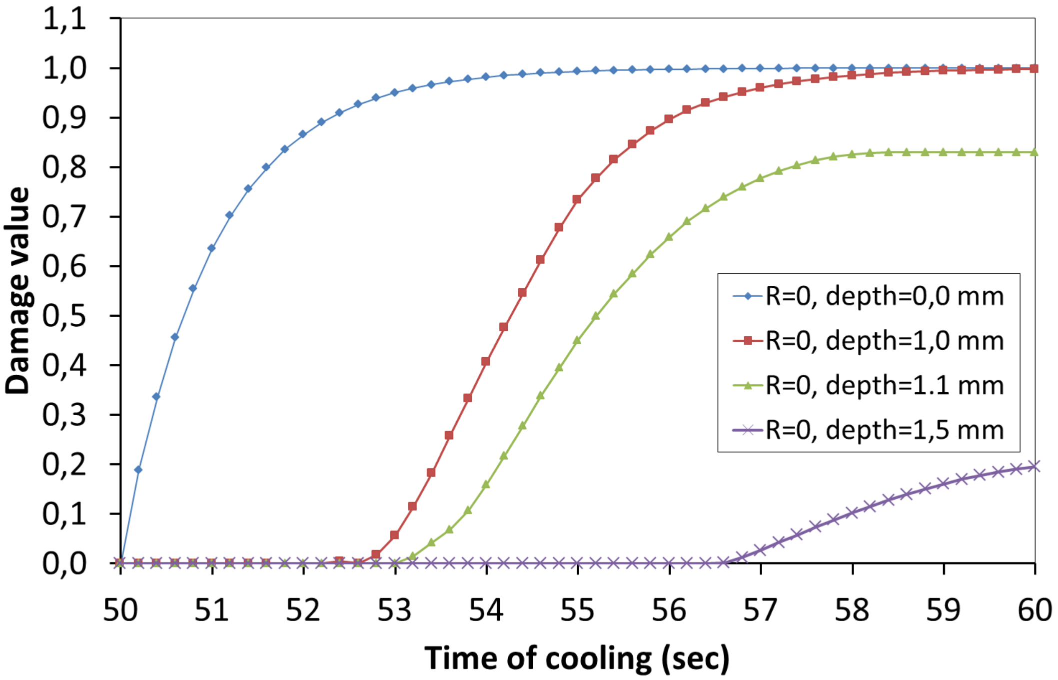

Figure 4.6: damage evolution in the subsurface layers beneath the treated spot

Figure 4.7 shows the evolution of the damage in the axis of the simple during the heating/cooling process.

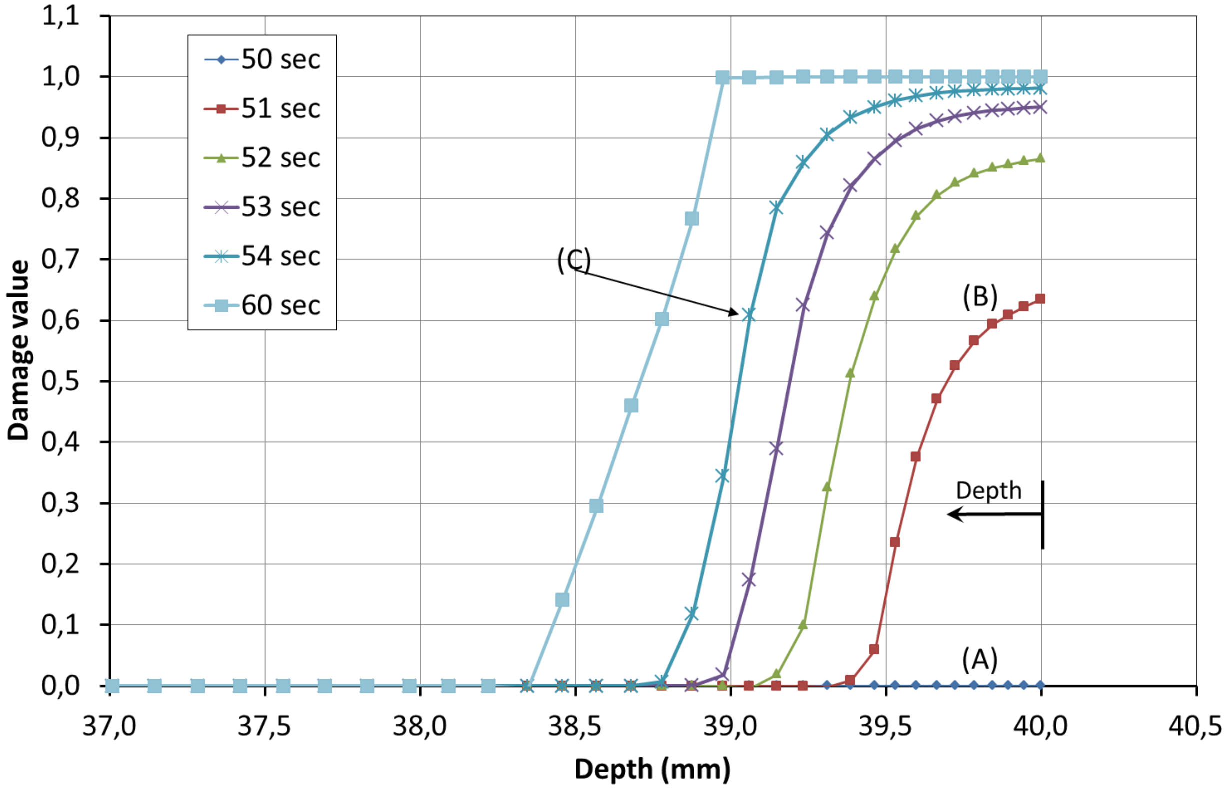

Figure 4.7: Damage evolution beneath the treated surface (centroid line)

We observe that damage variable increases rapidly near the treated surface and decreases sharply to zero at depth higher than 1.65 mm. After ten seconds of cooling, the rock is totally damaged in a layer 1 mm in thickness below the treated area (damage variable = 1).

Figure 4.8 shows the variation of the depth of the damaged layer during the cooling phase under the center of the treated spot. We observe a rapid increase in this depth during the 5 first seconds (it attains 1.5 mm), followed by a lower rate increase up to 8 seconds (depth = 1.6 mm) and then stabilization at 1.65 mm.

Comparing to the penetration depth predicted in the previous chapter, the penetration depth after adopting the damage law is increased by approximately 20% of its values to step up from ~1.4 mm to ~1.65 mm.

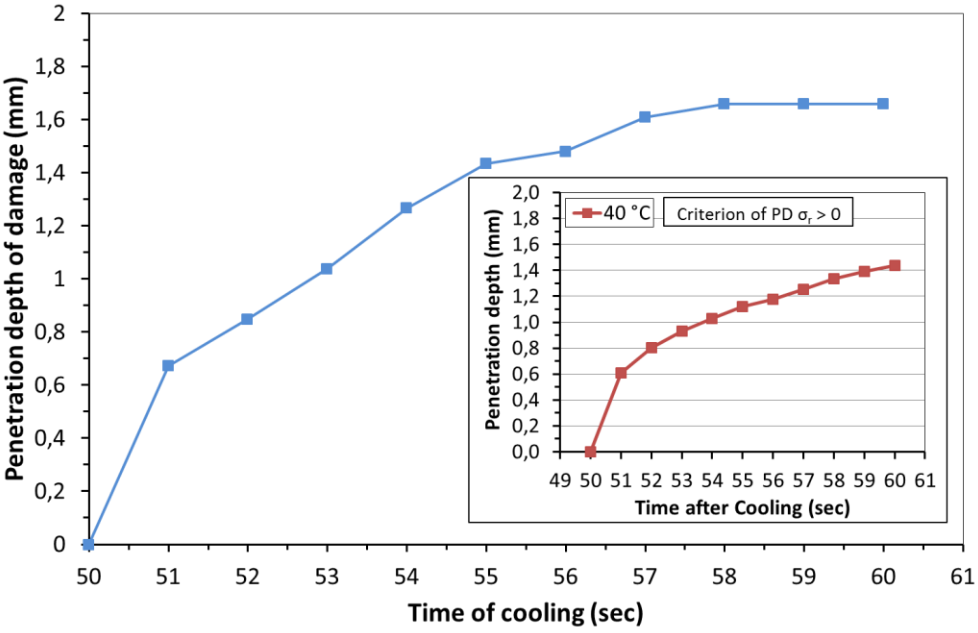

Figure 4.8: Penetration depth of damage under the treated zone

Figure 4.9 shows the variation of the Young’s Modulus during the cooling process.

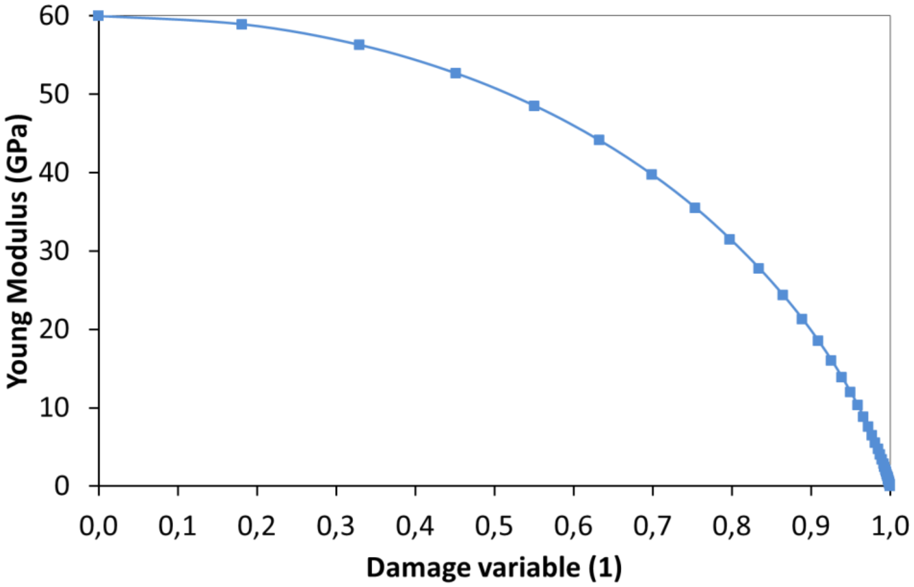

Figure 4.9: Young ‘modulus degradation with the damage variable

Figure 4.10 shows the lentil, which is removed from the rock sample by the thermal process (totally damaged). This lentil could be approximated by a disk 1 mm in depth and 5 mm in radius (the radius of the treated surface). This lenticular shape of the removed material eliminates the tapering problem associated to thermal rock removal by laser technique (Olaleye B, 2010) (Xu et al., 2004) where the formed hole in the sample takes the shape of the laser beam (Gaussian for example) (Xu et al., 2005).

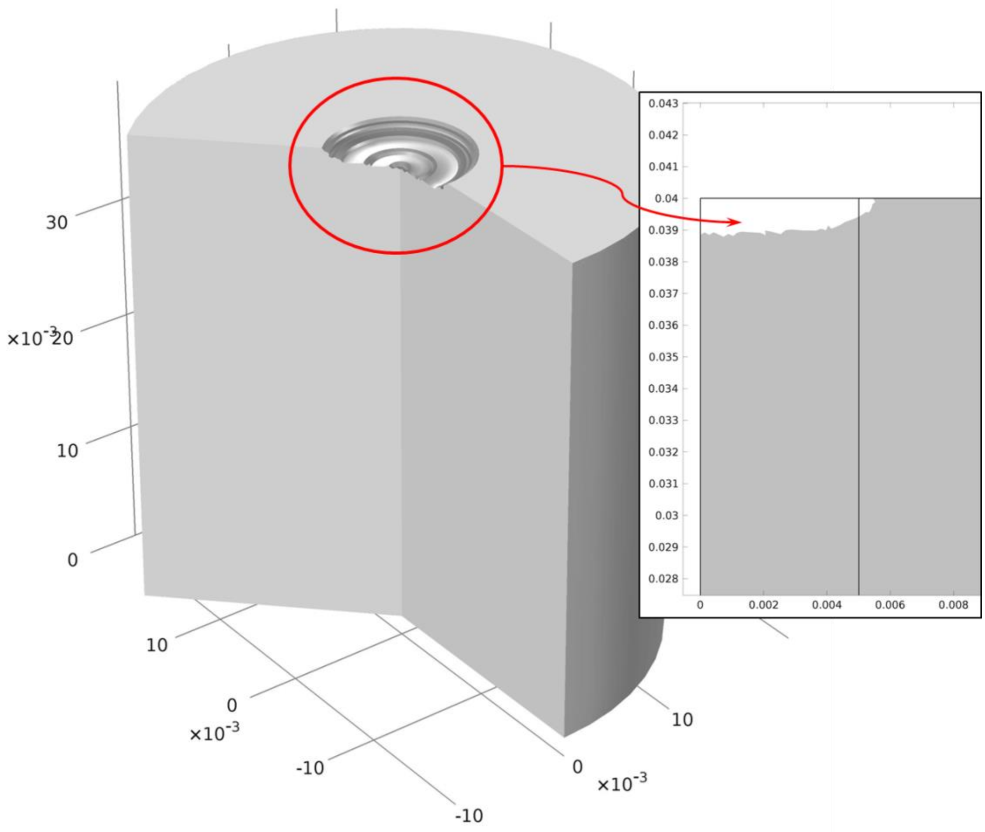

Figure 4.10: The estimated removed rock material after the thermal treatment during the first cycle

Figure 4.11 shows the influence of the temperature of the coolant on the variation of the damage penetration (thickness of the damaged zone). For a coolant temperature = 100°C, we observe a stabilization of the penetration damage after 1 second at 0.5 mm. For a coolant temperature = 60°C, stabilization occurs after 5 seconds at a penetration depth of 1.1 mm. For a coolant temperature = 40° C, stabilization occurs after 7 seconds at penetration of 1.6 mm. This result shows an important increase in the damage penetration with the reduction of the coolant temperature.

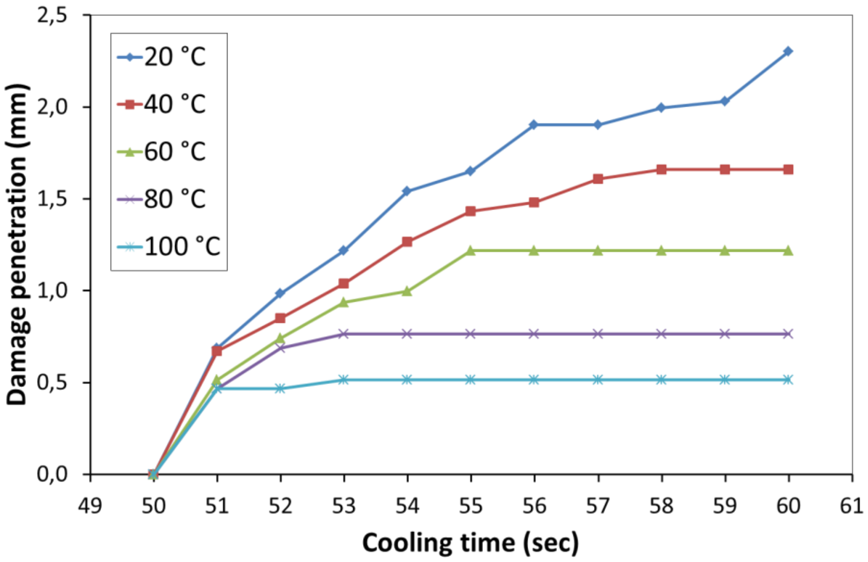

Figure 4.11: Variation of the damage penetration depth with different coolant temperatures

4.4 Analysis of the second cycle of the heating/cooling process

4.4.1 Numerical modeling

The second cycle of the thermal treatment starts after the end of cooling phase of the first cycle. Analysis is conducted on a modified geometry of the sample (Figure 4.12), because of the remove of the zone damaged during the first cycle. The state of the sample (temperature, stresses, damage, Young's modulus) at the end of the first cycle is considered as an initial condition in the analysis of the second cycle. These initial conditions were recalled through (.txt) file format which relates the variables values by the coordinates of the mesh elements. The quality of the retrieved data is auto-controlled by Comsol according to these notions: coarser, fine, extra fine. The latter was used. Relatively, difference between the final state due to first cycle and the initial conditions for the second cycle was observed (5%).

The heating period was reduced in comparison with the 1st cycle, because of the energy stored in the sample during the first cycle. Potentially, reaching the same temperature difference between the maximum temperature and the coolant temperature is required to get the same penetration depth as in the first cycle. So to determine this appropriate heating period in the second cycle, we divided the heating period into sections each for 25 seconds. Two intervals were obtained the first [0, 25] seconds and the second is [25, 50] seconds. Then after, the calculation was conducted for the mean values of each interval. The maximum temperature and the penetration depth in each step were retrieved and compared with those in the first cycle. Then each interval was divided into two new intervals and the calculation was again conducted for the mean values and so on. The process was repeated until the convergence between the maximum temperature and the penetration depth in the first cycle was obtained.

The optimal heating period corresponding to the conditions at the end of the first cycle was determined as 25 seconds. This optimal heating period can be reduced if the power intensity is increased. The cooling period was fixed to 10 seconds as in the first cycle.

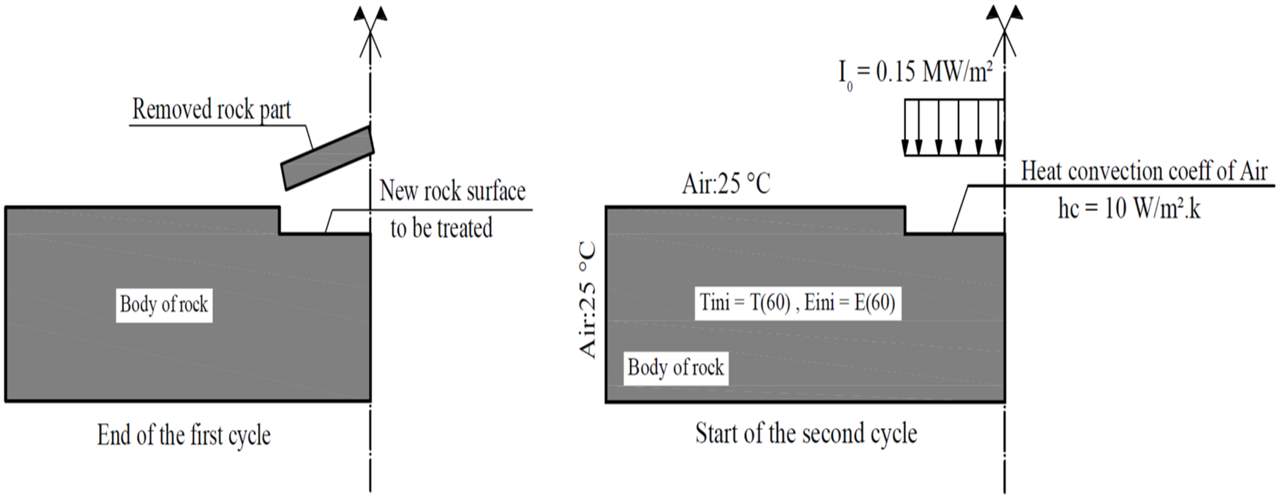

Figure 4.12: Scheme of the adopted geometry for the second cycle analysis

4.4.2 Results

Figure 4.13 shows the temperature variation during the heating/cooling treatment at the surface of the treated area. Compared to the first cycle, the heating period is reduced by a half. Which means that the energy used in the second cycle is equal to 50% of that used in the first cycle. We observe that the temperature profile in the second cycle is similar to that of the first cycle. We observe a rapid increase in the temperature, which attains 325°C is reached in 25 seconds. The variation of the temperature during the cooling phase is similar to that of the first cycle.

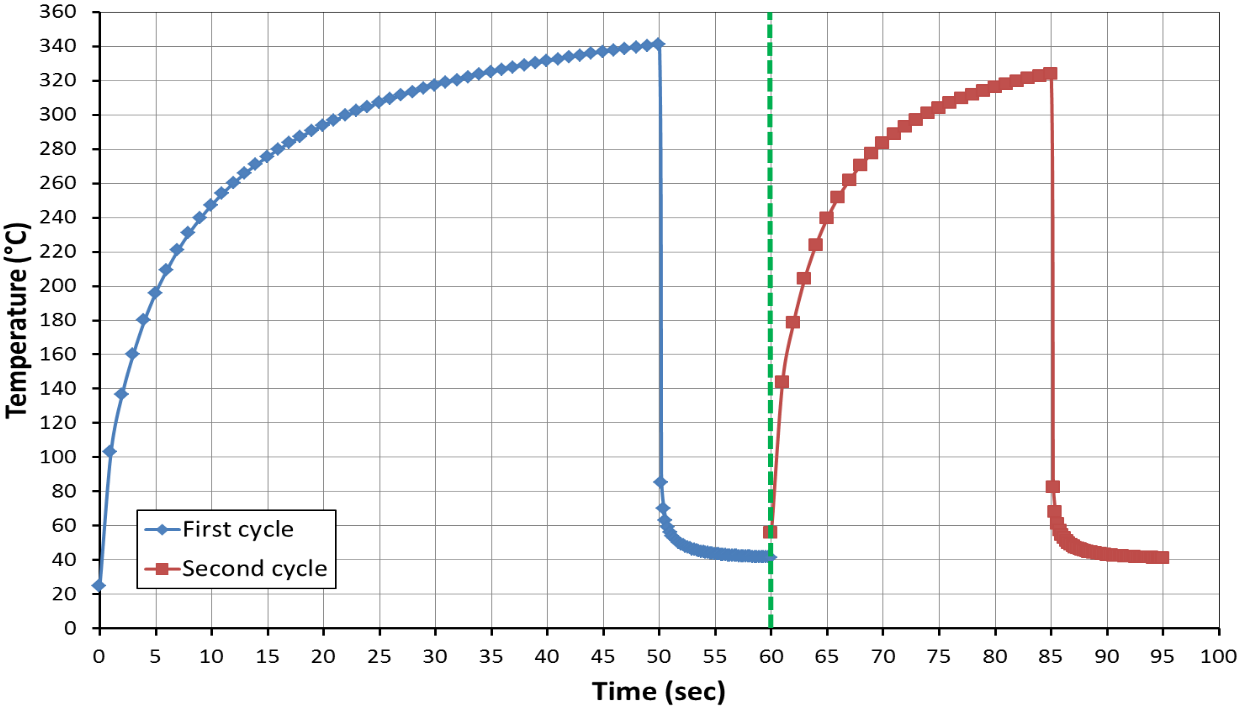

Figure 4.13: Temperature profile during the cyclic application of the thermal treatment

Figure 4.14 shows the variation of the damage variable at different depths in the sample axis and its comparison with results obtained during the first cycle. At the treated surface, the damage variable attained the value of 1.0 directly after cooling. At depth 0.5 mm, the damage started to evolve after one second of cooling and reached the value 1.0 after 6.0 seconds after cooling. At depth 1.0 mm, the damage evolved after 3.0 seconds and reached the maximum value (0.95) after 7.0 seconds of cooling. At depth 1.1 mm, the damage value recorded 0.75 that is lower than what is recorded in the first cycle at the same depth.

Comparing to the first cycle, the damage evolved in identical manner at the treated surface as well as at the deeper depths. The totally damaged rock material thickness in the second cycle was slightly smaller than what was removed in the first one (5%).

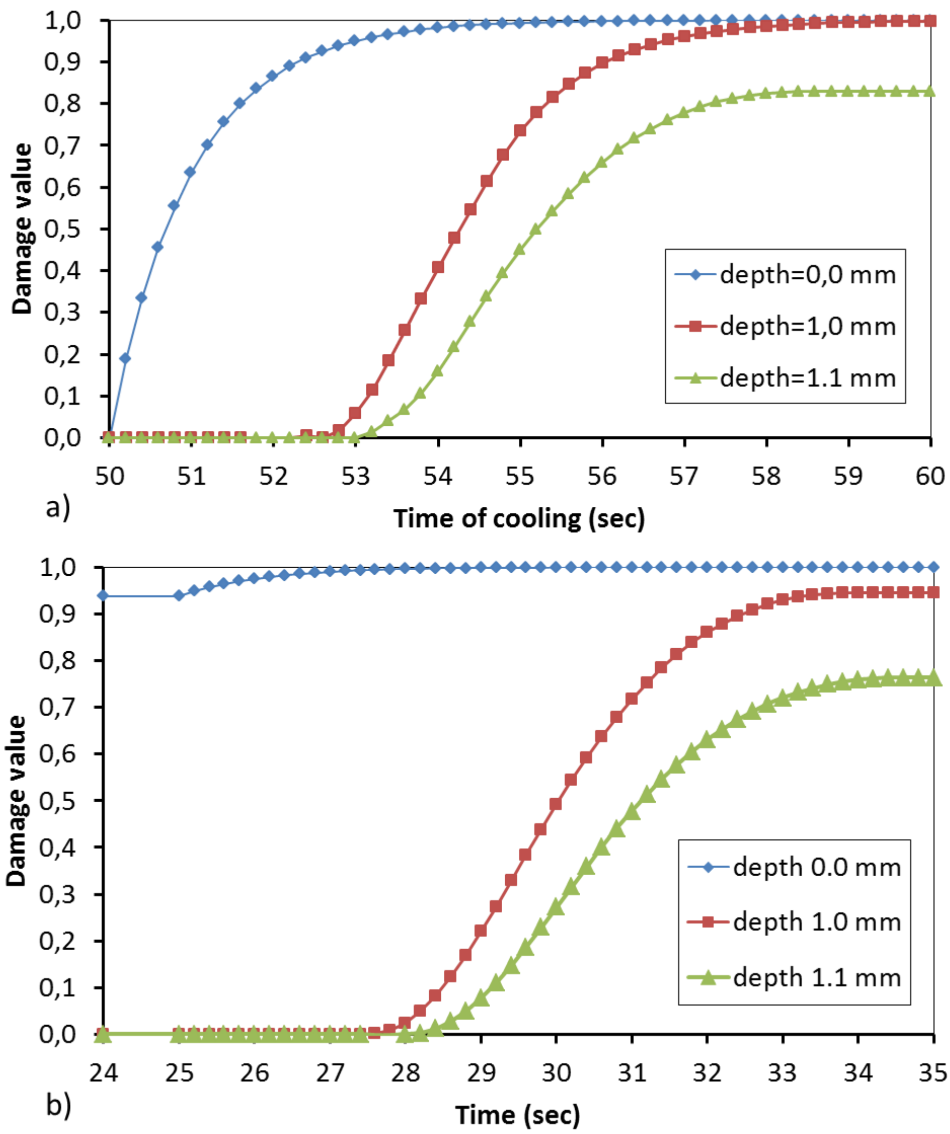

Figure 4.14: damage variation with process time at different levels under the treated surface: a) first cycle, b) second cycle

Figure 4.15 shows the variation of the damage penetration and its comparison with results obtained during the first cycle. We observe that the maximum attained penetration depth is about 1.65 mm which is equal to what has been achieved in the first cycle. A layer of 0.95 mm thickness is completely damaged at the end of the second cycle.

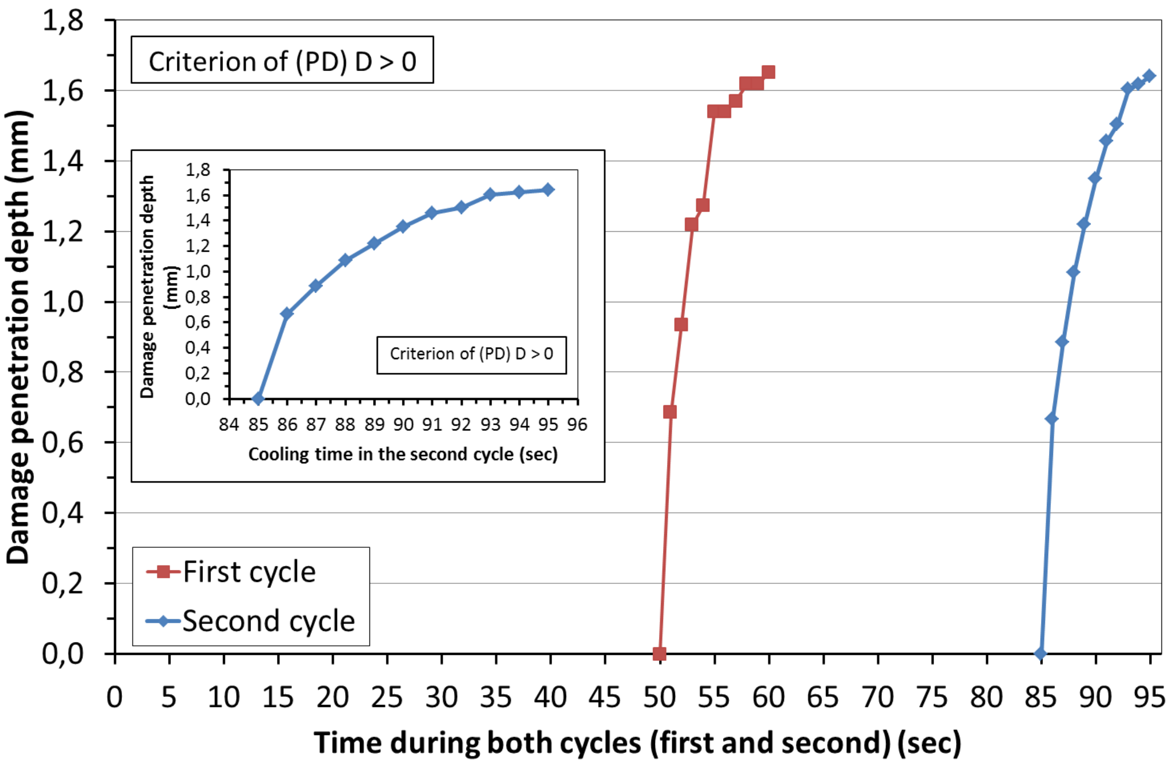

Figure 4.15: Damage evolution during the first and second cycles

Likewise, at the end of the second cycle another cylinder of dimensions of 10.0 mm in diameter and 0.95 mm in depth was completely removed. Consequently, the created hole within the sample counts 10.0 mm in diameter and 1.95 mm in depth.

Comparing to the hole perforated by laser that measures 3.4 mm in diameter and 5.8 in depth with energy supply equal to 2.75 kW (Ahmadi et al., 2011), the proposed mechanism succeeds to remove more significant quantity of rock material by use more less energy supply.

Whilst the reported damage by heating approached 0.12 due to 550 °C at the treated surface (Walsh et al., 2011), a complete damage of the rock material was predicted by the proposed heating/cooling process by the use of maximum treated surface temperature of 340 °C and sudden cooling process.

Concerning the penetration rate, it potentially attained a value of 0.02 mm/s in the granitic rocks. This penetration rate is relatively weak comparing to actual penetration rate recorded by the conventional mechanical techniques. This may be explained by that the penetration depth of cooling effect is proportional to the many factors as the thermal diffusivity of the rock material and the cooling period (Tarasovs and Chassemi, 2012).

The whole removed portion of the sample at the end of the second cycle is illustrated in (Figure 4.16).

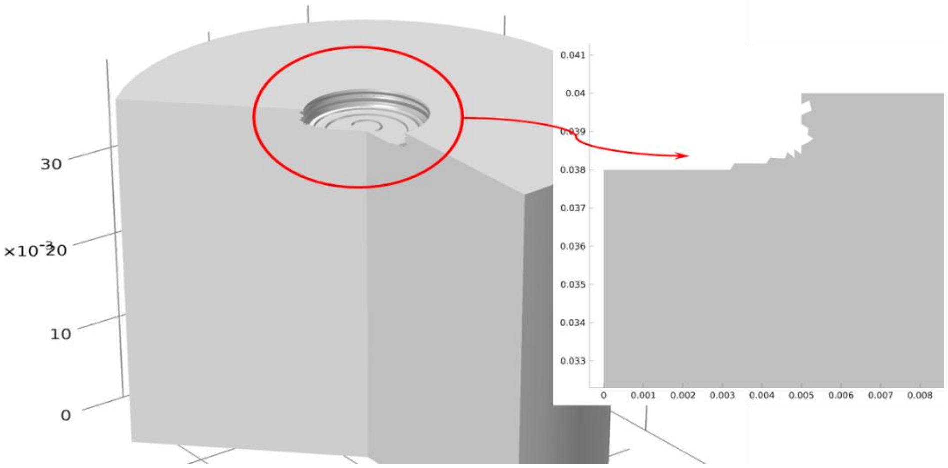

Figure 4.16: The removed rock material after the second cycle

4.5 Conclusion

This chapter included the consideration of rock material damage in the analysis of the heating/cooling process. Constitutive damage law was implemented in 2D axisymmetric finite element environment. The damage was supposed to occur in the cooling phase, which generated tensional stresses.

The cyclic nature of the proposed process was analyzed.. In the first cycle, damage occurred in the sub-layers near the treated surface. The damage penetration reached 1.65 mm. A layer with 1.0 mm of depth was completely damaged by tension.

In the second cycle, the heating period was reduced by a half with regard to the first cycle: It took 25 seconds using 0.15 MW/m² power intensity and 40 °C of coolant temperature. The penetration depth at the end of the second cycle was approximately similar to that achieved in the first cycle (1.65 mm). The completely damaged layer was 0.95 mm in depth.

The penetration rate is estimated to 0.02 mm/s in the granitic rock. However, this penetration rate was determined using strong simplifications. The incorporation of these simplifications in the fracture and penetration process should be verified using experimental works or (and) additional numerical analyses.

CHAPTER 5

THERMAL LABORATORY STUDY OF THE HEATING-COOLING FRACTURE PROCESS IN ROCK MATERIAL

5.1 Introduction:

This chapter presents a laboratory study of the thermal phenomena, which occurs during rock fracturing using heating-cooling process. The chapter describes first the experimental setup used in this study with a particular focus on difficulties encountered in the use of a thermal source as well as in monitoring the thermal parameters. Tests were conducted in two phases: the heating phase and the cooling phase. The latter was conducted using water at either 20 ° C or at 100 °C. The influence of the coolant temperature will be analyzed. The experimental results were compared to the numerical modeling presented in the 3rd chapter.

5.2 Description of the experimental setup and procedure

Figure 5.1 shows the experimental setup used in this study. It includes a heating/cooling dispositive and a monitoring system to follow the temperature variation in the rock sample during the heating/cooling process.

5.2.1 Heating/cooling dispositive

A heat gun was used as a heating source. It produces a hot air flow on the surface of the rock sample. Compared to the microwaves radiation heating, this process is slow. Consequently, it leads to heating the adjacent non-treated zones. In this case the heating mechanism occurs by convection. Tests were conducted using the hot air gun brand Metabo HE 23-650, whose power is equal to 2300 Watts. The air speed varies between 150 to 500 l/min. The temperature of the air at the nozzle open varies between 50 and 650 C°. The air temperature can be regulated with interval of 50 °C. The hot air can be concentrated over a circle of 1 cm in diameter. The cooling phase was conducted by water pulverization on the surface of the rock sample either at 20 °C or at the boiling point (about 100 °C).

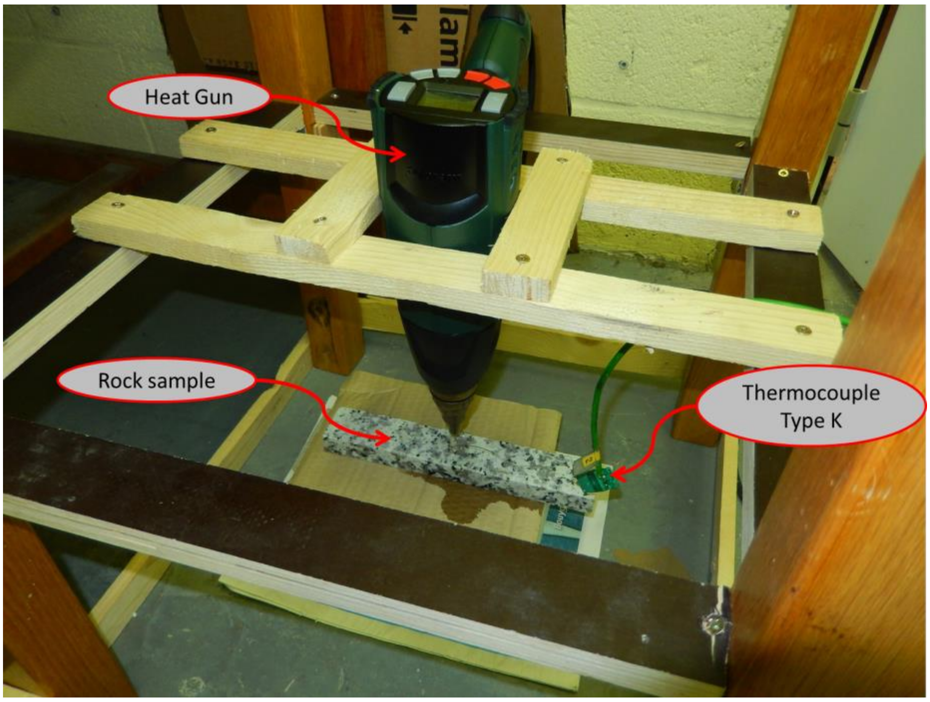

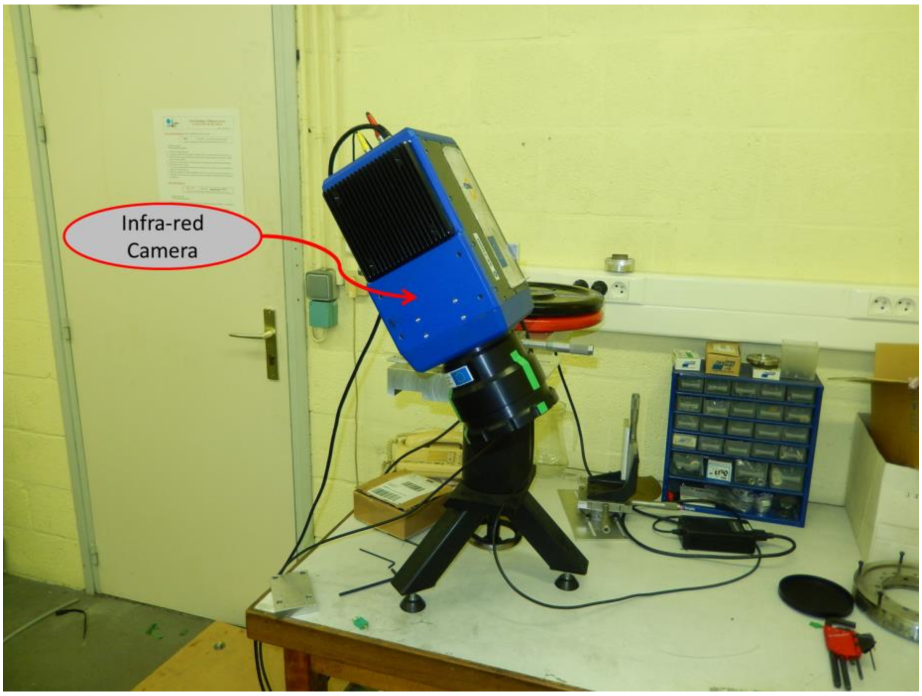

Figure 5.1: Experimental set up used in the study of the heating-cooling process in rock material

5.2.2 Thermal monitoring system

The temperature variation in the rock sample was followed using mineral-insulated Inconel 600 sheathed thermocouple. This thermocouple is 0.5 mm in diameter and 150 mm in length. Data was recorded at 0.01 sec time interval using the data recorder DN3100 V2.

The dispositive included also a thermography and infra-red camera, which is a "photon counting device". Depending on the amount of received photons, it returns an electrical voltage expressed in digital level (DL). The radiation source emits a photon flow, which is then captured by a receiver. The letter transforms the incident flux into electrical voltage, which is then converted to temperature using a calibration curve.

The matrix camera FLIR titanium SC7000 was used in this work. It uses InSb sensor and 640x512 pixels with optional waveband of 1.5-5 microns. It was calibrated in the temperature interval (-20°C - 3000°C). The integration time varies between 400 ns and 20 ms. The frame rate varies between 5 Hz to 96 Hz. An integration time of 60µs was selected for the short-term events.

The calibration process could be conducting using tow operating modes: simple calibration and complete calibration. The former consists in the determination of the camera's response to series of known reference temperatures point in the black body. The latter uses the same strategy, but in addition it considers the influence of the internal temperature of the camera on the measurements. The first mode was used in this work. In order to eliminate the effect of the camera internal temperature, the camera was turned on during four hours before conducting any test.

Each point in the calibration curve is characterized by two values the black body temperature and the digital level returned by the camera. The points were determined with a temperature interval of 25 °C of the black body temperature. In order to get these points, the black body temperature was raised to the required level and then the measurements of the camera were saved throughout 100 images. Thereafter the mean value of DL for these 100 images was calculated. Figure 5.2 shows the calibration setup. The calibration required about 5 hours. Image treatment was conducted to eliminate the bad pixels. Figure 5.3 shows an example of the calibration curve in the temperature interval (5- 70 °C).

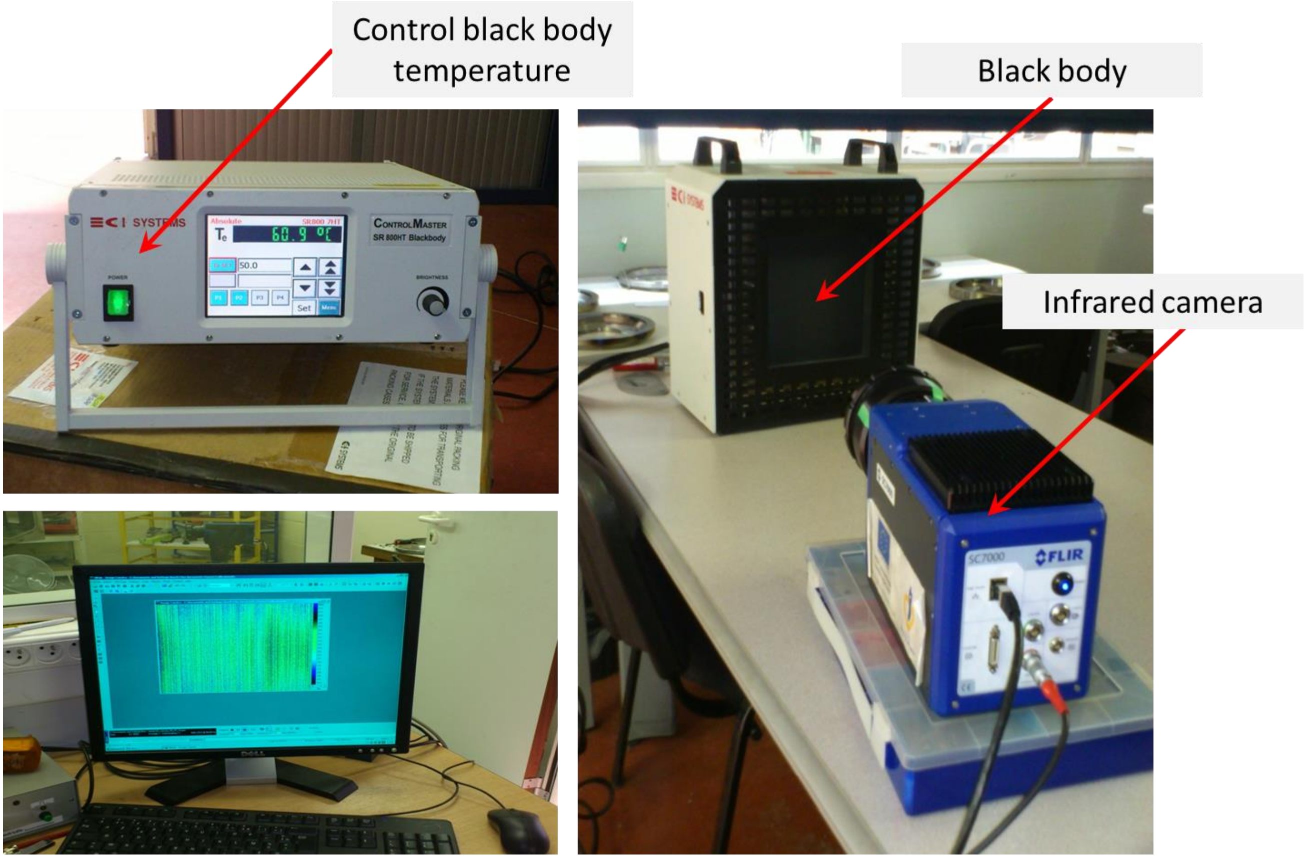

Figure 5.2: Camera calibration setup

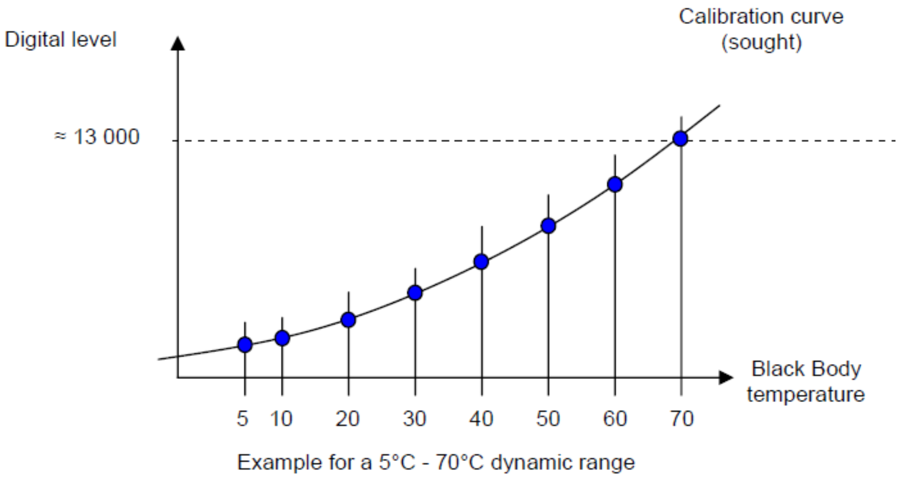

Figure 5.3: Camera calibration curve

5.2.3 Experimental protocol

Tests were conducted on granite samples, which were 250 mm in length, 40 mm in width and 20 mm in height. Thermocouples were fixed in holes 1 mm in diameter and 1mm in depth. They were not used in the treated spot, because of the difficulty of their fixation on the rock sample under high temperature condition. Figure 5.4 shows the scheme of the thermocouples installation.

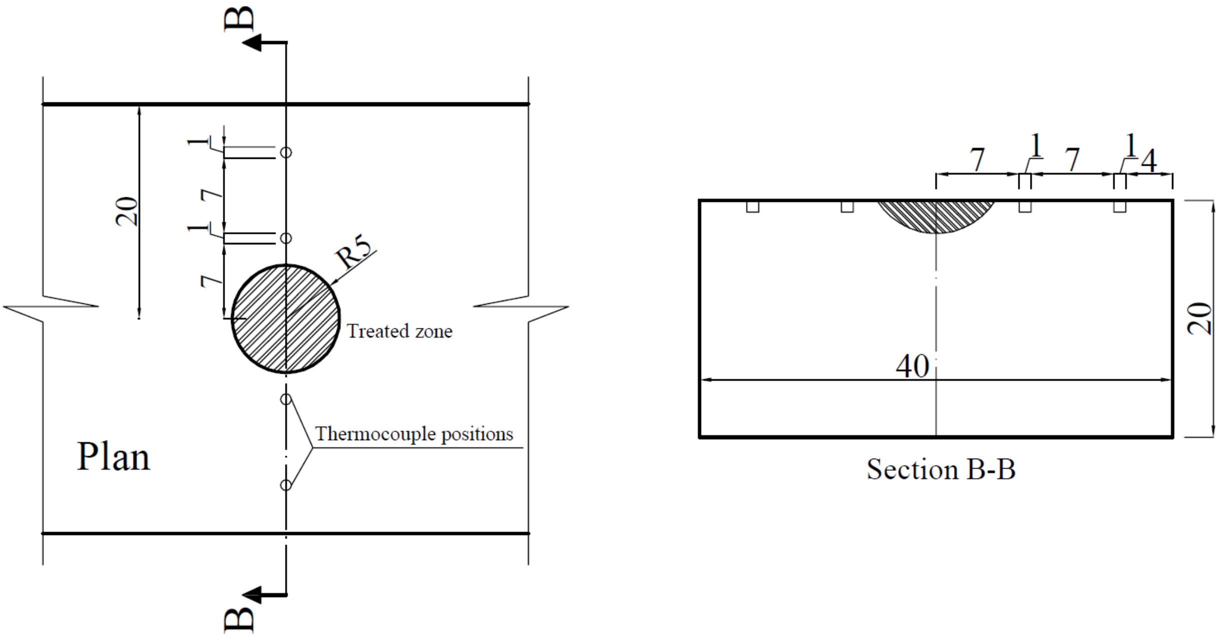

Figure 5.4: Scheme of thermocouples installation

Tests were conducted according to the following protocol:

- Fixation of the sample under the heat gun nozzle and adjusting the distance between the nozzle and the sample surface (Figure 5.5).
- Fixation of the thermocouple on the rock surface.
- Conduction of the heating phase.
- Conduction of the cooling phase using water pulverization.
- The evolution of the temperature was registered during the test.
- Five images per second were taken using the infrared camera. The data acquisition was conducted at 0.01 sec time interval.

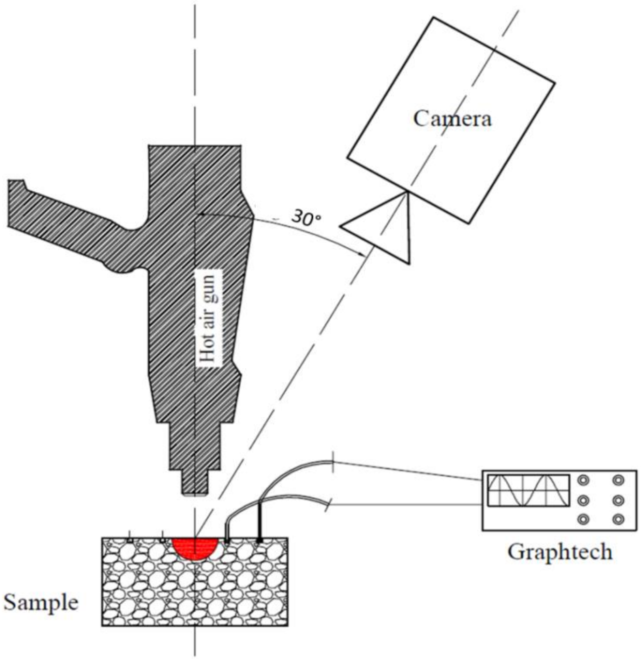

Figure 5.5: Experimental setup

5.3 Results and discussion

Tests were conducted on granite samples. The cooling phase was realized using water at either 20°C or near the water boiling temperature (100 °C).

5.3.1 Test with cooling water at 20 °C

Two tests were conducted using cooling water at 20 ° C. Below a presentation of the results of these tests as well as their comparison with the numerical modeling.

5.3.1.1 Thermocouple data

Figure 5.6 shows the temperature measured by the nearest thermocouple to the treated zone before and after smoothing process. It can be observed that the temperature increased from the rock temperature up to 50 °C and then it stabilized. This phase is related to the operation conditions of the heat gun. Then, the temperature increased rapidly to 250 °C, and then slowly to 290 °C. During the cooling phase, we observe first a rapid decrease in the temperature down to 100 °C followed by a slow decrease down to 60 °C.

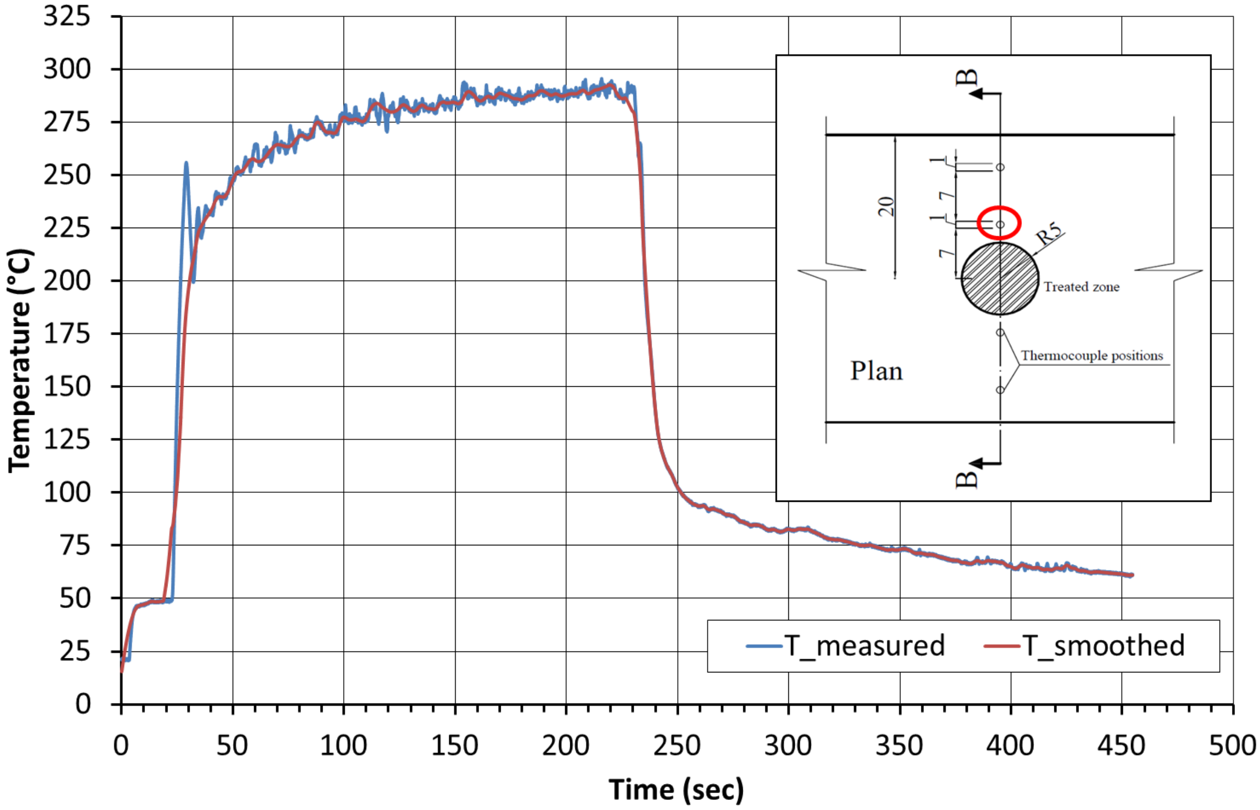

Figure 5.6: Temperature variation measured by the thermocouple (Test with water at 20 °C)

Figure 5.7 presents the temperature of the rock surface variation with time during the second test. At the beginning of the test once can notice that the thermocouple indicated a temperature about 100 °C because the second test was conducted directly after the first one without allowing the thermocouple to cool down. The maximum attained temperature for the rock surface was 286 °C.

During the cooling phase, the poured water reached the position of the nearest thermocouple to the treated zone. Likewise, the temperature dropped instantaneously to reach to 35 °C. This rapid drop of temperature by less than one second is related to the high heat exchange rate between the rock surface and the coolant. Thereafter, the temperature increased to attain water saturation point (100°C) during 20 sec and then decreased with time until the end of process to reach eventually 60 °C.

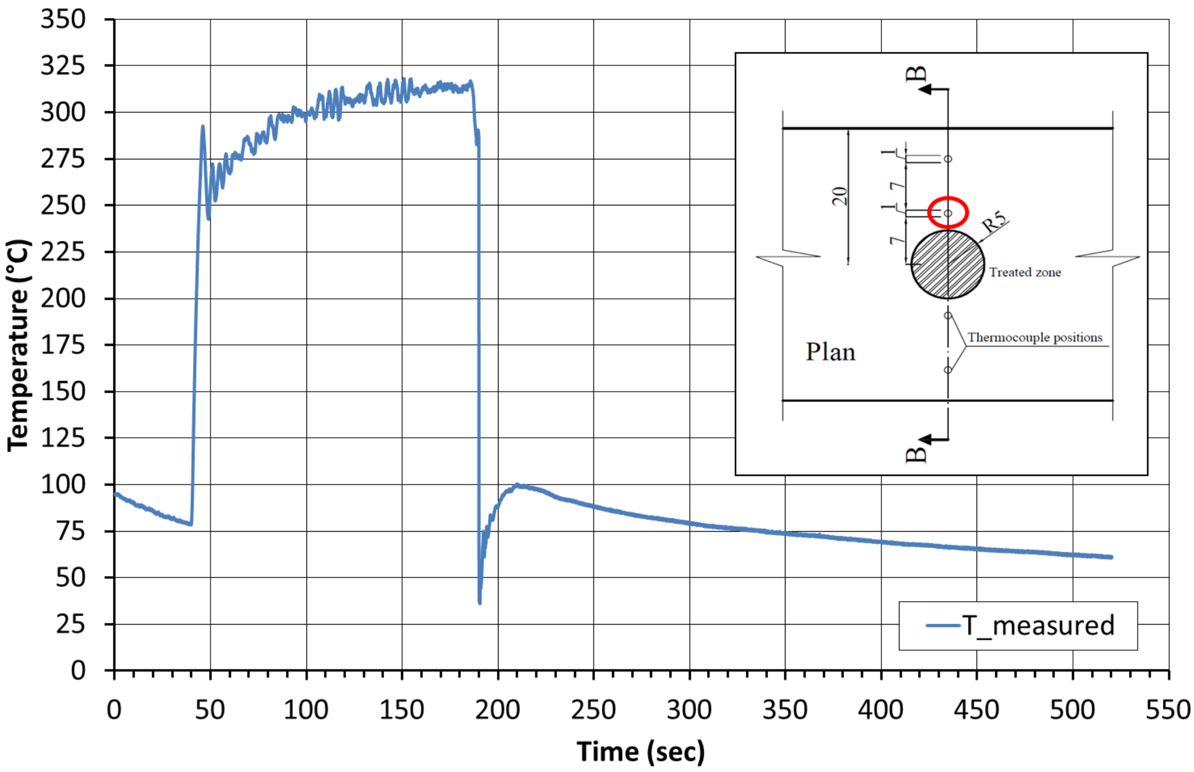

Figure 5.7: Temperature profile from the second sample cooled down with fresh water (~20 °C)

5.3.1.2 Thermography data

The use of the thermograph encountered the following difficulties:

- The high water absorption of the infrared radiation, consequently, during the cooling phase the camera cannot be used.
- The camera calibration was conducted in the temperature interval (50 - 500 °C), due to the black body temperature controller. During the experimental work we used integration time of 60 µs which leaded to the camera saturation, when the temperature reached 275 °C.

Figure 5.8 shows the thermal images at end of the heating phase. According to thermocouple readings, the temperature at the sample the surface reached 291 °C at the end of heating phase. The saturation of the camera occurred at 275 °C. Consequently, at the center of the treated zone where the temperature was higher than the saturation level, the thermal camera did not well capture the temperature. We replaced the pixels with DL values higher than 14000 by the mean value of DL in each image. This default appeared in the heat gun itself and even at the center of treated center just for very short time. Temperatures lower than 50 °C were also not well captured, because of the camera saturation.

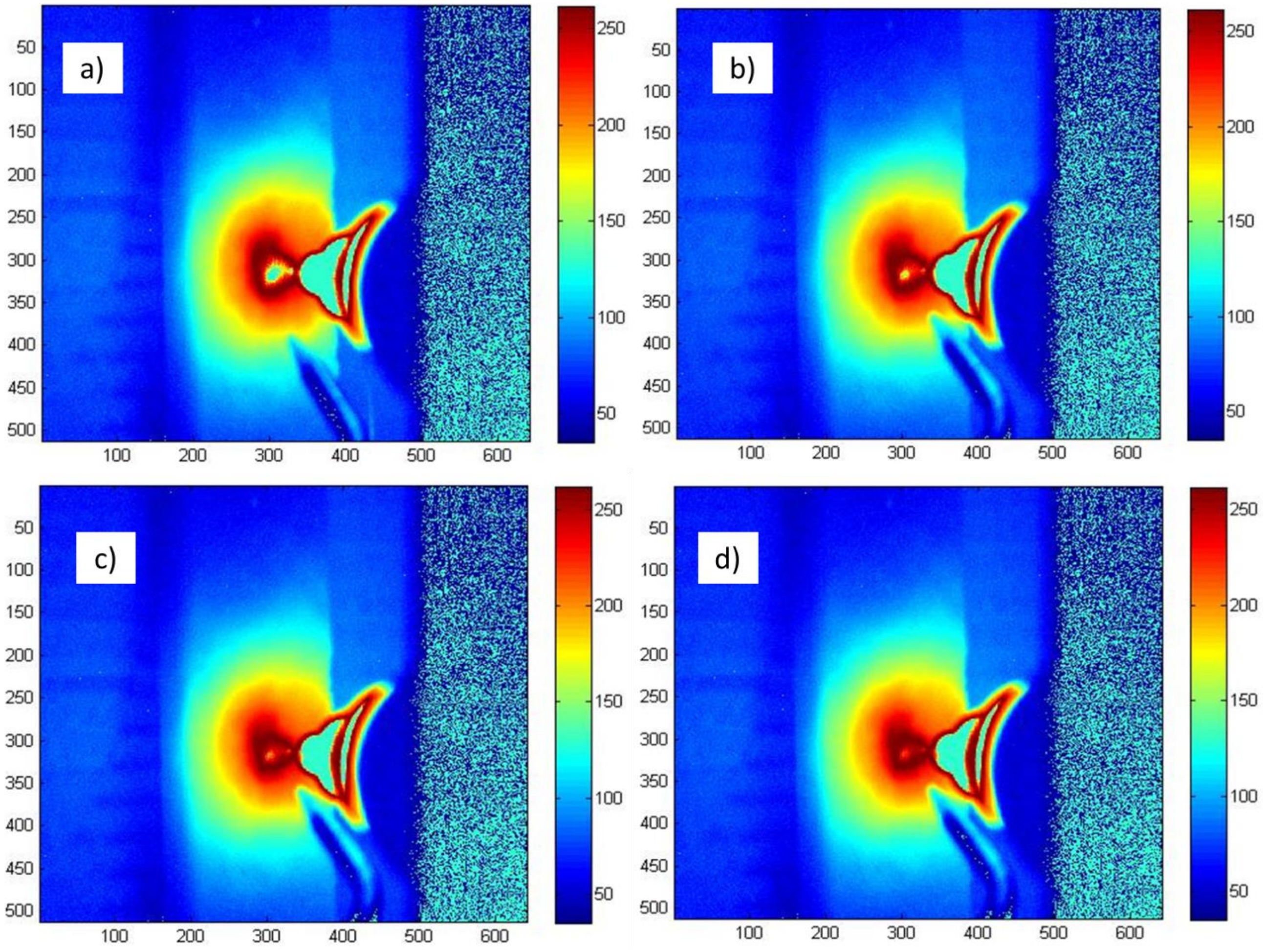

Figure 5.8: Temperature distribution on the rock surface during the last second of heating: a) and b): temperature distribution just before turning off the heat gun, c) and d) represent temperature distribution before water pulverization

Figure 5.9 shows the thermal images during the water pulverization (a, b) and after one second (c) and two seconds of cooling phase. We observe the presence of water in the treated zone, where the infrared radiation was totally absorbed. Consequently the measurement in this zone is related to that of the water. It was more efficient to use water spray to guarantee less water layer thickness and higher visibility for the thermal camera. As known the cooling by water spray can reach high heat exchange rate as the boiling one (Faghri and Zhang, 2006).

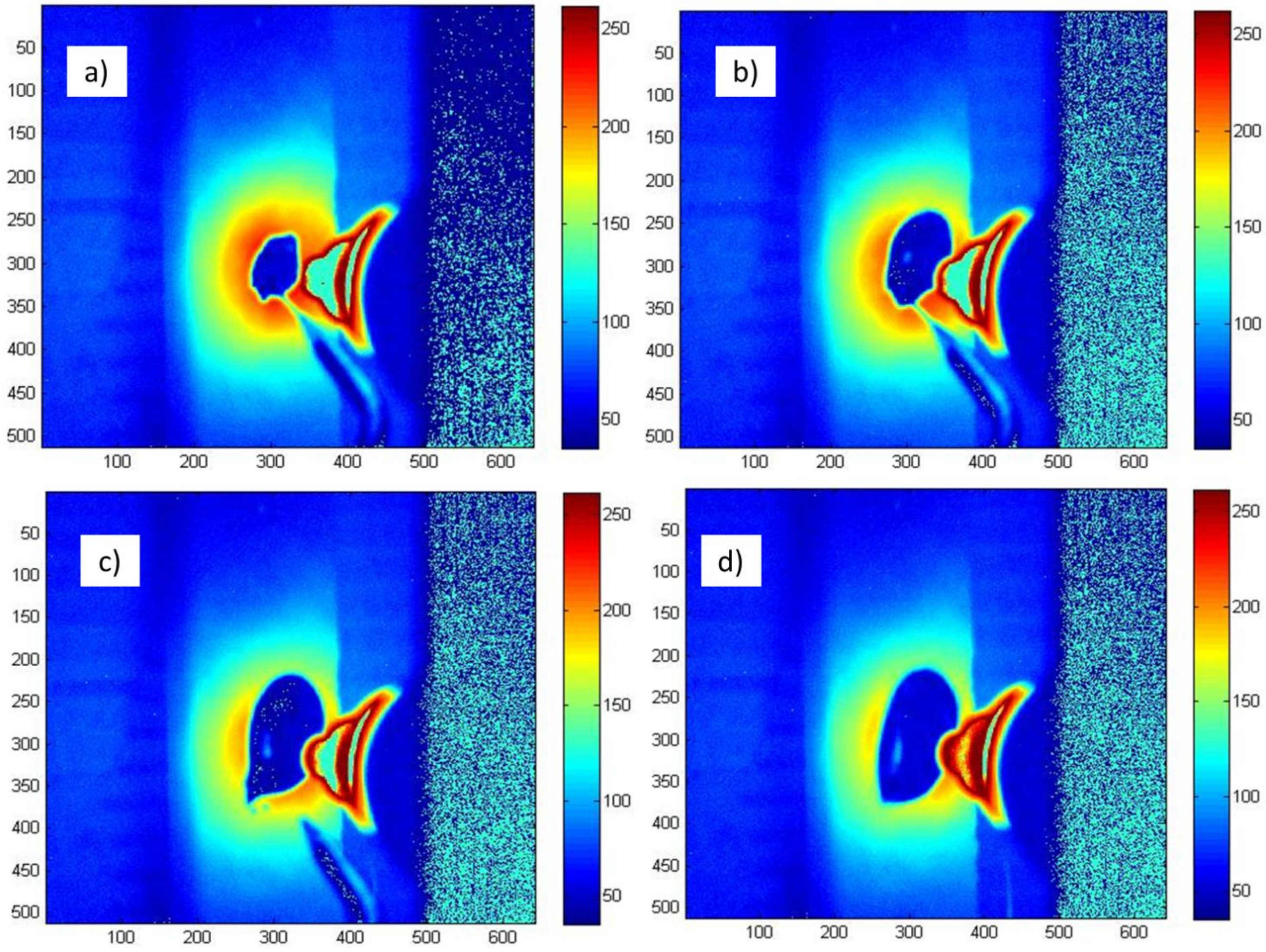

Figure 5.9: Temperature distribution at the beginning of cooling phase:
a) and b): temperature distribution during the water pulverization
c): temperature distribution after 1 sec of cooling
d): temperature distribution after 2 sec of cooling

5.3.1.3 Comparison with numerical modeling

Figure 5.10 shows a comparison between the experimental results with the numerical modeling presented in the 3rd chapter. We observe similar trends during the heating and cooling phases, but with significant gap between the temperature values, which could be related to the lack of quantitative knowledge of the complex environment of the test and the difficulty of well considering the experimental condition in the numerical modeling.

Figure 5.11 shows the variation of the heating and cooling rates deduced from the experimental and numerical results in the non-treated zones. We observe a good agreement concerning the maximum cooling rate: the experimental value is equal to 30 °C/sec, while the numerical one is equal to 23 °C/sec.

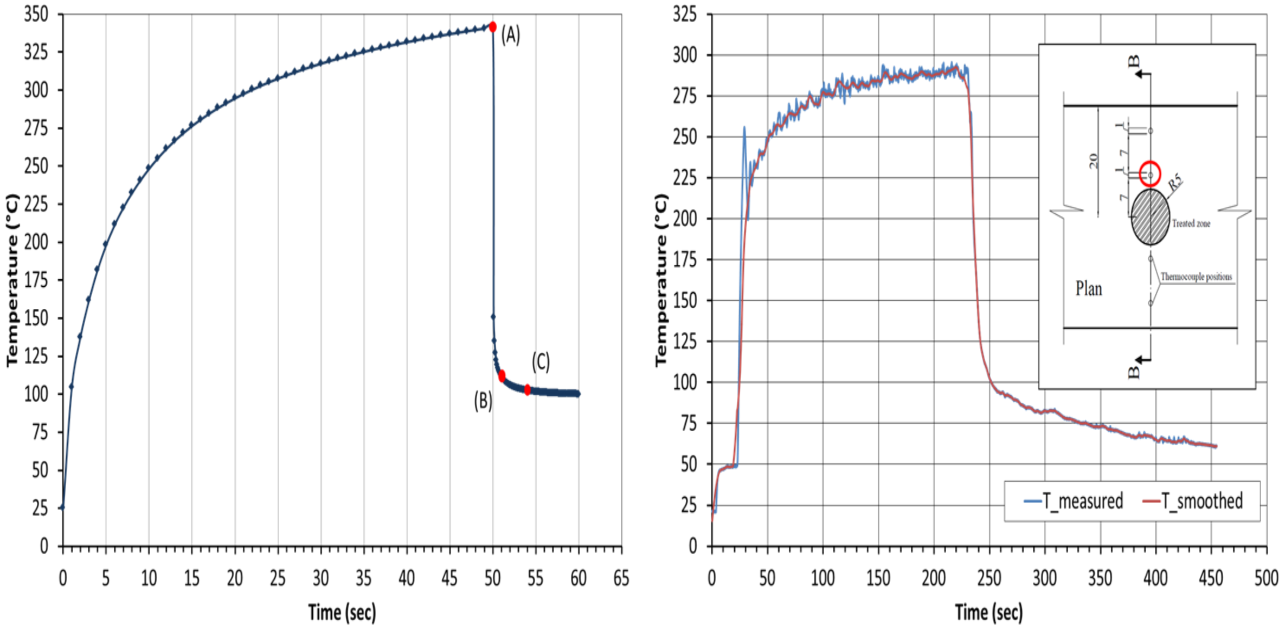

Figure 5.10: Comparison between the numerical and experimental temperature results

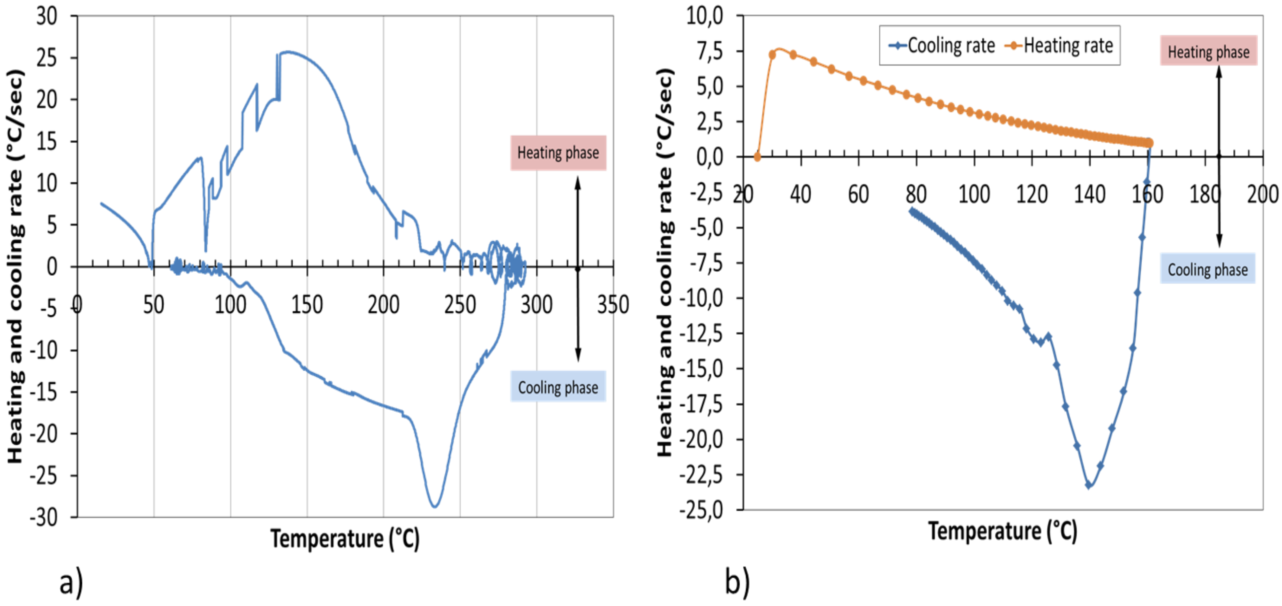

Figure 5.11: a) Experimental heating and cooling rates, b) Numerical heating and cooling rates

Figure 5.12 shows a comparison between the numerical results (for coolant temperature of ~20 °C and ~100 °C) and the experimental ones only during the cooling phase and within the treated zone. Once can see a good agreement between the slopes of the curves. The difference between the measured and the numerical solution in case of fresh water (20 °C) is related to non-consideration of the water amount in the numerical modelling. However, these experimental results confirm exceedingly from thermal point of view the presented numerical results presented in the previous chapters.

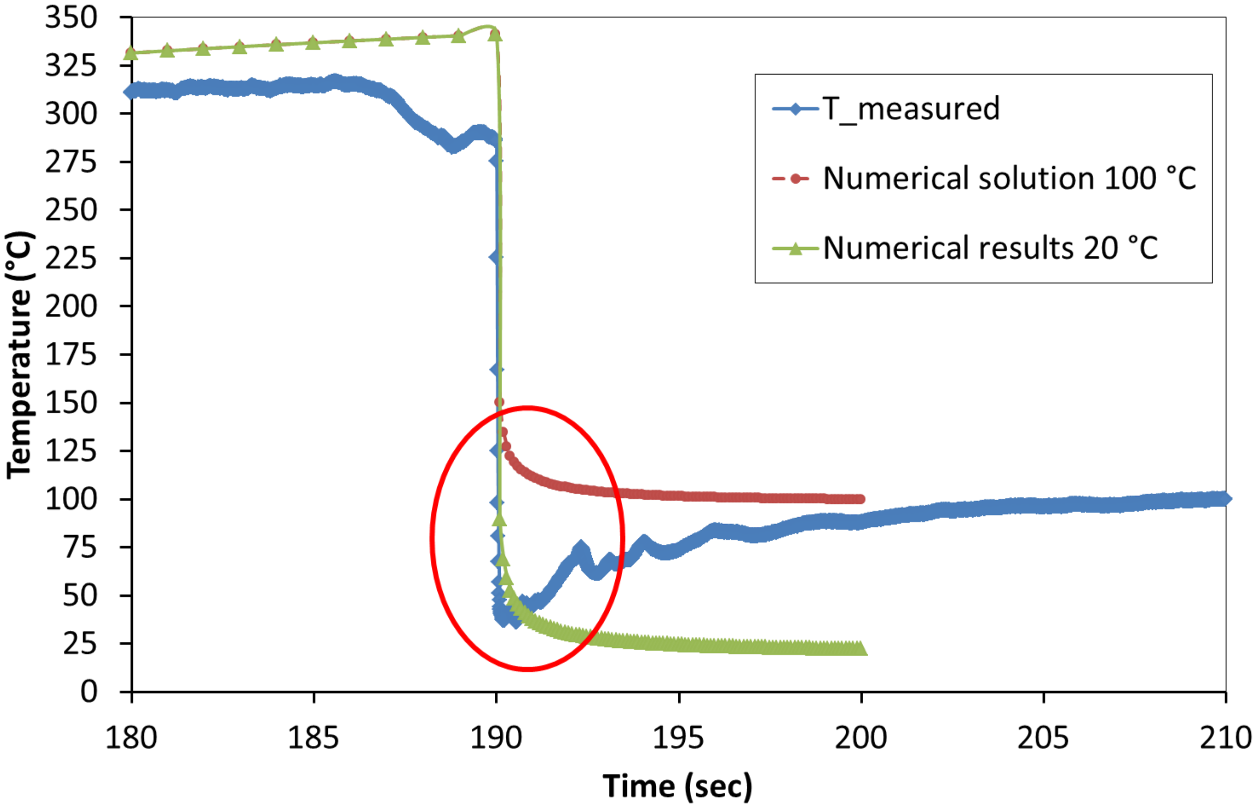

Figure 5.12: Comparison between numerical and experimental results in the cooling phase

The heating and cooling rates deduced from the second test are presented in (Figure 5.13). The high cooling rate happened when the rock surface temperature reached the 200 °C i.e. below the max recorded temperature by 86 °C. This difference between the maximum temperature and the temperature at which the maximum cooling rate occurs is close to that predicted in the numerical model which is about 91 °C.

A fair agreement can be observed between the deduced values of cooling rates from second test (Figure 5.13) and the numerical modelling (Figure 5.14). The difference between them is about 17 %.

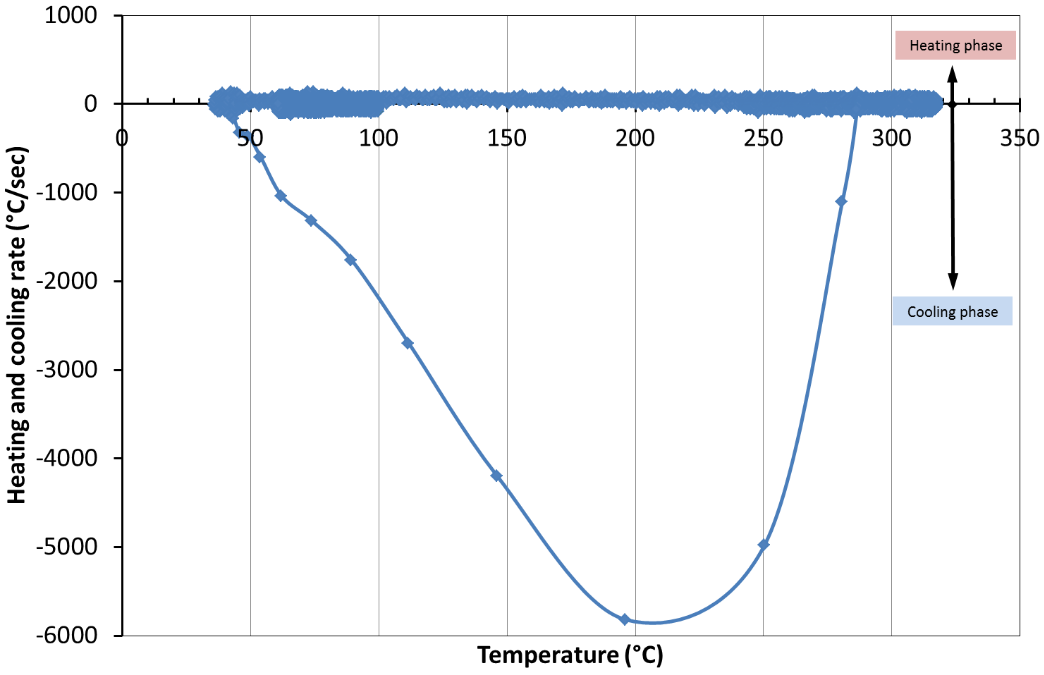

Figure 5.13: Heating and cooling rates during the second test

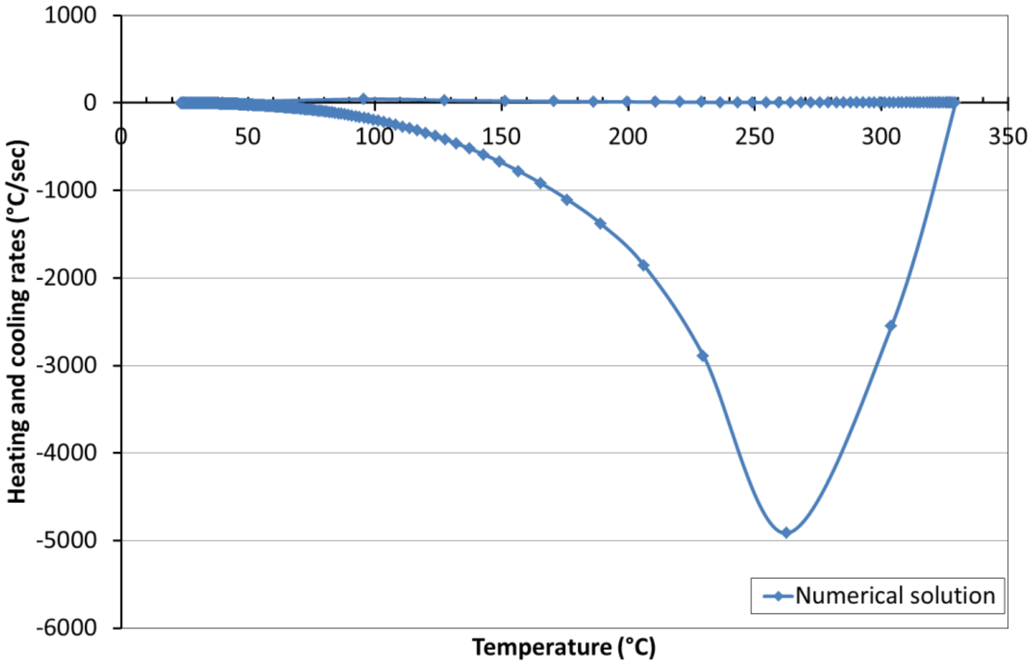

Figure 5.14: Heating and cooling rates within the treated zone

5.3.2 Test with cooling water at 100 °C

The second part of the tests was conducted using cooling water at 100 ° C. Unfortunately, this test was conducted without temperature monitoring. The presentation will focus on naked comparison with tests conducted with cooling water at 20 °C.

When the fresh water (~20 °C) was used, small pool of water was formed over the preheated rock surface. Then, the water temperature increased up to boiling. At this moment, small bubbles (diameter less than 1mm) started to leave the rock surface to join the air vapor. This process occurred during ten seconds. After that, the bubbles decreased gradually, and the water pool stabilized over the rock surface. During the test with hot water (~100 °C), the phase of water heating to the saturation point disappeared completely. Indeed, the hot water boiled at contact with the rock surface. Big bubbles were formed over the rock surface (Figure 5.15). The bubbles had a radius of approximately 1 cm. Few seconds after, the bubbles decreased leading to a stable water pool over the rock surface.

Figure 5.15: Bubbles formation during cooling phase by hot water at (~100 °C)

5.4 Conclusion

This chapter presented an elementary experimental study of the thermal heating/cooling process on granite rock material. Water was used in the cooling phase. The study focused on the temperature evolution during the test and the evolution of the water phase at the surface of the rock sample. The temperature variation was followed using thermocouples and an infrared camera. Difficulties were encounter in the use of the camera, because of the high absorption by water of the infrared radiation. Both qualitative and quantitative results were obtained with tests conducted using cooling water at 20° C, while only qualitative results were obtained with the test conducted with cooling water at 100° C.

During the heating phase, tests showed a rapid increase in the temperature (up to 250 °C), followed by a slow increase up to the maximum temperature (around 290 °C). During the cooling phase and concerning the first test, we observe first a rapid temperature decrease (about 100 °C), followed by a slow decrease down to 60 °C. Whilst in the second test, the temperature dropped instantaneously after the coolant pouring from 286 °C to 35 °C. The test conducted using cooling water at 100 °C, showed that the disappearance of the water heating to the saturation point, because, the water boiled at the contact of the rock surface.

The experimental results of the test conducted using cooling water at 20 °C was compared to the numerical modeling conducted in the 3rd chapter. Experimental trends were well reproduced. However, an important gap between the numerical and experimental results was observed during the cooling phase. This gap could be attributed to the lack of a good quantitative knowledge of the experimental condition and the complexity of the phenomena under consideration.

CONCLUSION

This thesis included the development and analysis of a thermal process for the rock material fracture. The process consists in locally heating the rock material surface using microwaves radiation followed by cooling this surface by water. During the heating phase, the treated zone is subjected to compressive stresses, which could lead to crack initiation in the rock material. During the cooling phase, the rock material is subjected to shrinkage, which could lead to extensile stresses and rock fracture by extension. This process was analyzed by means of both coupled numerical modelling and laboratory experiments.

The numerical model takes into consideration the coupled physical phenomena, in particular the microwaves-rock coupling (heating phase), the coolant-rock interaction (cooling phase) and the thermo-mechanical coupling in the rock material.

Numerical simulations were conducted using the software Comsol Multiphysics. Parametric analysis showed that the efficiency of the thermal treatment depends on the following parameters: the density of the irradiation energy, the period of the heating phase, the heat exchange coefficient, and the temperature of the coolant.

The increase in the irradiation density leads to an increase in the maximum temperature and in the penetration depth. The increase of the heating period from 25 sec to 300 sec leads to an increase in the penetration depth from 0.2 mm to 1.35 mm. The increase of the heat exchange coefficient leads to an increase in both the tensile stresses and penetration depth. The temperature of the coolant affects also the magnitude of the tensile stresses as well as the penetration depth. The decrease of this temperature from 100° C to 20° C leads to an increase of about 400% in the penetration depth.

The efficiency of the cyclic heating/cooling process was analyzed using a continuum damage constitutive model. The consideration of the rock damage in the analysis of the heating/cooling process leaded to an increase of about 20% in the penetration depth. The consideration of the rock damage leaded to 50% energy saving in the 2^{nd} cycle. The rate of penetration in the granitic rock was estimated to 0.02 mm/s.

The experimental work confirmed the viability of the heating/cooling process from the thermal point of view. The experimental cooling curve agreed with the numerical modelling. The experimentally recorded cooling rate was also close to that predicted in the numerical modeling. However, this study should be pursued using adequate experimental equipment to improve our knowledge of the physical complex phenomena involved in the heating/cooling process.

The numerical modeling was conducted on homogeneous rock material. However, the rock material is a multiphasic porous material, which has generally high heterogeneity. The latter is generally favorable for the creation of heterogeneous stress distribution, which could improve the efficiency of the proposed method; this issue constitutes a good axe for future researches.

The proposed method presents high advantages, its use in engineering is promising, but yet requires technological development for its adaption to field working condition.

REFERENCES

Ahmadi, M., Erfan, M.R., Torkamany, M.J., Sabbaghzadeh, J., 2012. The effect of confining pressure on specific energy in Nd:YAG laser perforating of rock. Optics & Laser Technology 44, 57-62.

Ahmadi, M., Erfan, M.R., Torkamany, M.J., Safian, G.A., 2011. The effect of interaction time and saturation of rock on specific energy in ND:YAG laser perforating. Optics & Laser Technology 43, 226-231.

Chaboche, J.L., 1988. Continuum Damage Mechanics, Part I & II. J. Appl. Mech. 55, 59-72.

Chaki, S., Takarli, M., Agbodjan, W.P., 2008. Influence of thermal damage on physical properties of a granite rock: Porosity, permeability and ultrasonic wave evolutions. Construction and Building Materials 22, 1456-1461.

Cherepanov, G.P., 1966. High Temperature Drilling. Journal of Applied Mechanics and Technical Physics 7, 114-118.

Comsol, 2011. COMSOL Multiphysics User’s Guide version 4.2a.

Damhof, F., Brekelmans, W.A.M., Geers, M.G.D., 2008. Non-local modeling of thermal shock damage in refractory materials. Engineering Fracture Mechanics 75, 4706-4720.

Deeny, S., Stratford, T., Dhakal, R., Moss, P., Buchanan, A., 2008. Spalling of Concrete: Implications for Structural Performance in Fire, 20th Australasian Conference on the Mechanics of Structures and Materials (ACMSM20), Australia.

Eberhardt, E., 1998. Brittle Rock Fracture and Progressive Damage in Uniaxial Compression, Geological Sciences. University of Saskatchewan, Canada.

Faghri, A., Zhang, Y., 2006. Transport Phenomena in Multiphase Systems. Elsevier.

Farra, G., 1968. Experimental Observation of Rock Failure Due to Laser Radiation, Departement of Civil Engineering. Massachusetts Institute of Technology, p. 128.

Finnie, I., Cooper, G.A., Berlie, J., 1979. Fracture Propagation in Rock by Transient Cooling. International Journal of Rock Mechanics and Mining Sciences 16, 11-21.

Germanovich, L.N., 1997. Thermal Spalling of Rocks, 9th International Conference on Fracture, Sydney, Australia, pp. 2771-2782.

Gong, Q.M., Zhao, J., 2007. Influence of rock brittleness on TBM penetration rate in Singapore granite. Tunnelling and Underground Space Technology 22, 317-324.

Gong, Q.M., Zhao, J., 2008. Development of a rock mass characteristics model for TBM penetration rateprediction. international Journal of Rock Mechanics and Mining Sciences 46, 8-18.

Heiniö, M., 1999. ROCK EXCAVATION HANDBOOK. Sandvik Tamrock Corp.

Heuze, F.E., 1983. High-temperature mechanical physical and thermal properties of granitic rocks, A review. Int.J. Rock Mechanics. Min. Sci. And Geomech 20, 3–10.

Hewson, A.C., 1970. An introduction to the theory of electromagnetic waves. Harlow Longman.

Hommand-Etienne, F., Hourpert, R., 1989. Thermally Induced Microcracking in Granite: Characterization and Analysis. International Journal of Rock Mechanics and Mining Sciences 26, 125-134.

Huotari, T., Kukkonen, l., 2004. Thermal Expansion Properties of Rocks: literature Survey and Estimation of Thermal Expansion Coefficient for Olkiluoto Mica Gneiss. Geological Survey of Finland, Finland, p. 68.

Jerby, E., Dikhtyar, V., 2001. Drilling into Hard Non-Conductive Materials by Localized Microwave Radiation, Ampere Conference. Trends in Microwave and HF Heating, Springer Verlag, 2002, Bayreuth, Germany.

Kachanov, L.M., 1958. Rupture Time Under Creep Conditions. Iv.Acad. Nuauk USSR, OTN 8, 26-31.

Kachanov, L.M., 1986. Introduction to Continuum Damage Mechanics, Martinus Nijhoff Publishers, Dordrecht, Netherlands.

Karwa, N., 2012. Experimental Study of Water Jet Impingement Cooling of Hot Steel Plates.

Karwa, N., Gambaryan-Roisman, T., Stephan, P., Tropea, C., 2011. A hydrodynamic model for subcooled liquid jet impingement at the Leidenfrost condition. International Journal of Thermal Sciences 50, 993-1000.

Kill, I.D., 1967. study of rock fracturing under high temperature gas jet impact with application to drilling in open mines, Moscow Mining Institute.

Lan, H., Martin, C.D., Hu, B., 2010. Effect of heterogeneity of brittle rock on micromechanical extensile behavior during compression loading. Journal of Geophysical Research 115.

Lemaitre, J., 1985. A Continuum Damage Mechanics Model for Ductile Fracture. J. Engrg. Mat. and Technol. 107, 83-89.

Liang, X., Headrick, W.L., Darani, L.R., 2006. Continuum Damage Mechanics Modelling of The Failure of the Refractory Cup Under Thermal Loading And Chemical Shrinking. Refractories Application and News 11, 17-23.

Lmdroth, D.P., Morrell, R.J., Blair, J.R., 1991. Microwave Assisted Hrd Rock Cutting. The United States of America as represented by the Secretary of the Interior, Washington, D.C.

Lockner, D.A., 1998. A generalized law for brittle deformation of Westerly granite. Journal of Geophysical Research 103, 5107-5123.

Norton, F.H., 1925. A general theory of spalling. Journal of the American Ceramic Society 8, 29-39.

Olaleye B, M., 2010. A review of light amplification by stimulated emission of radiation in oil and gas well drilling. Mining Science and Technology (China) 20, 752-757.

Ozbolt, J., Ananiev, S., 2007. Scalar Damage Model for Concrete Without Explicit Evolution Law. Institute of Construction Materials, University of Stuttgart. Pfaffenwaldring 4, Pfaffenwaldring, Germany.

Palmström, A., 1996. Engineering geology and rock engineering applied in the design of Norwegian tunnels, Tunnels for the third Millennium, Slovakia.

Potter, R.M., Potter, J.M., Wideman, T., 2010. Laboratory Study and Field Demonstration of Hydrothermal Spallation Drilling. GRC Transactions 34.

Preston, F.W., White, H.E., 1934. Observation on Spalling. Journal of the American Ceramic Society 17, 137-144.

Rauenzahn, R.M., 1986. Analysis of rock mechanics and gas dynamics of flame-jet thermal spallation drilling, Departement of Chemical Engineering Massachusetts Institute Of Technology.

Rauenzahn, R.M., Tester, J.W., 1989. Rock Failure Mechanisms of Flame-Jet Thermal Spallation Drilling - Theory and Experimental Testing. International Journal of Rock Mechanics and Mining Sciences 26, 381-399.

Ross, S.L., 1964. Excavating Apparatus and Method, in: Office, U.S.P. (Ed.), United States of America.

Seipold, U., Huenges, E., 1998. Thermal Properties of gneisses and amphibolites-high pressure and high temperature investigations of KTB-rock samples. Tectonophysics 291, 173-178.

Singha, T.N., Sinha, S., Singh, V.K., 2007. Prediction of thermal conductivity of rock through physico-mechanical properties. Building and Environment 42, 146-155.

Sun, X., Khaleel, M.A., 2004. Modeling of Glass Fracture Damage Using Continuum Damage Mechanics – Static Spherical Indentation. International Journal of Damage Mechanics 13, 263-285.

Takarli, M., Agbodjan, W.P., 2006. Etude expérimentale de l'endommagement thermique du granite, Laboratoire de Génie Civil et Génie Mécanique, INSA de Rennes.

Tarasovs, S., Chassemi, A., 2012. On The Role of Thermal Stress In Reservoir Stimulation, in: University, S. (Ed.), Thirty-seventh Workshop on Goethermal Reservoir Engineering, Stanford, California, USA.

Tavman, I.H., 1996. Effective Thermal Conductivity of Granular Porous Materials. International Journal of Heat and Mass Transfer 23, 169-176.

Ulaby, F.T., Bengal, T.H., Dobson, M.C., East, J.R., Garvin, J.B., Evans, D.L., 1990. Microwave Dielectric Properties of Dry Rocks. IEEE Transaction on Microwave Theory and Techniques 28, 325-337.

Van de Steen, B., Vervoort, A., Napier, J.A.L., Durrheim, R.J., 2003. Implementation of a Flaw Model to the Fracturing Around a Vertical Shaft. Rock Mechanics and Rock Engineering 36, 143-161.

Vasconcelos, G., Lourenço, P.B., 2008. Experimental Characterization of The Compressive Behavior of Granites. Mecânica Experimental 16, 61-71.

Vlachopoulos, J., Strutt, D., 2002. Basic Heat Transfer And Some Application in Polymer Processing, Plastics Technician's Toolbox, pp. 21-33.

Vosteen, H.-D., Schellschmidt, R., 2003. Influence of temperature on thermal conductivity, thermal capacity and thermal diffusivity for different types of rock. Physics and Chemistry of the Earth 28, 499-509.

Walsh, S.D.C., Lomov, I., 2013. Micromechanical Modeling of Thermal Spallation in Granitic Rock. International Journal of Heat and Mass Transfer 65, 366-373.

Walsh, S.D.C., Lomov, I., Roberts, J.J., 2011. Geomechanical Modeling for Thermal Spallation Drilling. GRC Transactions 35, 277-282.

Walsh, S.D.C., Lomov, I., Roberts, J.J., 2012. Grain-Scale Failure in Thermal Spallation Drilling, Thirty-Seventh Workshop On Geothermal Reservoir Engineering, Stanford University, Stanford, California, USA.

Wu, X., 2002. Experimental and Theoretical Study of Microwave Heating of Thermal Runaway Materials, Mechanical engineering. Virginia Polytechnic Institute and State University.

Xu, Z., Reed, C.B., Graves, R., Parker, R., 2004. Rock Perforation by Pulsed ND:YAG Laser, International Congress on Applications of Lasers and Electro-Optics.

Xu, Z., Reed, C.B., Konercki, G., Parker, R.A., Gahan, B.C., Batarseh, S., Figuerao, H., Skinner, N., 2003. Specific energy for pulsed laser rock drilling. Journal of Laser Application 15, 25-30.

Xu, Z., Yamashita, Y., Reed, C.B., 2005. Two Dimensional Modelling of Laser Spallation Drilling of Rock, International Congress on Applications of Lasers and Electro-Optics, ICALEO, Laser Institute of America

Zhao, S., Dharani, L.R., Chai, L., Barbat, S.D., 2005. Analysis of damage in laminated automotive glazing subjected to simulated head impact. Engineering Failure Analysis 13, 582-597.

Zhou, L., Puri, V.M., Anantheswaranb, R.C., Yeh, G., 1995. Finite Element Modeling of Heat and Mass Transfer in Food Materials During Microwave Heating - Model Development and Validation. Journal of Food Engineering 25, 509-529.